A STUDY OF THE
EFFECT OF DISORDER AND
CONFINEMENT ON BINARY SYSTEMS

THESIS SUBMITTED FOR THE DEGREE OF

DOCTOR OF PHILOSOPHY (SCIENCE)

OF THE

WEST BENGAL UNIVERSITY OF TECHNOLOGY

SHREEMOYEE GANGULY

SATYENDRANATH BOSE NATIONAL CENTRE
FOR BASIC SCIENCES
JD BLOCK, SECTOR 3, SALT LAKE CITY
KOLKATA 700 098, INDIA

JULY, 2011

Thesis Certificate

This is to certify that the thesis entitled **"A Study of the Effect of Disorder and Confinement on Binary Systems"** submitted by Shreemoyee Ganguly to the West Bengal University of Technology for the award of the degree of Philosophy, is a bona fide record of the research work done by her under my supervision in the duration of five years from August 2006 to July 2011. She has completed the work truthfully and successfully to the best of my knowledge. The contents of this thesis, in full or in part, have not been submitted to any other Institute or University for the award of any degree or diploma.

Abhijit Mookerjee
(Supervisor)
Emeritus Professor, Materials Science Depatment,
Satyendranath Bose National Centre For Basic Sciences,
JD Block, Sector III, Salt Lake City, Kolkata 700 098
India

To my grandmother who is no more ......

ACKNOWLEDGMENTS

"Nature is made in such a way as to be able to be understood. Or perhaps I should put it more correctly the other way around, and say that we are made in such a way as to be able to understand Nature." - Werner Heisenberg

I would like to take this opportunity to express my heart-felt gratitude to those people who have guided me, motivated me and been with me all through these five years of academic journey that has culminated into this thesis work.

The first person I would like to express my gratitude to is my supervisor Prof. Abhijit Mookerjee. I first came across him during my M.Sc. days as my Quantum Mechanics instructor. From those early days I have found him to be a great source of scientific inspiration. During my thesis work his vastness of scientific knowledge and insight into various problems has impressed me time and again. Working with him I have realized that :

Difficulties are opportunities to better things; they are stepping stones to greater experience. Perhaps someday we will be thankful for some temporary failure in a particular direction. When one door closes, another always opens.

He has helped me to mature not only scientifically but also as an independent human being. He has given me the opportunity to work at premier institutions like Indian Institute of Technology, Kanpur and Uppsala University, Uppsala. My stay at these institutes has not only led to progress in my scientific projects but has also taught me to interact with the scientific community at large. In this respect I would also like to thank his wife, Mrs. Mookerjee, whom we fondly call "Madam", for being so affectionate and creating a home away from home during my stay in Kanpur.

Next, I would like to deeply acknowledge Prof. Indra Dasgupta, Indian Asscociation for the Cultivation of Science, Kolkata for not only introducing me to the field of superconductivity but also being a constant source of scientific inspiration and guiding me in all my decisions regarding my academic career. He has truly been one of my scientific mentors.

I would also like to thank Dr. Mukul Kabir, Massachusetts Institute of Technology, Cambridge, Massachusetts who has introduced me to the field of cluster physics. His extreme enthusiasm in this field has been contagious. I also consider him to be one of my scientific mentors.

During my stay in Uppsala University, Sweden I have not only profited from my scientific discussions with Dr. Biplab Sanyal but he has also very kindly given me the

Shreemoyee Ganguly
S.N.Bose National Centre for Basic Sciences,
Kolkata, India.

Publications

1. **A study of superconductivity in multi-band disordered systems : A vector recursion approach.**
   Shreemoyee Ganguly, Indra Dasgupta and Abhijit Mookerjee
   Submitted to Phys. Rev. B - *Manuscript under review.*

2. **Augmented space recursion formulation of the study of disordered alloys with noncollinear magnetism and spin-orbit coupling: Application to MnPt and Mn3Rh.**
   Shreemoyee Ganguly, Marcio Costa, Angela B. Klautau, Anders Bergman, Biplab Sanyal, Abhijit Mookerjee, and Olle Eriksson
   Phys. Rev. B **83**, 094407 (2011)

3. **Unusual structure and magnetism in manganese oxide nanoclusters.**
   Shreemoyee Ganguly, Mukul Kabir, Biplab Sanyal and Abhijit Mookerjee
   Phys. Rev. B **83**, 020411(R) (2011).
   This paper was featured in Virtual Journal of Nanoscale Science and Technology, Vol-23, Issue-6 (2011).

4. **A real space approach to study the effect of off-diagonal disorder on superconductivity.**
   Shreemoyee Ganguly, Indra Dasgupta, and Abhijit Mookerjee
   Physica C **470**, Issues 15-16, 640 (2010).

5. **Augmented space recursion study of the effect of disorder on superconductivity.**
   Shreemoyee Ganguly, A.Venkatasubramanian, Kartick Tarafder, Indra Dasgupta, and Abhijit Mookerjee
   Phys. Rev. B **79**, 224204 (2009).

6. **A local-density approximation for the exchange energy functional for excited states: The band-gap problem.**
   Moshiour Rahaman, Shreemoyee Ganguly, Prasanjit Samal, Manoj Kumar Harbola, Tanusri Saha-Dasgupta and Abhijit Mookerjee
   Physica B: **404**, Issues 8-11, 1137 (2009).

---

[0]The contents of the paper with serial number (6), (8) and (9) are not included in this thesis.

7. **Magnetism in small bi-metallic Mn-Co clusters**
   <u>Shreemoyee Ganguly</u>, Mukul Kabir, Soumendu Datta, Biplab Sanyal and Abhijit Mookerjee
   Phys. Rev. B **78**, 014402(2008).
   This paper was featured in the Virtual Journal of Nanoscale Science and Technology,Vol-18, Issue-2 (2008).

8. **A Cartoon in One Dimension of the Hydrogen Molecular Ion**
   Sourav Datta, <u>Shreemoyee Ganguly</u> and Binayak Dutta-Roy
   Eur.J.Phys **29**,235 (2008).

9. **Structure, bonding and magnetism of cobalt clusters from first-principles calculations**
   Soumendu Datta, Mukul Kabir, <u>Shreemoyee Ganguly</u>, Biplab Sanyal, Tanusri Saha-Dasgupta and Abhijit Mookerjee
   Phys. Rev. B **76**,014429 (2007).

Contents

List of Figures

List of Tables

Chapter 1

Introduction

A study of binary systems in cluster form (confined systems) as well as in the bulk is of great technological relevance and is also physically intuitive. The basic types of structures that can be formed for mono-atomic clusters are now well-established. For example Lennard-Jones clusters [Wales and Doye 1997] provide a well-characterized archetypal model for systems with isotropic interactions. However, the situation for *binary clusters* is potentially more challenging, and the new types of structures that can be stabilized by the presence of two different atom types are only beginning to be mapped out.

Considering the scenario in the bulk, the discovery of binary alloys like brass (formed by alloying copper and zinc), bronze (formed by combining copper with a small proportion of tin) and steel (formed by alloying iron with a small amount of carbon) has remarkably improved the quality of human life. Alloying two or more constituents is one of the most successful processes in the search for new materials. Therefore, the study of the electronic structure of alloys is an important area of research in materials physics. Alloys of our interest are multi-component systems which primarily exhibit metallic bonding and may contain one or more phases. In the present study we will be studying the effect of randomness in *binary alloys*.

1.1 Transition Metal Nanoalloy clusters

The primary interest in transition metal clusters arises from a desire to seek a solution to the technologically important question : how magnetic properties change in reduced dimensions? The magnetism of bulk-transition metals is known to be due to itinerant d

electrons in contrast to the magnetism of atoms and insulators which is due to electrons localized in atomic-like orbitals. Thus, the study of transition metal clusters will also help to answer the fundamental question of electron delocalization as a function of cluster size. Furthermore, interesting structural dependence of the magnetic properties of transition metals has been observed, which reflects the sensitivity of these to the details in the electronic structure. The magnetization is also very sensitive to changes in the local environment that occur at surfaces or alloys. Since in a small cluster the local environment (e.g., coordination number) and structure vary sensitively with cluster size n, the transition metal clusters are expected to show a wide variety of magnetic properties as a function of n.

All our cluster calculations are done using *ab-initio* or first-principles techniques, whereby the properties of materials are predicted starting from the principles of quantum mechanics. With the development of modern computation, with a reasonable amount of resources, high throughput first principles studies can be performed and there are indications that these calculations have considerable predictive power. Though standard quantum-chemistry methods are adequate for describing electronic structure of transition metal clusters, owing to their enormous computational load, their applicability is often limited to small clusters consisting of simple metals, in which treatment of d-electrons is not essential. To avoid such restrictions, for $3d$ transition metal clusters one generally uses pseudo-potentials and density functional theory (both of which are discussed in detail in the next chapter of this thesis). Pseudo-potential theory allows one to focus on the chemically active valence electrons by replacing the strong all-electron atomic potential with a weak pseudo-potential, which effectively reproduces the effects of the core electrons on the valence states. Density functional theory replaces the many-electron wave function representation of the system, which is present in standard quantum chemistry approaches, by a set of non-interacting one-electron wave functions with the same charge density as the original system. The basis sets that are used for expanding the one-electron wave functions are plane waves. Basis sets like Gaussians or atomic-like functions require an extensive testing. This entails an optimization of a multiple parameter space. Consequently, the results obtained from these approaches can be sensitive to the basis choice. Plane-wave methods have the advantage that only one parameter (the wavelength of the

highest Fourier component used in the expansion) need to be refined to control conver-
gence. However in a plane-wave representation, periodic boundary conditions are typically
involved. Thus in order to study a non-periodic system such as a cluster using it, care
must be taken to reproduce the vacuum accurately, since spurious interactions between
replicated images of the system must be avoided.

In recent times nanoalloy clusters have received considerable attention for their pe-
culiar catalytic, optical, magnetic, electronic, and geometric properties [Jellinek and
Krissinel 1999, Kondow, 2003, Klabunde 1994, Andrews *et.al.* 1992, Jellinek 2008].
For such clusters, chemical and physical properties can be tailored by varying not only
the size but also the composition for a specific purpose. This opens the way to a large
variety of potential applications in areas such as high-density recording [Sun *et.al.* 2000],
catalysis [Sinfelt 1983, Molenbroek *et.al.* 2001, Hansen *et.al.* 1997], optics [Shibata *et.al.*
2002, Darby *et.al.* 2002, Ruban *et.al.* 1999] and biomedical studies [Loo *et.al.* 2005]. So
the first study that we made (Chapter 3 of the thesis) is on a transition metal nanoalloy
cluster system.

The candidates chosen for this study, Mn and Co have very interesting properties in
low dimensions. Manganese, though anti-ferromagnetic as bulk, shows finite magnetic
moment in reduced dimension [Knickelbein 2001, Knickelbein 2004, Kabir *et.al.* 2006,
Kabir *et.al.* 2007] whereas, Cobalt shows enhanced magnetic moment compared to the
bulk [Xu *et.al.* 2005, Knickelbein 2006, Datta *et.al.* 2007]. Therefore, it will be interesting
to see how the properties of the bimetallic cluster formed out of these two elements change
with composition, atomic ordering, and size.

The first step in the study of cluster properties is the determination of the ground
state structures and the complexity of locating these increases with the cluster size, as
the number of local minima in the potential energy surface increases. This leaves a number
of possible geometric and/or magnetic isomers in pure clusters for each size. Compared to
the pure clusters, in alloy clusters "homotops" [Jellinek and Krissinel 1999] are possible
in addition to such usual isomers. Jellinek introduced the term "homotop" to describe
A_xB_y alloy cluster isomers, with a fixed size ($x + y$=n) and composition (x/y ratio),
which have the same geometrical arrangement of atoms, but differ in the way A- and
B-type atoms are arranged. Due to the presence of these homotops, there arises a large

number of combinatorial possibilities which makes the finding of lowest energy structures for alloy clusters an even more computationally expensive task compared to pure clusters. Thus most of the theoretical studies done on bimetallic alloy clusters take resort to some empirical many-body potential to reduce computational expense [Jellinek and Krissinel 1999, Christensen *et.al.* 1995, Lopez *et.al.* 1996, Jellinek *et.al.* 1996, Krissinel and Jellinek 1997, Krissinel and Jellinek 1997, Jellinek *et.al.* 1999]. Our study is one of the very few which uses an *ab-initio* methodology for transition metal nanoalloy clusters.

1.2   Transition Metal Nano-oxide clusters

Extensive studies have been performed to characterize transition metal clusters and recently interest has expanded to transition metal oxides due to their applications as model systems in heterogeneous catalysis and materials science on a microscopic level [Schröder and Schwarz 1973, Keesee *et.al.* 1993]. By some estimates 90% of all commercially produced chemical products involves catalysts at some stage in the process of their manufacture. Catalysis is the acceleration of a chemical reaction by means of a substance, called a catalyst, which is itself not consumed by the overall reaction.

Group V transition metal (V, La, Nb) oxide clusters have proved to be catalytically active for oxidation reactions [Zhao *et.al.* 2011]. Chromium (Group VI transition metal) oxides besides being catalysts for many industrial processes, are widely used in magnetic recording tapes and other magnetic media [Schwarz 1986, Kamper *et.al.* 1987, Korotin *et.al.* 1998]. Very few experimental studies on group VII transition metal (Re, Mn) oxide clusters exist in literature. Manganese Oxide clusters are extremely important not only as catalysts and in the magnetic media but also in Mn-based single molecular magnets. They also take essential part in a variety of biological processes from photosynthesis to bacterially mediated organic matter decomposition. Thus it becomes necessary to characterize MnO clusters thoroughly and systematically. This we attempt to do in the fourth chapter of the thesis.

1.3   Disordered Alloys

The most common disordered alloys are substitutionally disordered alloys. These alloys have underlying lattice structure but each lattice point is occupied randomly by the constituent atoms. Thus the system lacks lattice translational symmetry. The difficulty arising due to this loss of periodicity is overcome by introducing mean-field theories [Ehrenreich and Schwartz 1976, Faulkner 1980, Bansil 1987, Prasad 1995]. In these approaches, the disordered system is replaced by a lattice periodic effective medium, with effective atoms occupying lattice sites. One of the most successful mean-field approximations is the coherent potential approximation (CPA) [Soven 1970]. However, whenever local environmental effects become important: like short-ranged ordering, chemical affinity driven local clustering, or if we are dealing with rough surfaces and interfaces, the augmented space recursion (it is discussed in detail in Chapter 5 of the thesis) is one of the more powerful techniques available. It goes beyond standard mean-field approximations to consider randomness not only at a site but also in its near neighbourhood. We use this augmented space recursion technique to study the effect of substitutional disorder on single-band and multi-band superconductivity in model binary alloy systems in Chapter 6 and Chapter 7 of the thesis respectively.

It has been customary to use semi-empirical tight-binding Hamiltonians to describe electronic properties. In spite of encouraging successes, electronic structure calculations based on semi-empirical tight-binding Hamiltonians have unjustified underlying assumptions of transferability of the Hamiltonian parameters [Pettifor 1992]. The major step towards constructing first principles tight-binding Hamiltonians began with the tight-binding, linearized muffin-tin-orbitals method (TB-LMTO) proposed by Anderson and Jepson 1984. In TB-LMTO, the Hamiltonian is characterized by a set of potential parameters which are derived self-consistently from a first-principles theory and are not empirical. Kudronovský and Drchal 1990 have demonstrated that the CPA based on the TB-LMTO accurately describes the electronic structure of random alloys with metallic and semi-conducting components in a large class of alloy systems. Within the TB-LMTO method, charge self-consistency can be achieved and extensive calculations have been carried out for elements, compounds and alloys. The TB-LMTO is usually implemented

within the atomic sphere approximation. The complicated shapes of the Wigner-Seitz cells are replaced by atomic spheres of the same volume. These spheres may overlap up to a maximum of about 15% of the sphere volumes and the contribution from the remaining interstitial space is either neglected or filled up as far as possible with empty spheres carrying charge but no ion cores.

However, there are many situations where single-site approximations (like CPA) begin to fail: for example, when clustering effects become important [Kumar *et.al.* 1982] in the impurity bands of split band alloys or when short-ranged order dominates, leading to ordering or segregation [Gonis *et.al.* 1987]. As mentioned before the augmented space recursion (ASR) effectively deals with such situations where one needs to go beyond single-site approximations. Thus for such situations we need to use TB-LMTO-ASR [Chakrabarti and Mookerjee 2005] instead of TB-LMTO-CPA. In Chapter 8 we have extended the TB-LMTO-ASR to deal with non-collinear magnetism to study the effect of disorder on non-collinear magnetism in binary alloys. We have applied our methodology to MnPt alloy system.

Single-site approximations also fail in alloys whose constituents have large differences in atomic radii leading to local lattice distortion effects whenever unlike-atoms surround one another. This results in off-diagonal disorder in the structure matrix [Bose *et.al.* 1992]. This happens usually when alloys are formed out of atoms coming from different rows of the periodic table and are called non-isochoric [Kudronovský and Maśek 1985]. Usual treatments of alloys with substitutional disorder place all atoms on a regular lattice whose lattice spacing is obtained either by assuming Vegard's law or by energy minimization with respect to the lattice constant. Though such an approach gives reasonable results for those alloys made out of components with nearly equal atomic radii, it overlooks the differential expansion (contraction) around larger (smaller) atom for non-isochoric alloys. The local lattice distortion of the ideal lattice has been verified by extended X-ray absorption fine structure experiments [Weightman *et.al.* 1987]. ASR provides a formally exact way of dealing with off-diagonal disorder. In Chapter 6 we have also studied the effect of such off-diagonal disorder on superconductivity in model binary alloy.

Chapter 2

A brief review of density functional theory

In this chapter, we shall present an overview of the density functional theory which describes the ground state properties of a many electron system in terms of the density of the system. This theory forms the backbone of our study of the electronic structure of the MnCo and MnO clusters and MnPt alloy in our subsequent chapters.

2.1 The many-body Schrödinger equation

The Schrödinger equation is the conventional point to begin description of many-electron systems. For stationary state problems :

$$\hat{H}\psi = i\bar{h}\frac{\partial \psi}{\partial t} = E\psi \tag{2.1}$$

where $\hat{H}$ represents the Hamiltonian of an N-electron system and can be written as (atomic units are used throughout)

$$H = \sum_{I=1}^{N_c} \frac{-\nabla_I^2}{2M_I} + \sum_{i=1}^{N} \frac{-\nabla_i^2}{2m} + \frac{1}{2}\sum_{i,j}\frac{1}{r_{ij}} + v_{eI}(\{\mathbf{r}_i\}, \{\mathbf{R}_I\}) + V_{II}(\{\mathbf{R}_I\}) \tag{2.2}$$

where we have considered a system consisting of N_c ion-cores (the Ith ion core having a mass M_I) bonded in a solid by N valence electrons (the ith valence electron having a mass m). V_{II} and v_{eI} are the Coulomb interactions between the ions themselves and between the electrons and ions. r_{ij} is the distance between the ith and the jth electron.

The mass of the ion is much larger than that of an electron (M $\gg$ m), so that the characteristic time scale over which an electron changes its state is much smaller than

that associated with the motion of the ions. Hence, the ion-cores can be treated as stationary during the short time the electron state evolves. This makes it possible to solve the Schrödinger equation for the wave function of electrons alone. This is the Born-Oppenheimer approximation. The wave function may then be written in a separable form $\chi(\{\mathbf{R}_I\})\psi(\{\mathbf{r}_i\}|\{\mathbf{R}_I\})$. Thus, the Schrödinger equation for the electrons (for a given position of the ion cores $\mathbf{R_I}$) can be written as:

$$\left[-\sum_{i=1}^{N} \frac{\nabla_i^2}{2m} + v_{eI}(\{\mathbf{r}_i\}|\{\mathbf{R}_I\}) + \frac{1}{2}\sum_{i,j}\frac{1}{r_{ij}}) \right] \psi(\{\mathbf{r}_i\}|\{\mathbf{R}_I\}) = E_e(\{\mathbf{R}_I\})\psi(\{\mathbf{r}_i\}|\{\mathbf{R}_I\}) \quad (2.3)$$

The total energy of the system is a sum of electron and ion-core energies. The problem in trying to solve this equation is the number of variables involved. This issue has been brilliantly put forward by Hartree :"The tabulation of one variable requires a page, of two variables a volume, and of three variables a library; but the full specification of a single wave function of neutral Fe is a function of seventy eight variables. It would be rather crude to restrict to ten the number of values at which to tabulate this function, but even so, full tabulation of it would require 10^{78} entries, and even if this number could be reduced somewhat from considerations of symmetry, there would still not be enough atoms in the whole solar system to provide the material for printing such a table." Thus the interpretation of the solution is a 'difficult' problem. We quote Feynman "The trouble with quantum mechanics is not only in solving the equations, but in understanding what the solutions mean."

Attempts to solve these problems due to the immensely large number of variables and lack of easy interpretation has led to the development of newer approaches. An important class of methods has been based on the variational principle where one minimizes the quantity

$$\tilde{E} = \langle \tilde{\Psi}|H|\tilde{\Psi}\rangle \quad (2.4)$$

using suitable forms of the trial function $\tilde{\Psi}$ mainly guided by the one-particle orbital picture leading to single particle self-consistent field schemes like Hartree, Hartree-Fock and multi-configuration methods. However, due to the computational expense the routine application of such methods to realistic models of systems of interest is not practical and not likely to become so despite rapid advances in computer technology. So, the question

that arises is - *Is it necessary to solve the Schrödinger equation and determine the 3N dimensional wave function in order to compute the ground state energy?*

2.2   Avoiding the solution of the Schrödinger equation

An alternative approach has been based on the reduction to lower dimensions based on the density functional theory. For more than past three decades density functional theory has been the dominant method for the quantum mechanical simulation of periodic systems. It has been adopted by quantum chemists and is now very widely used for the simulation of energy surfaces in molecules.

Although the electronic wave function for the N electron system is a function of 3N variables, the expectation value $\langle \Psi | \hat{A} | \Psi \rangle$ can be calculated through other derived quantities that depend on less number of variables, if $\hat{A}$ is a sum of one- or two-particle operators, as is the case for the Hamiltonian. Thus, for the ion-core - electron potential energy consisting of one-particle terms, one has :

$$\int \Psi^*(\mathbf{r}_1, \mathbf{r}_2, ..., \mathbf{r}_N) \sum_i v_{eI}(\mathbf{r}_i | \{\mathbf{R}_I\}) \Psi(\mathbf{r}_1, \mathbf{r}_2, ... \mathbf{r}_N) d\mathbf{r}_1 d\mathbf{r}_2 ... d\mathbf{r}_N$$
$$= N \int d\mathbf{r} \; v_{eI}(\mathbf{r} | \{\mathbf{R}_I\}) \int \Psi^*(\mathbf{r}, \mathbf{r}_2, ..., \mathbf{r}_N) \Psi(\mathbf{r}, \mathbf{r}_2, ... \mathbf{r}_N) d\mathbf{r} d\mathbf{r}_2 ... d\mathbf{r}_N \qquad (2.5)$$

All electrons are identical, so we choose any of the variables and rename it $\mathbf{r}$ and renumber the rest $\mathbf{r}_2, \mathbf{r}_3 \dots \mathbf{r}_N$. Hence the result

$$V_{eI} = \langle \Psi | \sum_i v_{eI}(\mathbf{r}_i | \{\mathbf{R}_I\}) | \Psi \rangle = \int d\mathbf{r} \; v_{eI}(\mathbf{r} | \{\mathbf{R}_I\}) \rho(\mathbf{r}) \qquad (2.6)$$

valid for any single-particle multiplicative operator, where the single-particle density is defined as

$$\rho(\mathbf{r}) = N \int \Psi^*(\mathbf{r}, \mathbf{r}_2, ..., \mathbf{r}_N) \Psi(\mathbf{r}, \mathbf{r}_2, ... \mathbf{r}_N) \; d\mathbf{r}_2 d\mathbf{r}_3 ... d\mathbf{r}_N \qquad (2.7)$$

Similarly, for two-particle multiplicative operators such as the electron-electron repulsion, one can write

$$V_{ee} = \langle \Psi | \frac{1}{2} \sum_{i,j} \frac{1}{\mathbf{r}_{ij}} | \Psi \rangle = \frac{1}{2} \int d\mathbf{r}_1 d\mathbf{r}_2 \; \Gamma_2(\mathbf{r}_1, \mathbf{r}_2) / \mathbf{r}_{12} \qquad (2.8)$$

where the two-particle density, which gives the joint probability of finding an electron at $\mathbf{r}_1$ and an electron at $\mathbf{r}_2$, is defined as

$$\Gamma_2(\mathbf{r}_1, \mathbf{r}_2) = \frac{N(N-1)}{2} \int \Psi^*(\mathbf{r}_1, \mathbf{r}_2, ..., \mathbf{r}_N)\Psi(\mathbf{r}_1, \mathbf{r}_2, ...\mathbf{r}_N)d\mathbf{r}_3...d\mathbf{r}_N \qquad (2.9)$$

The functional Γ_2 is often referred to as the pair density.

The reduced density functions can also be expressed as the expectation values of the corresponding density operators, viz.

$$\rho(\mathbf{r}) = \langle\Psi| \sum_i \delta(\mathbf{r} - \mathbf{r}_i)|\Psi\rangle \qquad (2.10)$$

Thus we can write

$$\Gamma_2(\mathbf{r}_1, \mathbf{r}_2) = \langle\Psi| \sum_{i \neq j} \sum \delta(\mathbf{r}_1 - \mathbf{r}_i)\delta(\mathbf{r}_2 - \mathbf{r}_j)|\Psi\rangle \qquad (2.11)$$

For the kinetic energy term which involves differential operators, one can write

$$
\begin{aligned}
T &= -\langle\Psi| \sum_i \frac{\nabla_i^2}{2m_i})|\Psi\rangle \\
&= -\frac{1}{2}N \int \Psi^*(\mathbf{r}_1, \mathbf{r}_2, ..., \mathbf{r}_N) \nabla_1^2 \Psi(\mathbf{r}_1, \mathbf{r}_2, ...\mathbf{r}_N) \, d\mathbf{r}_1 d\mathbf{r}_2...d\mathbf{r}_N \\
&= -\frac{1}{2}N \int \left[\frac{\nabla_1^2}{2m_1}\Psi^*(\mathbf{r}_1, \mathbf{r}_2, ..., \mathbf{r}_N)\Psi(\mathbf{r}_1, \mathbf{r}_2, ...\mathbf{r}_N) \right]_{r_1 = r_1'} d\mathbf{r}_1 d\mathbf{r}_2...d\mathbf{r}_N \\
&= -\frac{1}{2} \int d\mathbf{r}_1 \left[\frac{\nabla_1^2}{2m_1}\gamma(\mathbf{r}_1; \mathbf{r}_1') \right]_{r_1 = r_1'} \qquad (2.12)
\end{aligned}
$$

with the first-order reduced density matrix defined as

$$\gamma(\mathbf{r}_1; \mathbf{r}_1') = N \int \Psi^*(\mathbf{r}_1', \mathbf{r}_2, ..., \mathbf{r}_N)\Psi(\mathbf{r}_1, \mathbf{r}_2, ...\mathbf{r}_N)d\mathbf{r}_2 d\mathbf{r}_3...d\mathbf{r}_N \qquad (2.13)$$

Clearly, the following relationships among the reduced density functions and matrices hold good.

$$
\begin{aligned}
\rho(\mathbf{r}_1) &= \gamma(\mathbf{r}_1, \mathbf{r}_1) \quad ; \quad \Gamma_2(\mathbf{r}_1, \mathbf{r}_2) = \Gamma_2(\mathbf{r}_1, \mathbf{r}_2; \mathbf{r}_1, \mathbf{r}_2) \\
\int \rho(\mathbf{r}_1)d\mathbf{r}_1 &= N \quad ; \quad \int \Gamma_2(\mathbf{r}_1, \mathbf{r}_2)d\mathbf{r}_1 d\mathbf{r}_2 = N(N-1) \\
\gamma(\mathbf{r}_1; \mathbf{r}_1') &= \gamma^*(\mathbf{r}_1'; \mathbf{r}_1) \quad ; \quad \rho(\mathbf{r}_1) = \frac{1}{N-1} \int \Gamma_2(\mathbf{r}_1; \mathbf{r}_2)d\mathbf{r}_2 \qquad (2.14)
\end{aligned}
$$

For spin-polarized situation one has to include the spin dependence, such that,

$$\rho(x) \equiv \rho(\mathbf{r}\ s) \quad ; \quad \int dx \rightarrow \sum_s \int d\mathbf{r} \quad ; \quad \rho(\mathbf{r}) = \sum_s \rho(x)ds$$

$$\rho(\mathbf{r}) = \rho_\uparrow(\mathbf{r}) + \rho_\downarrow(\mathbf{r}) \qquad s(\mathbf{r}) = \rho_\uparrow(\mathbf{r}) - \rho_\downarrow(\mathbf{r}) \tag{2.15}$$

The total energy can thus be expressed in terms of the reduced density matrices (RDM) as

$$E[\rho, \gamma, \Gamma_2] = T[\gamma(\mathbf{r}_1; \mathbf{r}_1^{'})] + V_{eI}[\rho(\mathbf{r})] + V_{ee}[\Gamma_2(\mathbf{r}_1, \mathbf{r}_2)] + V_{II} \tag{2.16}$$

where V_{II} is the ion-core - ion-core interaction energy. This leads to the possibility of developing the quantum mechanics of many-electron systems in reduced space in terms of the RDM's bypassing the wave function. One of the important requirements is the possibility of direct determination of RDM by minimizing the energy with respect to the RDM's for which the effect of the Pauli exclusion principle has to be built-in into the RDM's. The existence of an antisymmetric ψ from which the RDM's can be obtained has to be guaranteed.

This is the so called N-representability problem which has to be solved by imposing necessary and sufficient conditions on $\gamma_1(\mathbf{r}_1; \mathbf{r}_1^{'})$ and $\Gamma_2(\mathbf{r}_1, \mathbf{r}_2)$, which are unfortunately not yet known. The N-representability conditions on $\rho(\mathbf{r})$ are however known and are very simple, viz.

$$\int \rho(\mathbf{r})d\mathbf{r} = N; \qquad \rho(\mathbf{r}) \geq 0. \tag{2.17}$$

This makes the single-particle density (simplest reduced quantity) a promising candidate for the formulation of quantum mechanics in reduced space. Some of the many advantages for the electron density $\rho(\mathbf{r})$ to be the basic variable are :

(a) it is a function in 3D space in which we live and perceive,

(b) it is simpler to tabulate and plot,

(c) it provides a better visualization and

(d) it is an experimental observable, thus enabling one to compare the results of theoretical calculations directly with experiments.

The question now is whether it is possible to develop a quantum theory in terms of density alone bypassing the wave function, for which one has to ensure if (a) the density contains sufficient information (b) calculation of the properties and the energy is possible from the density alone (c) it is possible to develop a method for the direct calculation of density.

The possibility of a density description of many-electron systems has been explored by many people leading to the so called density functional theory (DFT). Although the first DFT, viz. The Thomas Fermi method has existed since 1927, the birth of modern DFT has been through the formal proof of a theorem by Hohenberg and Kohn (1964).

2.3   Hohenberg-Kohn Theorem

The Hohenberg-Kohn Theorem [Hohenberg and Kohn 1964] establishes the density as the basic variable. This theorem states that the ground-state density $\rho(\mathbf{r})$ of a bound system of interacting electrons in an external potential $v(\mathbf{r})$ determines this potential uniquely (up to an uninteresting additive term).

Consider the ground states of two N-electron systems characterized by the two external potentials (differing by more than an additive constants) $v_1(\mathbf{r})$ and $v_2(\mathbf{r})$ with corresponding Hamiltonian:

$$H_1 = T + U + \sum_i v_1(r_i) \quad ; \quad H_2 = T + U + \sum_i v_2(r_i)$$

where

$$T = -\frac{1}{2}\sum_i^N \nabla_i^2 \quad \text{and} \quad U = \frac{1}{2}\sum_{i \neq j} \frac{1}{|\mathbf{r}_i - \mathbf{r}_j|}$$

with the corresponding Schrödinger equation, $H_1\psi_1 = E_1\psi_1; H_2\psi_2 = E_2\psi_2$ and we assume that the two wave functions ψ_1 and ψ_2 yield the same density as,

$$\rho(\mathbf{r}) = N \int \psi_{1|2}^*(\mathbf{r}, \mathbf{r}_2, ..., \mathbf{r}_N)\psi_{1|2}(\mathbf{r}, \mathbf{r}_2, ...\mathbf{r}_N) \; d\mathbf{r}_2 d\mathbf{r}_3...d\mathbf{r}_N \qquad (2.18)$$

Now,

$$
\begin{aligned}
E_1 &= \langle \Psi_1 | H_1 | \Psi_1 \rangle \le \langle \Psi_2 | H_1 | \Psi_2 \rangle \\
&\le \langle \Psi_2 | H_2 | \Psi_2 \rangle + \langle \Psi_2 | H_1 - H_2 | \Psi_2 \rangle \\
&\le E_2 + \int dr \rho(r) [v_1(\mathbf{r}) - v_2(\mathbf{r})].
\end{aligned}
\tag{2.19}
$$

Now, similarly one could show that,

$$
E_2 \le E_1 + \int dr \rho(r) [v_2(\mathbf{r}) - v_1(\mathbf{r})].
\tag{2.20}
$$

Summation of the above two inequalities leads to the contradiction

$$
E_1 + E_2 \le E_2 + E_1
\tag{2.21}
$$

Hence the assumption of identical density arising from the two different external potentials is wrong. Thus a given $\rho(r)$ can only correspond to only one $v(\mathbf{r})$ and since $v(\mathbf{r})$ is fixed, the Hamiltonian and hence the wave functions are also fixed by density $\rho(\mathbf{r})$. Since the wave function is a functional of density, the energy functional $E_v[\rho]$ for a given ion-core - electron potential $v_{eI}(\mathbf{r})$ is a unique functional of density. It can also be directly proved that this energy functional assumes a minimum value for the true density.

The minimization of $E_v[\rho]$ subject to the constraint of normalized density, as given by Eqn.(2.17), leads to the Euler equation for the direct calculation of density, viz.

$$
\delta[E_v[\rho] - \mu \int \rho(\mathbf{r})d\mathbf{r} - N] = 0
$$
$$
\frac{\partial E}{\partial \rho} - \mu = 0 \Rightarrow \mu = \frac{\partial E}{\partial \rho} = v(\mathbf{r}) + \frac{\partial F}{\partial \rho}.
\tag{2.22}
$$

The essence of the problem now is to obtain an expression for the energy functional in terms of density which has the general form

$$
E_v[\rho] = \int v_{eI}(\mathbf{r})\rho(\mathbf{r})d\mathbf{r} + F[\rho]
$$

where $F[\rho]$ is a universal functional of density. Comparing with the energy functional in terms of the RDM's, i.e.,

$$E_v[\rho, \gamma, \Gamma_2] = T[\gamma] + \int v_{eI}(\mathbf{r})\rho(\mathbf{r})d\mathbf{r} + \frac{1}{2}\int\int \frac{\Gamma_2(\mathbf{r}_1, \mathbf{r}_2)}{\mathbf{r}_{12}}d\mathbf{r}_1 d\mathbf{r}_2 \tag{2.23}$$

and using the decomposition

$$\Gamma_2(\mathbf{r}_1, \mathbf{r}_2) = \rho(\mathbf{r}_1)\rho(\mathbf{r}_2)[1 - f(\mathbf{r}_1, \mathbf{r}_2)] \tag{2.24}$$

where $f(\mathbf{r}_1, \mathbf{r}_2)$ is the correlation function, one can separate out from the electron-electron repulsion term, the classical electrostatic contribution

$$E_{coul}[\rho] = \frac{1}{2}\int\int \frac{\rho(\mathbf{r}_1)\rho(\mathbf{r}_2)}{\mathbf{r}_{12}}d\mathbf{r}_1 d\mathbf{r}_2 \tag{2.25}$$

The exact kinetic energy functional $T[\rho]$ is usually replaced by the kinetic energy of a system of non-interacting particles $T_s[\rho]$ and the contribution from the electron-electron interaction energy other than the classical electrostatic contribution and the difference $T[\rho] - T_s[\rho]$ constitute what is known as the exchange-correlation (xc) energy functional $E_{xc}[\rho]$. Thus, one can write

$$E_v[\rho] = \int v(\mathbf{r})\rho(\mathbf{r})d(\mathbf{r}) + E_{coul}[\rho] + T_s[\rho] + E_{xc}[\rho]. \tag{2.26}$$

Thus E_{xc} is simply the sum of the error made in treating the electrons classically and in the error made in using a non-interacting kinetic energy. We note at this point that the nomenclature in general use and also used in the present context, exchange-correlation (xc) energy functional is quite misleading for as stated above the E_{xc} contains an element of the kinetic energy and is not the sum of the exchange and correlation energies.

The scheme for obtaining the non-interacting kinetic energy functional $T_s[\rho]$ for a certain $\rho(\mathbf{r})$ is through the solution of the one-particle Schrödinger equations

$$\left[-\frac{1}{2}\nabla^2 + \lambda(\mathbf{r})\right]\psi_i = \epsilon_i\psi_i \tag{2.27}$$

for a suitably chosen $\lambda(\mathbf{r})$ such that the resulting orbitals yield the density as

$$\rho(\mathbf{r}) = \sum_i |\psi_i|^2 \tag{2.28}$$

and then evaluating the functional as

$$T_s[\rho] = \sum_i \epsilon_i - \int dr\, \lambda(\mathbf{r})\rho(\mathbf{r}). \tag{2.29}$$

The energy functional that is to be minimized for determining the correct equilibrium density is then given by

$$E_v[\rho] = \sum_i \epsilon_i - \int dr\, \lambda(\mathbf{r})\rho(\mathbf{r}) + \int v_{eI}(\mathbf{r})\rho(\mathbf{r})d(\mathbf{r}) + E_{coul}[\rho] + E_{xc}[\rho] \tag{2.30}$$

which leads to the variational condition

$$\partial E_v[\rho] = 0 = \sum_i \nabla \epsilon_i - \int dr\, \delta\lambda(\mathbf{r})\rho(\mathbf{r}) + \int \delta\rho(\mathbf{r})[-\lambda(\mathbf{r}) + v_{eI}(\mathbf{r}) + \frac{\partial E_{coul}}{\partial \rho(\mathbf{r})} + \frac{\partial E_{xc}}{\partial \rho(\mathbf{r})} \tag{2.31}$$

Considering the expression for ϵ_i,

$$\epsilon_i = -\langle \Psi_i | \frac{1}{2} \nabla_i^2 |\Psi_i\rangle + \langle \Psi_i | \lambda(\mathbf{r}) |\Psi_i\rangle \tag{2.32}$$

we get,

$$
\begin{aligned}
\delta\epsilon_i &= \langle \nabla\Psi_i | \frac{1}{2} \nabla_i^2 |\Psi_i\rangle + \langle \nabla\Psi_i | \lambda(\mathbf{r}) |\Psi_i\rangle + c.c. + c.c. + \langle \Psi_i | \nabla\lambda(\mathbf{r}) |\Psi_i\rangle \\
&= \epsilon_i \nabla \langle \Psi_i |\Psi_i\rangle (= 0) + \langle \Psi_i | \nabla\lambda(\mathbf{r}) |\Psi_i\rangle
\end{aligned} \tag{2.33}
$$

and hence the result:

$$\sum \nabla \epsilon_i = \int dr\, \rho(\mathbf{r})\nabla\lambda(\mathbf{r}) \tag{2.34}$$

which in combination with the variational condition leads to the result

$$\nabla E_v[\rho] = 0 = \int dr\, \nabla\rho(\mathbf{r})[-\lambda(\mathbf{r}) + v_{eI}(\mathbf{r}) + \frac{\partial E_{coul}}{\partial \rho(\mathbf{r})} + \frac{\partial E_{xc}}{\partial \rho(\mathbf{r})}] \tag{2.35}$$

Since the variation of $\nabla\rho(\mathbf{r})$ is arbitrary, the bracketed quantity must be zero and hence one has

$$\lambda(\mathbf{r}) = v_{eI}(\mathbf{r}) + \frac{\partial E_{coul}}{\partial \rho(\mathbf{r})} + \frac{\partial E_{xc}}{\partial \rho(\mathbf{r})} \tag{2.36}$$

This clearly shows that if one chooses $\lambda(\mathbf{r})$ given by this expression, the single particle Schrödinger equation leads to the correct density for the system.

This provides the basis for the Kohn-Sham (K-S) density functional scheme which involves solution of a set of N nonlinear integro-differential equations:

$$[-\tfrac{1}{2} \bigtriangledown^2 + v_{eff}(\mathbf{r}; \rho)]\psi_i = \epsilon_i \psi_i$$

with the effective potential given by

$$v_{eff}(\mathbf{r}) = v_{eI}(\mathbf{r}) + \int \frac{\rho(\mathbf{r}')}{|\mathbf{r} - \mathbf{r}'|} d\mathbf{r}' + \frac{\delta E_{xc}}{\delta \rho(\mathbf{r})} = \phi(\mathbf{r}) + \frac{\delta E_{xc}}{\delta \rho(\mathbf{r})} \tag{2.37}$$

where, $\bigtriangledown^2 \phi = 4\pi \rho(\mathbf{r})$ and the density is calculated as

$$E_v[\rho] = \sum_i \epsilon_i - \frac{1}{2} \int \int \frac{\rho(\mathbf{r})\rho(\mathbf{r}')}{|\mathbf{r} - \mathbf{r}'|} d\mathbf{r} d\mathbf{r}' + E_{xc}[\rho] - \int d\mathbf{r}\rho(\mathbf{r})\frac{\partial E_{xc}}{\partial \rho(\mathbf{r})} \tag{2.38}$$

for spin-polarized situations, incorporating the spin-components of the density as well we have,

$$E_v[\rho_\alpha, \rho_\beta] = T_s + \int v(\mathbf{r})\rho(\mathbf{r})d(\mathbf{r}) + E_{coul}[\rho] + T_s[\rho] + E_{xc}[\rho_\alpha, \rho_\beta]. \tag{2.39}$$

and the Kohn-Sham equation under the spin-polarized situation becomes

$$[-\frac{1}{2} \bigtriangledown^2 + v_{eff}(\mathbf{r}; \rho_\sigma)]\psi_{k\sigma} = \epsilon_{k\sigma}\psi_{k\sigma} \tag{2.40}$$

with an effective potential given by

$$v_{eff,\sigma}(\mathbf{r}) = v(\mathbf{r}) + \int \frac{\rho(\mathbf{r}')}{|\mathbf{r} - \mathbf{r}'|} d\mathbf{r}' + \frac{\nabla E_{xc}[\rho_\alpha, \rho_\beta]}{\nabla \rho_\sigma(\mathbf{r})} \tag{2.41}$$

The corresponding density is given by

$$\rho(\mathbf{r}) = \sum_i |\psi_{k\sigma}|^2$$

This set of non-linear equations (the Kohn-Sham equations) describes the behaviour of non-interacting "electrons" in an effective local potential. For the exact functional, and thus exact local potential, the "orbitals" yield the exact ground state density and corresponding energy. The Kohn-Sham approach gives an exact correspondence of the density and ground state energy of a system consisting of non-interacting Fermions and the "real" many body system described by the Schrödinger equation. The correspondence of the charge density and energy of the many-body and the non-interacting system is only exact if the exact functional is known. In this sense Kohn-Sham density functional theory is an empirical methodology - we do not know (and have no way of systematically approaching) the exact functional. However the functional is universal - it does not depend on the materials being studied. For any particular system we could, in principle, solve the Schrödinger equation exactly and determine the energy functional and its associated potential. This, of course, involves a greater effort than a direct solution for the energy. Nevertheless, the ability to determine the exact properties of the universal functional in a number of systems allows excellent approximations to the functional to be developed and used in unbiased and thus predictive studies of a wide range of materials -a property usually associated with an *ab initio* theory. In practice, the utility of the theory rests on the approximation used for $E_{xc}[\rho]$.

2.4   The Local density approximation for $E_{xc}[\rho]$

The generation of approximations for E_{xc} has lead to a large and still rapidly expanding field of research. There are now many different flavours of functional available which are more or less appropriate for any particular study. In the early days practical implementations of density functional theory was dominated by one particular system for which near exact results could be obtained - the homogeneous electron gas. In this system the electronic charge density (ρ) is uniform due to a constant external potential faced by the electrons.

Thomas and Fermi studied the homogeneous electron gas in the early twentieth century[Fermi and Thomas 1928,1927]. The orbitals of the system are, by symmetry, plane waves. If the electron-electron interaction is approximated by the classical Hartree poten-

tial (that is exchange and correlation effects are neglected) then the total energy functional can be readily computed. Under these conditions the dependence of the kinetic and exchange energy on the density of the electrons can be extracted and expressed in terms of a local functions of density. This suggests that in the inhomogeneous system we might approximate the functional as an integral over a local function of the charge density. Using the kinetic and exchange energy densities of the non-interacting homogeneous electron gas this leads to;

$$T[\rho] = 2.87 \int \rho^{\frac{5}{3}}(\mathbf{r})d\mathbf{r} \tag{2.42}$$

and

$$E_x[\rho] = 0.74 \int \rho^{\frac{4}{3}}(\mathbf{r})d\mathbf{r} \tag{2.43}$$

These results are highly suggestive of a representation for E_{xc} in an inhomogeneous system. The local exchange correlation energy per electron might be approximated as a simple function of the local charge density (say, $\epsilon_{xc}^{LDA}(\rho)$). That is, an approximation of the form;

$$E_{xc}^{LDA}[\rho] = \int \rho(\mathbf{r})\epsilon_{xc}^{LDA}(\rho(\mathbf{r}))d\mathbf{r} \tag{2.44}$$

An obvious choice is then to take $\epsilon_{xc}^{LDA}(\rho)$ to be the exchange and correlation energy density of the uniform electron gas of density ρ - this is the *local density approximation (LDA)*. Within the LDA $\epsilon_{xc}^{LDA}(\rho)$ is a function of only the local value of the density. It can be separated into exchange and correlation contributions;

$$\epsilon_{xc}^{LDA}(\rho) = \epsilon_x^{LDA}(\rho) + \epsilon_c^{LDA}(\rho) \tag{2.45}$$

The Dirac form can be used for E_x^{LDA};

$$\epsilon_x^{LDA}(\rho) = -C\rho^{\frac{1}{3}} \tag{2.46}$$

Where for generality an arbitrary free constant, C, has been introduced rather than that determined for the homogeneous electron gas. This functional form is much more

widely applicable. The functional form for the correlation energy density, ϵ_c^{LDA}, is unknown and has been simulated for the homogeneous electron gas in numerical quantum Monte Carlo calculations which yield essentially exact results[Ceperley and Alder 1980]. It is a remarkably noteworthy fact that the LDA works as well as it does given the reduction of the energy functional to a simple local function of the density. One of the reasons could be that in LDA there are very significant errors in the exchange and correlation energies but, as the exchange energy is generally underestimated and the correlation energy overestimated, these errors tend to cancel. The success of the LDA is in part due to this cancellation of errors.

Further insight into the behaviour of functionals can be obtained by examining how well they approximate Γ_2 - the probability of finding an electron at $\mathbf{r}_1$ and an electron at $\mathbf{r}_2$. LDA seems to make a very poor approximation of Γ_2. So, we are faced with the question - how can the LDA produce such reasonable energetics if the functional Γ_2 is so poorly described by it? The answer is based on the structure of the Coulomb operator. We remember from Eqn 2.8 that the electron-electron interaction can be written as;

$$V_{ee} = \frac{1}{2} \int d\mathbf{r}_1 d\mathbf{r}_2 \Gamma_2(\mathbf{r}_1, \mathbf{r}_2)/\mathbf{r}_{12} \tag{2.47}$$

From this it seems a poor approximation to Γ_2 leads to a poor estimate of the electron-electron interaction. However, the Coulomb operator depends only on the magnitude of the separation of $\mathbf{r}_1$ and $\mathbf{r}_2$, $\mathbf{r}_{12}$. We can re-write V_{ee} as ::

$$\begin{aligned} V_{ee} &= \frac{1}{2} \int d\mathbf{r}_1 d\mathbf{r}_{12} \Gamma_2(\mathbf{r}_1, \mathbf{r}_1 + \mathbf{r}_{12})/\mathbf{r}_{12} \\ &\quad \frac{1}{2} \int_0^\infty 4\pi |\mathbf{r}_{12}|^2 [\frac{\int \Gamma_2(\mathbf{r}_1, \mathbf{r}_1 + \mathbf{r}_{12})}{\mathbf{r}_{12}} \frac{d\Omega_{r_{12}}}{4\pi}] dr_{12} \end{aligned} \tag{2.48}$$

Thus the electron-electron interaction depends only on the spherical average of the pair density - $P(\mathbf{r}_{12})$;

$$P(\mathbf{r_{12}}) = \int \mathbf{\Gamma_2}(\mathbf{r_1}, \mathbf{r_1} + \mathbf{r_{12}}) d\mathbf{r_1} \frac{\mathbf{d\Omega_{r_{12}}}}{\mathbf{4\pi}} \tag{2.49}$$

The LDA makes a reasonable approximation to this spherically averaged pair density. This explains in part the success of the LDA.

Thus, we can conclude that the remarkable performance of the LDA is a consequence of its reasonable description of the spherically averaged pair density along with the tendency

for errors in the exchange energy density to be canceled by errors in the correlation energy density.

2.5   The Generalized Gradient Approximation for E_{xc}

In the generalized gradient approximation (GGA) the exchange-correlation functional E_{xc} depends on the density and its derivative,

$$E_{xc}^{GGA}[\rho] = \int \rho(\mathbf{r}) \epsilon_{xc}^{GGA}(\rho(\mathbf{r}), |\bigtriangledown \rho(\mathbf{r})|) d\mathbf{r} \qquad (2.50)$$

Now one can use the GGA functionals by Perdew and Wang [Wang 1996], by Perdew, Burke and Ernzerhof (PBE)[Perdew *et.al.* 1996] and Becke's formula[Becke 1988] for the exchange part combined with Perdew's 1986 formula for correlation [Perdew 1986]. The GGA improves significantly on the LDA's description of the binding energy of molecules - it was this feature which lead to the very wide spread acceptance of DFT in the chemistry community during the early 1990's. We use the PBE functional mostly for DFT-based calculations in this thesis.

2.6   Solution of the Kohn-Sham Equation

The Kohn-Sham orbitals are required to be expanded in a suitable basis set in order to be solved. The basis set can either be fixed energy dependent like plane waves or linear combination of the atomic orbitals or energy dependent partial wave-like basis. Plane wave basis has been found to be useful for the calculation of systems like clusters and solids. Plane wave basis expansion is mathematically simple. By using the pseudo-potential approach the size of the basis set required can be reduced making the calculation computationally less expensive.

2.6.1   Plane Waves and Pseudo-potentials

Plane wave basis are orthonormal and energy independent. Thus they convert the Kohn-Sham equation to a simple matrix eigenvalue problem for the expansion coefficients. More-over, plane waves are atom and atomic position independent. In such calculations , the

single electron wave function is expanded using plane wave basis $\exp(i\mathbf{G}.\mathbf{r})$, where the candidate G's are the reciprocal vectors of the unit cell used. The biggest advantage of plane wave basis is its ability to perform the exact variational calculation based on a discrete numerical grid, i.e., instead of doing actual real space integrations, we can do a summation over a real space grid, the results are exactly the same.

The plane wave calculations require that the wave function be described by plane waves within a certain energy cut-off E_{cut}. In order to reduce E_{cut} to a reasonable value the wave function should be smooth. While it is often smooth at the chemically important bonding area, near the nuclei, the valence wave functions often have a lot of wiggles. These wiggles must exist so that the valence wave functions are orthogonal to the deep level core wave functions. Besides, it is difficult to describe those chemically-not-important core wave functions using plane wave basis. To overcome these difficulties, pseudo-potentials are developed. Basically, using a Pseudo-potentials, the core states will no longer exist, and the valence pseudo-wave functions become smooth near the nuclei. Using this technique the unwanted singular behaviour of the ionic potential at the lattice points can be removed. A good pseudo-potential wave function should be soft and transferable. A pseudo-potential is soft if it requires less number of plane waves. A pseudo-potential is transferable if it works considerably well in different environments. However, to have these good properties, it is necessary to have different pseudo-potentials for s,p,d states, i.e, the pseudo-potential is angular momentum dependent (non-local pseudo-potential).

2.6.2   Projector Augmented Wave

The drawback of the pseudo-potential method is that all information on the full wave function close to the nuclei is lost. This can influence the calculation of certain properties, such as hyperfine parameters, and electric field gradients. Another problem is that one has no before hand knowledge of when the approximation yields reliable results.

A different approach is the augmented-plane-wave method(APW), in which space is divided into atom-centered augmented spheres inside which the wave functions are taken as some atom-like partial waves, and a bonding region outside the spheres, where some envelope functions are defined. The partial waves and envelope functions are then matched

at the boundaries of the spheres. A more general approach is the projector augmented wave method (PAW) which is used in this thesis, which offers APW as a special case and the pseudo-potential method as a well defined approximation. The PAW method was first proposed by Blöchl[Blöchl 1994].

The projector augmented wave (PAW) method separates the Kohn-Sham wave functions, which displays rapid oscillations in some parts of space, and smooth behaviour in other parts of space into auxiliary functions which are smooth everywhere and a contribution which contains rapid oscillations, but only contributes in certain, small, areas of space. Having separated the different types of waves they can be treated individually. Thus the Kohn-Sham total energy E can be separated into a part calculated on smooth functions, $\tilde{E}$, and some atomic corrections, ΔE^a, involving quantities localized around the nuclei only

$$E = \tilde{E} + \sum_a \Delta E^a \tag{2.51}$$

where the smooth part $\tilde{E}$ is the usual energy functional, but evaluated on the smooth functions $\tilde{\rho}$ instead of ρ and with the soft compensation charges $\tilde{Z}$ instead of nuclei charges $Z(\mathbf{r})$.

Chapter 3

A study of the electronic structure of bimetallic Mn-Co clusters

3.1 Introduction

In this chapter[1] we shall systematically and thoroughly investigate the structural, electronic and magnetic properties of Mn-Co clusters within the *ab-initio* pseudo-potential plane wave method using generalized gradient approximation for the exchange correlation energy. In Co-rich clusters the magnetic moment is enhanced by Mn addition unlike in the bulk. Certain Mn rich clusters are found to be ferri-magnetic. The enhancement of magnetic moment of Mn-Co clusters when a Co atom is replaced by a Mn atom is found to be independent of the size and composition (as long as there is no change in the magnetic nature of the cluster on Mn inclusion). The interplay of bond lengths and coordination in determining the magnetic moment of clusters is also analyzed in this chapter.

Nanoalloy clusters have received considerable attention for their peculiar catalytic, optical, magnetic, electronic, and geometric properties [Jellinek and Krissinel 1999, Kondow, 2003, Klabunde 1994, Andrews *et.al.* 1992, Jellinek 2008]. For such clusters, chemical and physical properties can be tailored by varying not only the size but also the composition for a specific purpose. This opens the way to a large variety of potential applications in areas such as high-density recording [Sun *et.al.* 2000], catalysis [Sinfelt 1983, Molenbroek *et.al.* 2001, Hansen *et.al.* 1997], optics [Shibata *et.al.* 2002,

---

[1]The contents of this chapter has been published : Shreemoyee Ganguly, Mukul Kabir, Soumendu Datta, Biplab Sanyal and A. Mookerjee, *Magnetism in small bimetallic Mn-Co clusters*, Phys. Rev. B **78**, 014402 (2008)

Darby *et.al.* 2002, Ruban *et.al.* 1999] and biomedical [Loo *et.al.* 2005]. Particularly, the interest in transition metal clusters arises from a desire to seek a solution to the technologically important question: how magnetic properties change in reduced dimensions? The candidates chosen for the present study, Mn and Co have very interesting properties in low dimensions. Manganese, though anti-ferromagnetic as bulk, shows finite magnetic moment in reduced dimension [Knickelbein 2001, Knickelbein 2004, Kabir *et.al.* 2006, Kabir *et.al.* 2007] whereas, Cobalt shows enhanced magnetic moment compared to the bulk [Xu *et.al.* 2005, Knickelbein 2006, Datta *et.al.* 2007]. Therefore, it will be interesting to see how the properties of the bimetallic cluster formed out of these two elements change with composition, atomic ordering, and size.

The first step to the study of cluster properties is the determination of the ground state structures and the complexity to locate that increases with the cluster size as the number of local minima in the potential energy surface increases. This leaves a number of possible geometric and/or magnetic isomers in pure clusters for each size. Compared to the pure clusters, in alloy clusters "homotops" [Jellinek and Krissinel 1999] are possible in addition to such usual isomers. Jellinek introduced the term "homotop" to describe A_xB_y alloy cluster isomers, with a fixed size ($x+y=n$) and composition (x/y ratio), which have the same geometrical arrangement of atoms, but differ in the way A- and B-type atoms are arranged. Due to the presence of these homotops, there arises a large number of combinatorial possibilities which makes the finding of lowest energy structures for alloy clusters even more computationally expensive task than that for pure clusters. Thus most of the theoretical studies done on bimetallic alloy clusters take resort to some empirical many body potential to reduce the computational expense [Jellinek and Krissinel 1999, Christensen *et.al.* 1995, Lopez *et.al.* 1996, Jellinek *et.al.* 1996, Krissinel and Jellinek 1997, Krissinel and Jellinek 1997, Jellinek *et.al.* 1999]. Our study is one of the very few which uses an *ab-initio* methodology for transition metal nano-alloy clusters. Here we study bimetallic Mn_xCo_y clusters in the size ranging from 2 to 5 for all possible stoichiometry. Using first-principles DFT we study the evolution of structural, electronic and magnetic properties as we change the size and composition. The interplay between these properties yield many interesting features. Such features are analyzed in greater depth through density of states and partial charge density.

In earlier works, we have studied pure Mn_n (Refs. [Kabir *et.al.* 2006, Kabir *et.al.* 2007]) and Co_n (Ref. [Datta *et.al.* 2007]) clusters. A transition from ferromagnetic to ferri-magnetic Mn-Mn coupling is observed at $n = 5$ for Mn_n clusters and the ferri-magnetic states continue to be the ground state for larger clusters. On the other hand, pure Co_n clusters are found to be ferromagnetic with magnetic moment higher than the bulk. Calculated magnetic moments of pure Mn_n and Co_n clusters show very good agreement with the Stern-Gerlach molecular beam experiments [Knickelbein 2001, Knickelbein 2004, Xu *et.al.* 2005, Knickelbein 2006].

Neutron scattering studies of bulk Mn_xCo_{1-x} alloy have been used to determine the variation of individual atomic moments, μ_{Mn} and μ_{Co}, with increasing Mn:Co ratio [Knick-elbein 2007, Cable 1982, Men'shikov 1985]. On the Co-rich side, μ_{Mn} and μ_{Co} are aligned antiferro-magnetically, with the magnitude of both μ_{Co} and μ_{Mn} decreasing monotonically with increasing Mn content such that the mean per-atom moment $(\bar{\mu})$ of the alloy also decreases strongly with Mn content. In fact, $\bar{\mu}$ decreases from 1.72 μ_B for $x=0$ to 0 μ_B for $x=0.32$ (Ref. [Matsui *et.al.* 1970]). However, small Mn-Co clusters have been found to behave in a completely different way [Knickelbein 2007, Yin *et.al.* 2007]. Recently, Knick-elbein has found that unlike bulk Mn_xCo_{1-x} alloys, in which the presence of Mn forces the mean per-atom moment to decrease, the significant presence of Mn in medium sized Mn_xCo_y ($n=x+y=11-29$) clusters results in overall magnetic moment that are compara-ble to those of the corresponding pure Co_n clusters, and in some cases (e.g. $n=11-14$) even larger. More recently Yin *et al.* have measured the magnetic moments of Mn_xCo_y ($y \leq 60$; $x \leq y/3$) clusters and found an increase in per-atom magnetic moment for Co-rich Mn_xCo_y cluster with increasing Mn concentration [Yin *et.al.* 2007]. This enhancement in moment due to Mn doping is independent of cluster size and composition. On the other hand, for Mn-rich clusters, for more than 40% Mn concentration, the average magnetic moment of Mn_xCo_y cluster decreases with increasing Mn concentration. This suggests that unlike bulk Mn-Co alloys, both Mn and Co within the small Mn-Co clusters retain substantial moments even at high Mn fractions. However, the magnitudes of individual Mn and Co moments could not be measured, and consequently the nature of magnetic coupling can not be concluded in a SG experiment. Motivated by these recent SG ex-periments, [Knickelbein 2007, Yin *et.al.* 2007] in the present chapter, we study Mn_xCo_y

clusters from first-principles in the size range n=2-5. In order to make a direct comparison to the experiments we also study Mn_2Co_{11} cluster, which lies within the experimental regime [Knickelbein 2007].

3.2   Computational Details

Calculations are performed using DFT based pseudo-potential plane wave method [Kresse *et.al.* 1999]. We have chosen the projector augmented wave method, [Blöchl 1994] and used the Perdew-Bruke-Ernzerhof exchange-correlation functional [Perdew *et.al.* 1996] for the spin-polarized generalized gradient correction. The $3d$ and $4s$ electrons of Mn and Co are treated as valence electrons. The wave functions are expanded in a plane wave basis set within 270 eV kinetic energy. Reciprocal space integrations are carried out at the Γ point. Symmetry unrestricted optimizations (of both geometry and spin) are performed using the conjugate gradient and quasi-Newtonian methods until all the force components are less than a threshold value of 0.005 eV/A. Simple cubic supercells are used with periodic boundary conditions, and it is made sure that two neighboring clusters are separated by at least 10 A vacuum space. This ensures that the interaction of a cluster with its periodic image is negligible. Earlier we have used same methodology to study pure Mn_n and Co_n clusters [Kabir *et.al.* 2006, Datta *et.al.* 2007]. For each cluster size all possible "homotops" have been considered for several geometric structures with all possible compositions. We have also considered all possible spin multiplicities for each of these structures. These ensures the robustness for the ground state search. It should be mentioned here that calculations are done within the collinear spin assumption.

The binding energy per atom (E_B) is defined as,

$$E_B(\mathrm{Mn}_x\mathrm{Co}_y) = \frac{1}{n}[xE(\mathrm{Mn}) + yE(\mathrm{Co}) - E(\mathrm{Mn}_x\mathrm{Co}_y)], \qquad (3.1)$$

where x (y) is the number of Mn (Co) -atoms in $\mathrm{Mn}_x\mathrm{Co}_y$ cluster, $n(= x + y)$ is the cluster size and $E(\mathrm{Mn}_x\mathrm{Co}_y)$, $E(\mathrm{Mn})$, and $E(\mathrm{Co})$ are the total energies of $\mathrm{Mn}_x\mathrm{Co}_y$ cluster, and an isolated Mn- and Co-atom, respectively. For a given n and for a certain composition, the structure with the highest binding energy is considered to be the *ground*

state. The local magnetic moment μ_X at X-atom can be calculated from,

$$\mu_X = \int_0^R [\rho_\uparrow(\mathbf{r}) - \rho_\downarrow(\mathbf{r})] \, d\mathbf{r} \tag{3.2}$$

where $\rho_\uparrow(\mathbf{r})$ and $\rho_\downarrow(\mathbf{r})$ are spin-up and spin-down charge-densities, respectively and R is the radius of the sphere centered on the atom X. For a particular cluster, R is taken such that no two spheres overlap i.e. R is equal to half of the shortest bond length in that cluster.

3.3   Results

3.3.1   Ground states and some important isomers

It is necessary to carry out calculations for not only the ground state, but also for the low energy isomers, i.e. clusters with different geometries, homotops and different magnetic arrangements, which have energies close to that of the ground state. This is because when, in our earlier works [Kabir *et.al.* 2006, Datta *et.al.* 2007], theoretical results were compared with experimental results, it was noted that for a particular size of cluster, the isomers with different magnetic moments are likely to be present in the SG beam with a statistical weight and essentially the measured magnetic moment is the weighted average of the moments of all those isomers. Previously we have extensively studied the pure Mn_n (Ref. [Kabir *et.al.* 2006]) and Co_n (Ref. [Datta *et.al.* 2007]) clusters within the same theoretical methodology. Therefore, we do not elaborate pure clusters here, rather we refer the readers to Ref. [Kabir *et.al.* 2006] and Ref. [Datta *et.al.* 2007].

$Mn_x Co_y$ *(x + y = 2):* Due to the half-filled $3d$ and filled $4s$ states and due to high $4s^2 3d^5 \rightarrow 4s^1 3d^6$ promotion energy Mn-atoms bind very weakly when they are brought together. The binding energy of Mn_2 dimer is 0.52 eV/atom and the bond length is comparatively higher than all other $3d$ transition metal dimers.Kabir *et.al.* 2006 On the other hand, Co_2 dimer has much higher binding energy (1.45 eV/atom) and smaller bond length (1.96 A) [Datta *et.al.* 2007]. Both the pure dimers are ferromagnetic with 10 (Mn_2) and 4 μ_B (Co_2) moments. The bond length of MnCo dimer is in between the pure dimers and the binding energy increases monotonically in $Mn_2 < MnCo < Co_2$ order (Table 3.1). The Mn-Co coupling is also ferromagnetic in the mixed dimer.

Table 3.1: Structure, binding energy E_B, relative energy to the ground state (GS), $\Delta E = E - E_{\text{GS}}$, per-atom magnetic moment $\bar{\mu}$ and average bond length $\langle L_B \rangle$ for the ground states of $Mn_x Co_y$ clusters with $x + y = 2$.

Cluster	Structure	E_B (eV/atom)	ΔE (eV)	$\bar{\mu}$ (μ_B/atom)	$\langle L_B \rangle$ (A)
Co_2	linear	1.45	0.00	2	1.96
MnCo	linear	1.09	0.00	3	2.06
Mn_2	linear	0.52	0.00	5	2.58

$Mn_x Co_y$ ($x + y = 3$): The linear and triangular structures were taken as initial guess and the results are shown in Fig.3.1 and Table 3.2. The ground state structure are found to be triangular for all the compositions. The pure Co_3 has two degenerate ground states. The magnetic moment is enhanced by 2 and 4 μ_B from the two degenerate ground state structures of Co_3 due to single Mn doping. For Mn_2Co the lowest energy state with a stable spin distribution [2] is ferri-magnetic, with one of the Mn atoms having opposite spin to the other Mn and Co. The closest isomer to this is a linear ferromagnetic structure. However, it lies 0.39 eV above the ground state. Here the Mn-Mn distance is large (4.54 A) causing them to be ferro-magnetically coupled. The ferromagnetic ground state of pure Mn_3 was found to be nearly degenerate with a ferri-magnetic structure [Kabir *et.al.* 2006].

$Mn_x Co_y$ ($x + y = 4$): For these clusters square and tetrahedral structures were considered. Results are summarized in Table 3.3 and some of the relaxed structures are shown in Fig.3.2. The ground state structures come out to be tetrahedral for all compositions. Co_4 has a Jahn-Teller distorted tetrahedral ground state[Datta *et.al.* 2007] similar to that obtained by Castro *et al.*,Castro 1997 and the closest isomer is a rhombus. Single Mn-substitution ($MnCo_3$) increases the ground state moment by 2 μ_B. The first isomer is a planar structure, a quadrilateral, having equal magnetic moment as the tetrahedral ground state. The next two closest isomers also have tetrahedral structure: one with average magnetic moment 0.5 μ_B/atom lower and average bond length 0.03 A shorter

---

[2]Stability of spin arrangement : a spin arrangement in any magnetic clusters is magnetically stable only if the lowest unoccupied molecular orbital (LUMO) of the majority spin lies above the highest occupied molecular orbital (HOMO) of the minority spin and vice versa.

and the other with average bond length 0.01 A longer and average magnetic moment 0.5 μ_B/atom higher than that of the ground state. Thus the isomer with higher bond length has higher moment. This trend is seen for all compositions and sizes (Tables I to IV). The closest non-ferromagnetic $MnCo_3$ isomer lies much higher (0.82 eV) than the ground state and has zero net moment.

Substitution of another Co with Mn (Mn_2Co_2) further enhances the total magnetic
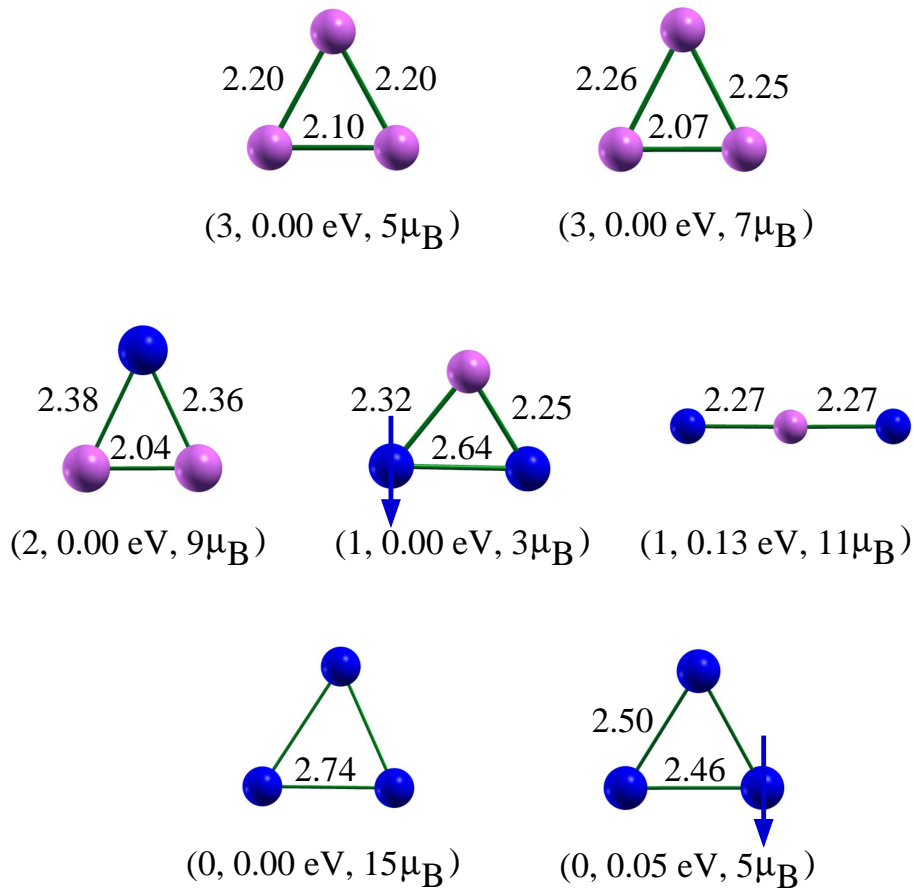
Figure 3.1: Ground state structures and significant isomers of Mn_xCo_y ($x + y = 3$) clusters. Magenta shades represent Co-atoms and blue shades represent Mn-atoms. The bond lengths are quoted in A. The numbers in the parenthesis represent the number of Co-atoms (y), difference in total energy from the corresponding ground state (ΔE), and total magnetic moment, respectively. Down arrow represents the atom with anti-parallel moment.

Table 3.2: Same as Table 3.1 for $x + y = 3$ clusters.

Cluster	Structure	E_B (eV/atom)	ΔE (eV)	$\bar{\mu}$ (μ_B/atom)	$\langle L_B \rangle$ (A)
Co$_3$	Triangular	1.78	0.00	1.67	2.16
	Triangular	1.78	0.00	2.33	2.19
MnCo$_2$	Triangular	1.67	0.00	3.00	2.26
Mn$_2$Co	Triangular	1.16	0.00	1.00	2.40
	Linear	1.12	0.13	3.67	2.27
	(with endon Mn)				
Mn$_3$	Triangular	0.82	0.00	5.00	2.74
	Triangular	0.80	0.05	1.67	2.48

moment by 2 μ_B compared to MnCo$_3$ cluster. In this case, the closest ferri-magnetic isomer, with average magnetic moment 1 μ_B/atom, lies far above (0.56 eV) from the ground state. A further substitution of a Co-atom with Mn atom (Mn$_3$Co) again leads to further 2 μ_B increase in magnetic moment. A planar (rhombus) ferri-magnetic isomer

Table 3.3: Same as Table 3.1 for $x + y = 4$ clusters.

Cluster	Structure	E_B (eV/atom)	ΔE (eV)	$\bar{\mu}$ (μ_B/atom)	$\langle L_B \rangle$ (A)
Co$_4$	Tetrahedral	2.28	0.00	2.5	2.34
	Rhombus	2.25	0.11	2.5	2.25
MnCo$_3$	Tetrahedral	2.06	0.00	3.0	2.34
	Quadrilateral	2.05	0.05	3.0	2.32
	Tetrahedral	2.02	0.18	2.5	2.31
	Tetrahedral	2.00	0.25	3.5	2.35
Mn$_2$Co$_2$	Tetrahedral	1.87	0.00	3.5	2.41
	Tetrahedral	1.82	0.22	4.0	2.46
Mn$_3$Co	Tetrahedral	1.60	0.00	4.0	2.54
	Tetrahedral	1.54	0.22	4.5	2.60
	Rhombus	1.51	0.35	1.5	2.39
Mn$_4$	Tetrahedral	1.18	0.00	5.0	2.54
	Tetrahedral	1.16	0.08	2.5	2.59
	Tetrahedral	1.13	0.20	2.0	2.58
	Tetrahedral	1.13	0.20	0.0	2.65

2.14
2.72   2.72

2.14
2.67

2.12   2.42
2.52

(4, 0.00 eV, 10 μ_B)   (4, 0.11 eV, 10 μ_B)   (3, 0.00 eV, 12 μ_B)

2.35   2.13
2.64

2.83   2.11
2.37

2.74
2.28

(3, 0.05 eV, 12 μ_B)   (2, 0.00 eV, 14 μ_B)   (1, 0.00 eV, 16 μ_B)

2.47   2.45
2.63
2.21   2.21

2.70

2.67
2.51

(1, 0.35 eV, 06 μ_B)   (0, 0.00 eV, 20 μ_B)   (0, 0.08 eV, 10 μ_B)
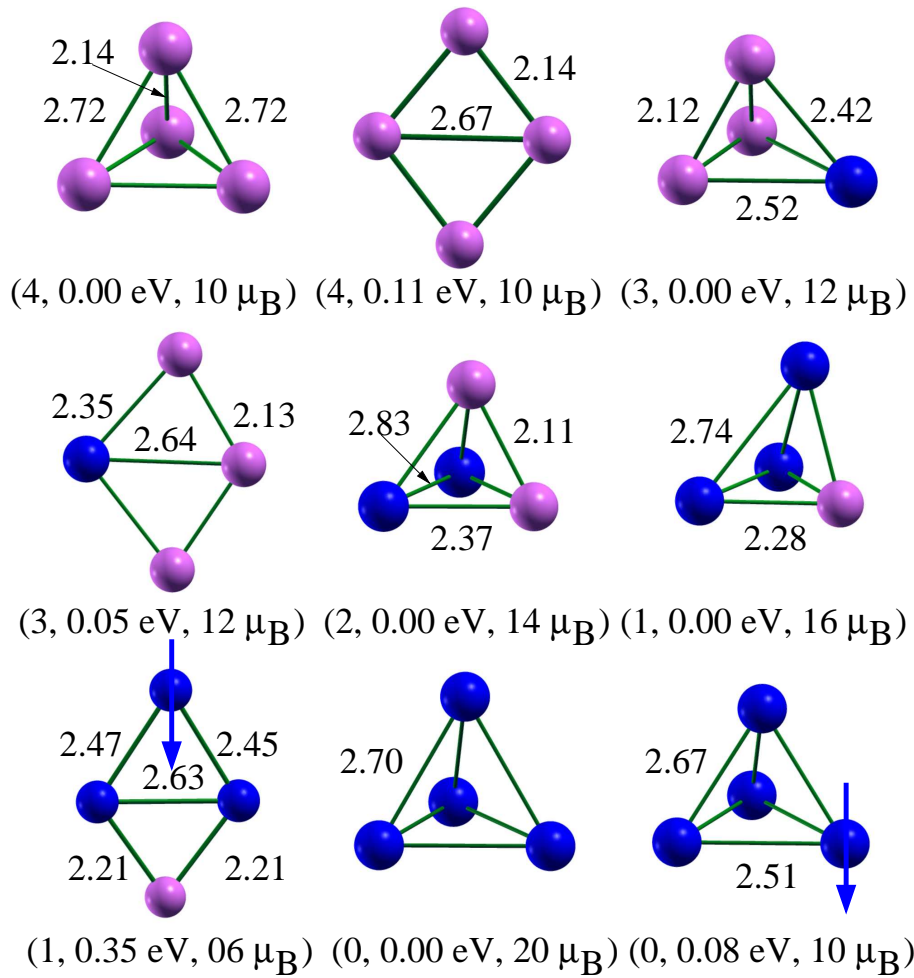
Figure 3.2: Ground state structures and significant isomers of Mn_xCo_y $(x + y = 4)$ nano-alloy clusters. Same conventions are followed as in Fig.3.1.

lies 0.35 eV above the ground state. Mn_4 has binding energy 1.07 eV/atom, which is much lower than that of Co_4 and is ferromagnetic. However, it has a close ferri-magnetic isomer, which lies only 0.08 eV higher in energy. It is interesting to note here that for these clusters with $n=4$, the energy splitting between the ferromagnetic ground state and optimal ferri-magnetic state decreases with increasing Mn.

Mn_xCo_y $(x + y = 5)$: The trigonal bi-pyramidal (TBP), square pyramidal (SQPD) and (planar) pentagonal geometries are considered as starting configurations. The results are tabulated in Table 3.4 and minimum energy structures are shown in Fig.3.3. All the

clusters with different compositions have trigonal bi-pyramidal ground state. For $MnCo_4$ cluster, the ground state magnetic moment is enhanced by 2 μ_B compared to the pure Co-pentamer due to single Mn substitution. The single-Mn doping also enhances the energy splitting between TBP and SQPD structures. We have found a similar trend in magnetic moment for Mn_2Co_3 as it is further enhanced by 2 μ_B due to another Mn-substitution. For this cluster the nearest 'homotop' lies 0.15 eV higher.

The incremental behavior of magnetic moment with Mn-substitution is no longer observed as the clusters become ferri-magnetic, when the number of Mn-atoms increase to three or more, i.e., when the clusters become Mn-rich. Thus, magnetic moment of Mn_3Co_2 drops by 4 μ_B from the pure Co_5, as in this cluster one of the Mn-atoms has anti-parallel spin alignment with the others. The first isomer found is a homotop of the ground state. A ferromagnetic homotop, which follows an increment of 2 μ_B/Mn-substitution, lies much higher (0.30 eV), and has larger ($\sim$ 2.80 A) $Mn_\uparrow$-$Mn_\uparrow$ separations. In contrast, in the ferri-magnetic ground state $Mn_\downarrow$-$Mn_\uparrow$ distance is much shorter (2.44 A) than the $Mn_\uparrow$-$Mn_\uparrow$ distance (2.88 A). This is in general true for other clusters (Fig.3.3). The Mn_4Co is also ferri-magnetic, which has $2\mu_B$ less moment than that of pure Co_5. However, it has a ferromagnetic structure which obeys the '2 μ_B/Mn-substitution increment' rule and this structure lies only 0.04 eV higher. This cluster also has two different homotops in the form of a distorted tetragonal pyramid (TGPD) and a SQPD and they lie 0.15 and 0.18 eV higher, respectively. It has previously been reported that pure Mn_5 is ferri-magnetic in its ground state and a ferromagnetic isomer lies 0.19 eV higher [Kabir *et.al.* 2006].

3.3.2   Binding energy and stability

The coordination number increases with cluster size, and thus the binding energy, which we have discussed earlier in detail for pure Mn_n and Co_n clusters [Kabir *et.al.* 2006, Kabir *et.al.* 2007, Datta *et.al.* 2007]. However, the binding energy of pure Co_n clusters are much larger than that of pure Mn_n clusters of same size. This is because the Mn-atoms have half-filled $3d$ and filled $4s$ shells and also have high $4s^23d^5 \rightarrow 4s^13d^6$ promotion energy. As a consequence, the Mn-atoms do not bind strongly when they are brought together [Kabir *et.al.* 2006, Kabir *et.al.* 2007].

Table 3.4: Same as Table 3.1 for $x + y = 5$ clusters.

Cluster	Structure	E_B (eV/atom)	ΔE (eV)	$\bar{\mu}$ (μ_B/atom)	$\langle L_B \rangle$ (A)
Co_5	TBP	2.55	0.00	2.6	2.34
	SQPD	2.52	0.15	2.6	2.27
$MnCo_4$	TBP	2.46	0.00	3	2.38
	SQPD	2.41	0.23	2.6	2.29
	SQPD	2.40	0.29	3	2.35
Mn_2Co_3	TBP	2.25	0.00	3.4	2.43
	TBP	2.24	0.03	3	2.40
	TBP	2.22	0.15	3.4	2.42
	TBP	2.22	0.15	3.4	2.37
Mn_3Co_2	TBP	2.03	0.00	1.8	2.45
	TBP	2.01	0.10	1.8	2.45
	TBP	1.99	0.19	3.8	2.50
	TBP	1.99	0.22	3.4	2.44
	TBP	1.97	0.30	3.8	2.54
Mn_4Co	TBP	1.76	0.00	2.2	2.52
	TBP	1.76	0.02	0.2	2.49
	TBP	1.75	0.04	4.2	2.55
	TGPD	1.73	0.15	2.2	2.52
	SQPD	1.72	0.18	3.8	2.51
	TBP	1.71	0.25	4.2	2.60
	TBP	1.70	0.30	1.8	2.51
Mn_5	TBP	1.41	0.00	0.6	2.54
	TBP	1.40	0.06	2.6	2.58
	TBP	1.40	0.07	1.0	2.59
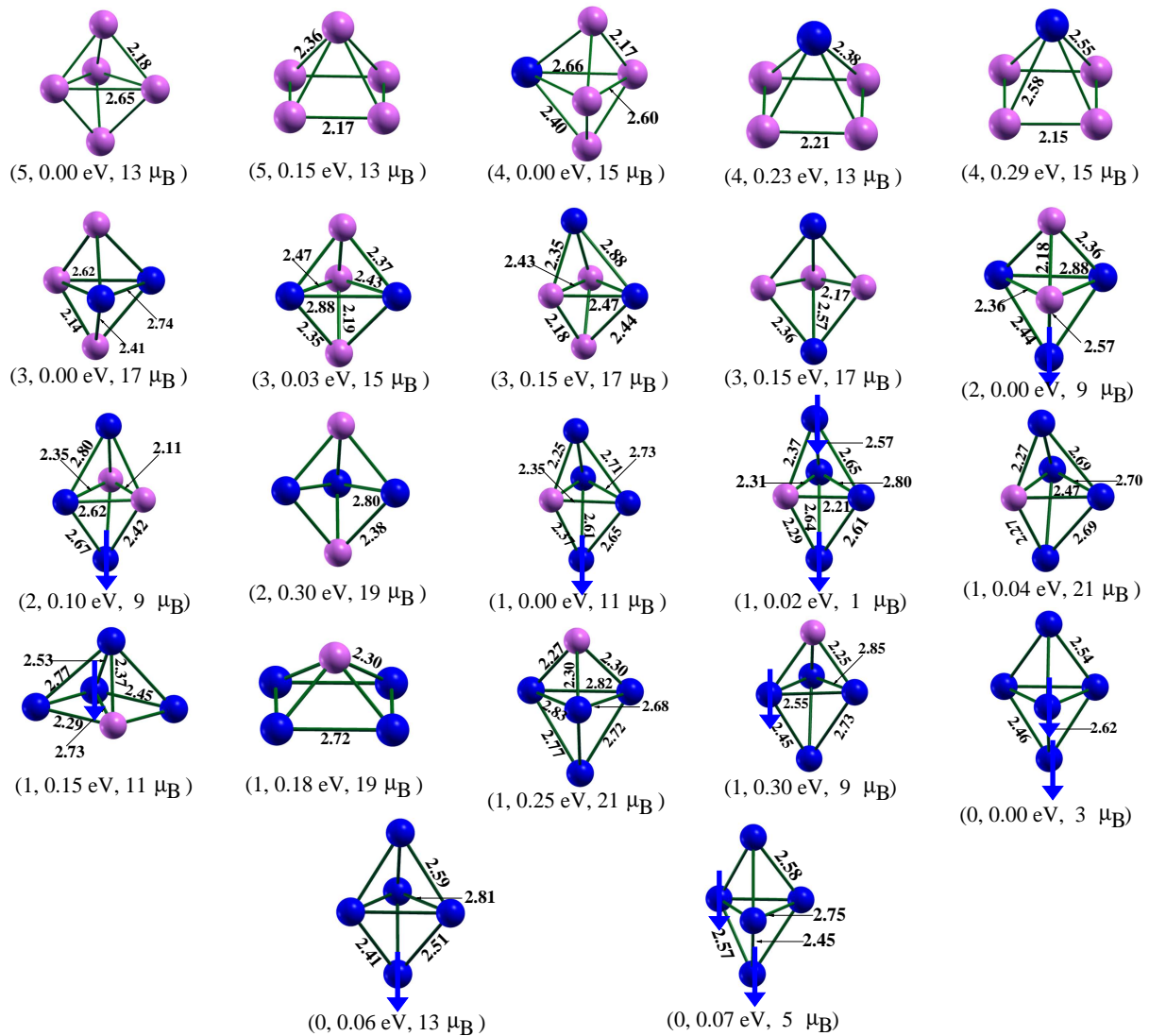
Figure 3.3: Ground state structures and significant isomers of Mn_xCo_y $(x+y=5)$ nano-alloy clusters. Same conventions are followed as in Fig.3.1.

The Fig.3.4 shows that, in general, the binding energy decreases with increasing number of Mn-atoms (x) for a particular sized cluster n. This again is due to the weaker binding among Mn atoms, and relatively weak Mn-Co binding than Co-Co bonding.

The stability S of these nano-alloy clusters with variation of Mn-concentration x can

be defined as,

$$S(n, x) = E(n, x + 1) + E(n, x - 1) - 2E(n, x), \quad (3.3)$$

where $E(n, x)$ is the bound state energy of the $Mn_x Co_y$ ($n = x + y$) cluster, and is shown in Fig.3.5 for $n = 5$. The $MnCo_4$ clusters is seen to have maximum stability. A sudden dip in stability is seen for $Mn_2 Co_3$, which can be described in terms of different bond distributions. We see that $Mn_2 Co_3$ has maximum (minimum) Mn-Mn (Co-Co) bond length, and thus, has the weakest (strongest) Mn-Mn (Co-Co) interaction among all the $n=5$ clusters with different compositions. This reduced hybridization of the Mn-atoms in turn reduces the stability of this cluster compared to its neighbors in x, and also leaves the cluster ferromagnetic. Similarly, for $n=4$ cluster, $Mn_2 Co_2$ has larger average Mn-Mn distance (2.83 A) than $Mn_3 Co$ (2.74 A) and found to be less stable.

3.3.3   Magnetic moment

The atoms in the pure Co_n clusters are found to be aligned ferro-magnetically [Datta *et.al.* 2007], whereas a ferromagnetic to ferri-magnetic transition has been observed for
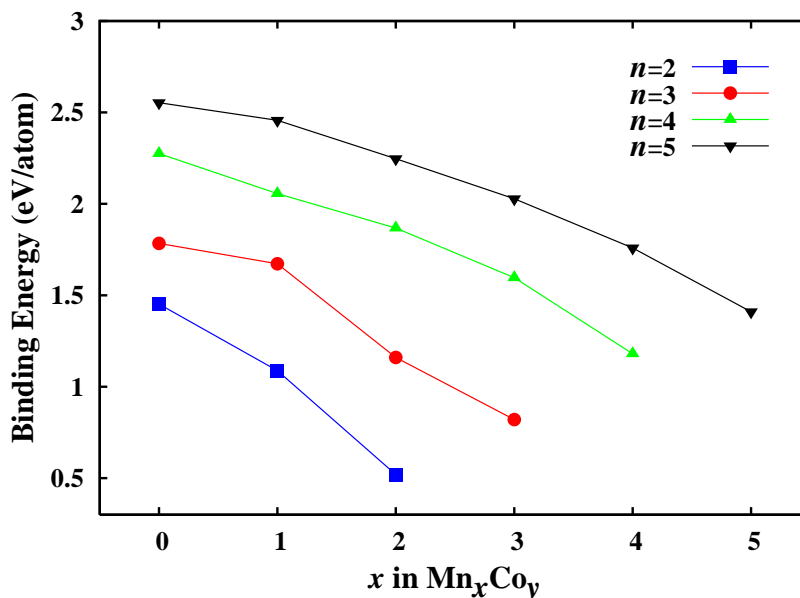
Figure 3.4: Binding energy of $Mn_x Co_y$ alloy clusters as a function of Mn-concentration.
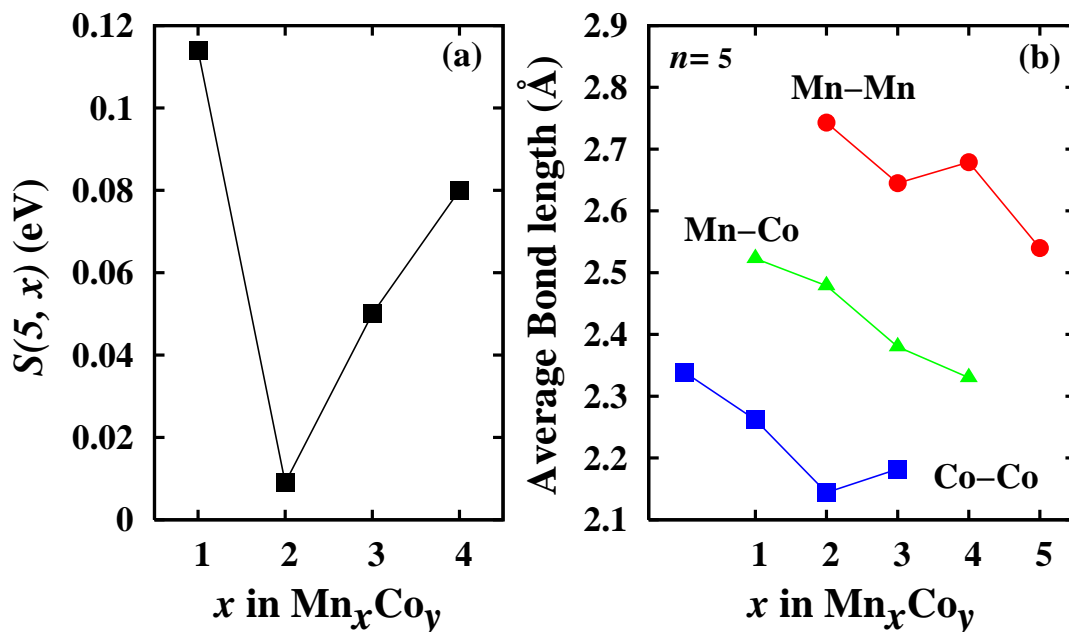
Figure 3.5: (a) Relative stability and (b) different (Mn-Mn, Mn-Co, and Co-Co) bond lengths of $n = 5$ cluster as a function of Mn-concentration.

pure Mn_n at $n = 5$ and remains the same for larger sized clusters [Kabir *et.al.* 2006]. The local magnetic moment of Mn (μ_{Mn}) is found to be higher than μ_{Co} due to more number of unpaired d-electrons in Mn-atom ($3d^5 4s^2$) than in Co-atom ($3d^7 4s^2$).

Fig.3.6 shows the average magnetic moment $\bar{\mu}$ as a function of Mn-concentration, x, for different cluster sizes n. For $n = 2$ and 4, $\bar{\mu}$ increases with increasing number of Mn-atoms. This is expected since for these sizes, all the clusters with different compositions are ferromagnetic. As mentioned earlier, the net number of unpaired d-electrons in Mn (five) is greater than that in Co (three). Thus as Co-atoms are replaced by Mn-atoms, total cluster moment increases by ~ 2 μ_B/Mn-substitution. For cluster size n=3 and composition x=2, and also for n=5 and $x \geq 3$, i.e., as the clusters become Mn-rich, $\bar{\mu}$ decreases with x. We see that these Mn-rich clusters are ferri-magnetic. For pure Mn_n clusters ferri-magnetic coupling is observed for $n \geq 5$ (Ref. [Kabir *et.al.* 2006]). On the other hand, for bimetallic $Mn_x Co_y$ clusters, ferri-magnetic coupling of Mn-atoms is observed for n=5 with $x \geq 3$. This could be because, for pure Mn_3 and Mn_4, the ferri-magnetic isomers having average magnetic moment 1.67 and 2.50 μ_B/atom, respectively,
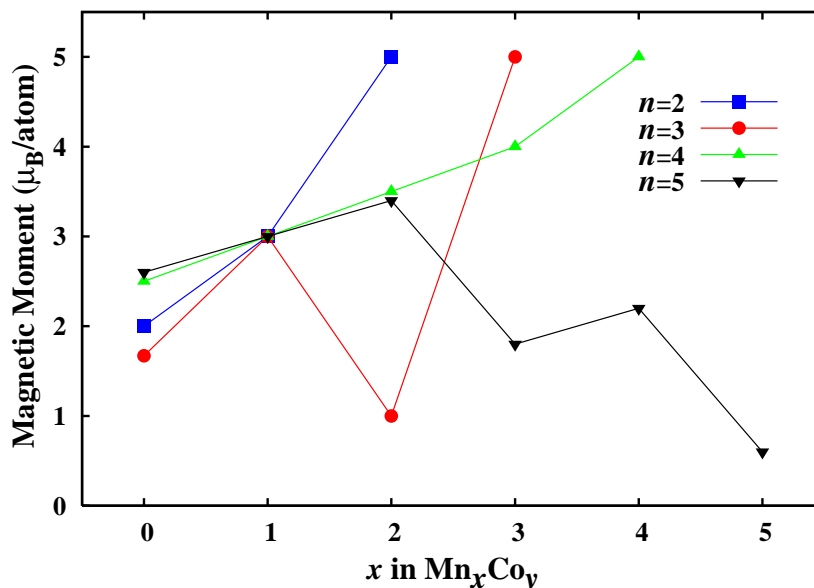
Figure 3.6: Calculated magnetic moment per atom as a function of Mn-concentration.

lie just 0.05 eV and 0.08 eV above their corresponding ferromagnetic ground states. Thus perturbing these clusters with Co-atoms could induce the corresponding ground state to be ferri-magnetic.

Another interesting observation is made that if we dope a Co_2 dimer with increasing number of Mn-atoms, the Co-Co bond length keeps increasing (Fig.3.7a). This indicates that Mn-atoms reduce the hybridization between Co-atoms in the dimer. Therefore, we have further studied the average μ_{Co} in Co_2 dimer with increasing x, and is shown in Fig.3.7b. It is seen that μ_{Co} remain almost the same for all the Mn_xCo_2 clusters (1.94, 1.88, 1.88, and 1.85 μ_B/atom for Co_2, $MnCo_2$, Mn_2Co_2, and Mn_3Co_2, respectively). Although the Co-Co bond length in Mn_xCo_2 increases with increasing x, the coordination of Co-atoms also increases as we go along $Co_2 \rightarrow MnCo_2 \rightarrow Mn_2Co_2 \rightarrow Mn_3Co_2$, which leaves the effective hybridization of the Co-atoms unaffected.

The magnetization density (difference between the up and down spin densities) further illustrates (Fig.3.8) the magnetic nature of these nano-alloy clusters. It is interesting to note that in ferri-magnetic Mn_2Co (Mn_4Co) cluster the $Mn_\uparrow$-$Mn_\downarrow$ separation is 2.64 A (2.61 and 2.65 A). This is significantly smaller than $Mn_\uparrow$-$Mn_\uparrow$ separation in ferromagnetic

Mn_3 and Mn_4 clusters, 2.74 and 2.70, respectively [Kabir *et.al.* 2006]. Also the average $Mn_\uparrow$-$Mn_\uparrow$ bond in ferri-magnetic Mn_4Co is longer (Fig.3.8c) than the $Mn_\uparrow$-$Mn_\downarrow$ one. Thus it seems that wherever there is a contraction of Mn-Mn bond due to Co doping, the two Mn atoms concerned get antiferro-magnetically aligned. This is further supported by the fact that for Mn_3Co, where the distances between the Mn atoms (2.74 A) is not reduced by Co-doping, the Mn atoms remain ferro-magnetically coupled. The dependence of Mn-Mn coupling on the separation is due to the modification of hybridization. We will further discuss the magnetic nature of the clusters in Section 3.3.8 through partial charge density.

3.3.4   Comparison of magnetic moment with Stern-Gerlach experiment

In a recent SG experiment, Mn_xCo_y (n=11-29) clusters were produced via pulsed laser vaporization from cylindrical Mn_xCo_{1-x} alloy ($Mn_{0.15}Co_{0.85}$ or $Mn_{0.5}Co_{0.5}$) target rods [Knickelbein 2007]. The *mass spectrum* shows that average Mn-fraction in the alloy clusters are always less than in the corresponding source rod. However, this Mn-fraction increases with the increase in cluster size. Therefore, in the experiment, alloy clusters were always Co-rich compared to the bulk source [Knickelbein 2007]. Clusters generated from both the $Mn_{0.15}Co_{0.85}$ and $Mn_{0.5}Co_{0.5}$ target rods have moments that are similar
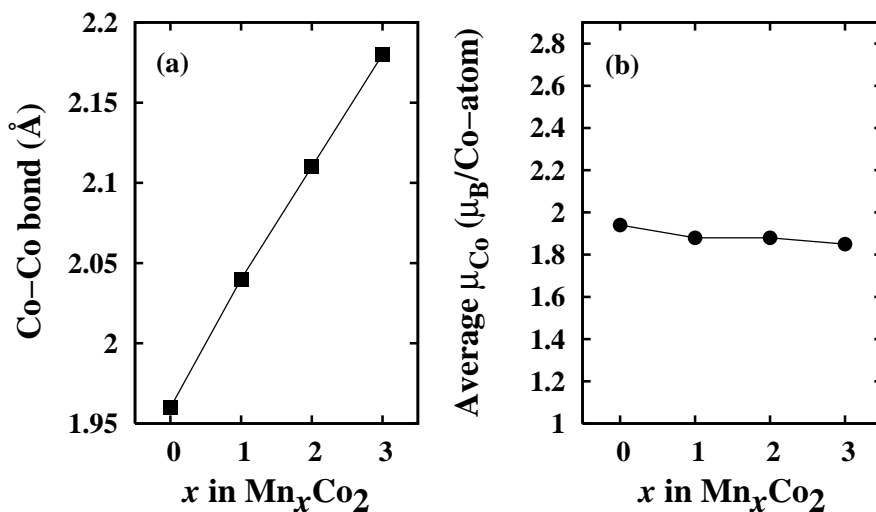
Figure 3.7: (a) Co-Co bond length and (b) average local Co-moment (μ_{Co}) in Mn_xCo_2 clusters as a function of x.
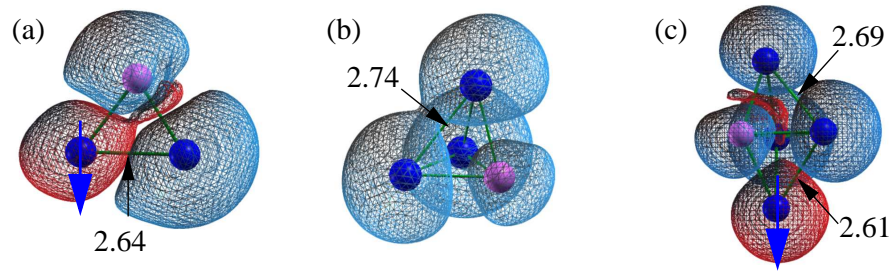
Figure 3.8: Isosurfaces of magnetization density for (a) Mn_2Co, (b) Mn_3Co, and (c) Mn_4Co corresponding to 0.02, 0.03, and 0.04 e/A^3, respectively. Dark (Blue) and light (magenta) color represent Mn- and Co-atoms, respectively. The $Mn_\downarrow$ is marked by down arrow. Blue (Red) surface indicates positive (negative) magnetization density.

to that of the pure cobalt clusters of same size. In fact in *smaller* size range, n=11-14, the average moment is enhanced by 28-60% for clusters generated from $Mn_{0.50}Co_{0.50}$ source. We have compared the magnetic moments of pure Co_n clusters with 50-50 Mn-Co nano-alloy clusters (Fig.3.9) in the size range n =2-5 to see whether the observed experimental trend continues for the smaller sizes. It should be pointed out here that, for
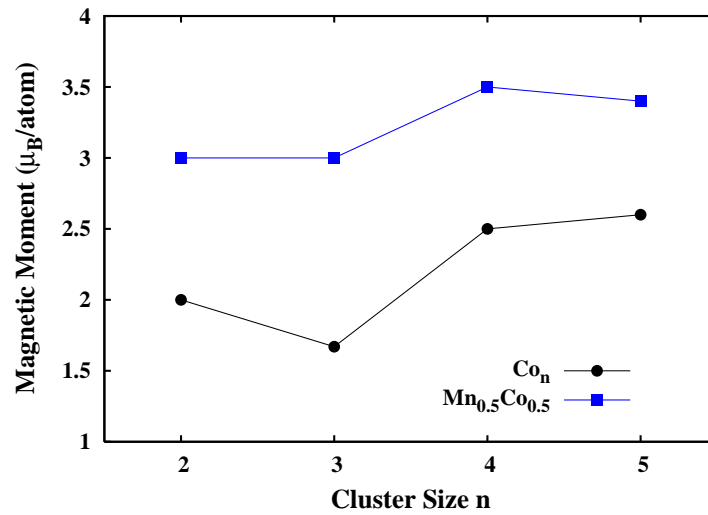
Figure 3.9: Magnetic moment of pure Co_n and $Mn_{0.5}Co_{0.5}$ clusters. For cluster sizes $n = 3$ and 5, the cobalt rich clusters ($MnCo_2$ and Mn_2Co_3, respectively) are considered. See the text.

$Mn_{0.50}Co_{0.50}$ clusters, we have considered the Co-rich clusters to mimic the experimental situation [Knickelbein 2007], for sizes where an exact 50-50 concentration is not possible. We see a 80-31% enhancement in magnetic moment compared to pure Co_n clusters. As we have already seen that these nano-alloy clusters are ferromagnetic unless the cluster is Mn-rich, thus when we replace Co-atoms in pure Co_n clusters with Mn, the magnetic moment increases.

In a separate SG experiment Yin *et al.* [Yin *et.al.* 2007] has found that magnetic moment increases as the number of Co-atoms, y, in Mn_xCo_y increases in the range 15-45 keeping x constant at $1 - 9$ (i.e., all the cluster are Co-rich). This observation also holds good in the present study for smaller clusters as long as the alloy cluster is Co-rich. For an example, as we go along MnCo ($6 \ \mu_B$) $\rightarrow$ $MnCo_2$ ($9 \ \mu_B$) $\rightarrow$ $MnCo_3$ ($12 \ \mu_B$) $\rightarrow$ $MnCo_4$ ($15 \ \mu_B$) the total moment increases with increasing y. They have also found that the total enhancement in the magnetic moment to be 1.7 μ_B/Mn-substitution, and is independent of the cluster size n and composition, which is justified by the virtual bond state model.Yin *et.al.* 2007 The present calculation is in good agreement and we find this enhancement to be 2 μ_B/Mn-substitution (Tables 3.1-3.4) as long as cluster is ferromagnetic (Co-rich).

3.3.5   Comparison with bulk alloy

The individual atomic moments of Mn and Co for Mn_xCo_{1-x} bulk alloy have been determined with increasing Mn:Co ratio through neutron scattering studiesKnickelbein 2007. On the Co-rich side μ_{Mn} and μ_{Co} are aligned antiferro-magnetically, with the magnitude of both μ_{Mn} and μ_{Co} decreasing monotonically with increasing Mn-content. Same trend is also seen for the mean per atom moment of the alloy $\bar{\mu} = x\mu_{Mn} + (1-x)\mu_{Co}$. However, it is seen from the SG experiments [Knickelbein 2007, Yin *et.al.* 2007] that Co-rich Mn_xCo_{1-x} nano-alloy clusters retain substantial magnetic moment in the size range n=11-29. Moreover, for clusters with n=11-14 obtained by laser vaporization of $Mn_{0.15}Co_{0.85}$ rods, the magnetic moment increases by 88-148% compared to the bulk value [Knickelbein 2007]. At 20% Mn-concentration for cluster size n=5 we estimate 241% enhancement in magnetic moment from the corresponding bulk value. This enhancement of $\bar{\mu}$ in low dimension over bulk alloy is not only due to decrease in coordination number, which effectively reduces
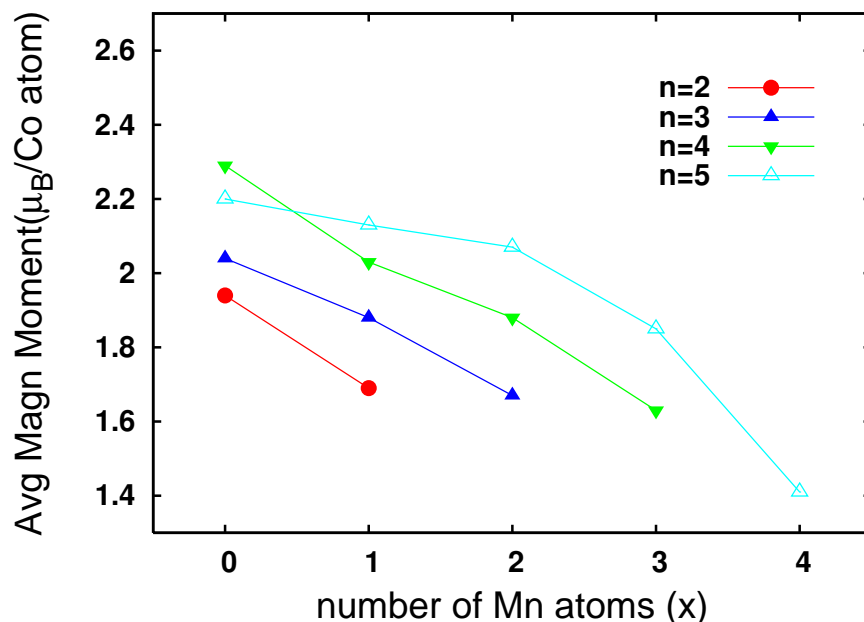
Figure 3.10: Average local Co-moment (μ_{Co}) as a function of Mn-concentration for different cluster sizes.

the hybridization among the orbitals, but also due to the ferromagnetic Mn-Co coupling (unlike bulk alloy) in Co-rich Mn_xCo_y nano-alloy clusters.

The average μ_{Mn} and μ_{Co} (calculated using Eqn. 2) are studied individually for different sizes with increasing Mn-concentration. The average μ_{Mn} oscillates with increasing x. For clusters like Mn_2Co which are ferri-magnetic, the average magnetic moment of Mn is very low ($0.08\mu_B$/atom), whereas for ferromagnetic (like Mn_2Co_2) clusters it is high ($4.21\mu_B$/atom). Here, it is to be noted that even for such ferri-magnetic clusters the individual μ_{Mn} values are high but due to their ferri-magnetic Mn-Mn alignment the net Mn-moment is low. The average μ_{Co} is plotted in Fig.3.10. It is clear from Fig.3.10 that, likewise in bulk alloy, the average μ_{Co} decreases with increasing Mn concentration for all cluster sizes, [3] and, as we will see in Section 3.3.7, is because of increasing Mn neighbor. However, μ_{Mn} doesn't behave in similar fashion, and unlike the bulk alloy, in Co-rich Mn_xCo_y nano-alloy clusters, μ_{Mn} and μ_{Co} are ferro-magnetically coupled.

---

[3]Degenerate ground states : It should be noted that the pure Co_3 has two degenerate ground states with 1.67 and 2.33 μ_B/atom.

3.3.6 A medium sized cluster ($n = 13$) and direct comparison with SG experiment

In order to perform a direct comparison with the SG experiment [Knickelbein 2007] we have studied a Mn_xCo_y cluster of size $n=13$, with 15% Mn-concentration i.e., Mn_2Co_{11} nano-alloy cluster. The ground state is found to be nearly degenerate with magnetic moments 1.92 and 2.38 μ_B/atom. The ground state has binding energy 3.18 eV/atom (Fig.3.11a), whereas the nearly degenerate isomer lies only 0.01 eV higher (Fig.3.11b). In the first structure the Mn-Mn distance is 2.46 A and one of the Mn-atom sits at the center, and consequently the magnetic moment of this (Mn) atom gets quenched. Whereas, the Mn-Mn distance is comparatively larger (4.78 A) in the second cluster as both the Mn-atoms sit on the surface. These are the reasons that the second structure has larger magnetic moment than the first one. Another icosahedral isomer (Fig.3.11c) has large magnetic moment of 2.69 μ_B/atom and lies 0.15 eV higher than the ground state.

The icosahedral ground state structure for this Mn-doped cluster is quite interesting. For pure Co_{13} the stable ground state is a distorted hexagonal structure [Datta *et.al.* 2007] and, on the other hand, we have previously found an icosahedral ground state for pure Mn_{13} cluster [Kabir *et.al.* 2006, Kabir *et.al.* 2007]. Replacing two Co-atoms in Co_{13} with Mn results in a structural change from a distorted-hexagonal-like structure to an icosahedron. The calculated magnetic moment of the pure Co_{13} is found to be 25 μ_B, which is in good agreement with experimental values, 26-30 μ_B (Refs. [Knickelbein 2006, Xu *et.al.* 2005]). On the other hand, two degenerate ground states of Mn_2Co_{11} nano-alloy cluster have 25-31 μ_B magnetic moments, which is 0-6 μ_B larger than that of (calculated) the pure Co_{13} cluster. This is in good agreement with the experiment: For $n=13$ cluster produced from $Mn_{0.15}Co_{0.85}$ bulk source an enhancement in average magnetic moment is seen over the corresponding pure Co_{13} cluster [Knickelbein 2006]. It should also be pointed out here that the SG experiment was done at finite temperature (91 K), so the cluster beam may contain both the degenerate states which are separated only by 0.01 eV energy.
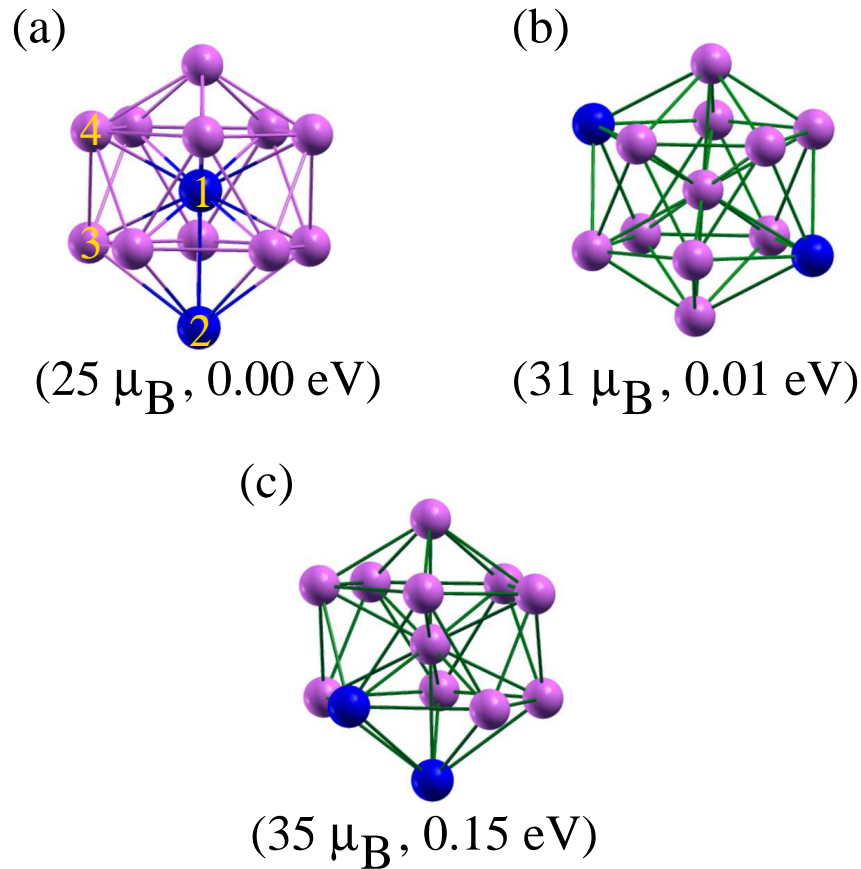
Figure 3.11: The ground state (a), first (b), and second (c) isomers for $Co_{11}Mn_2$ nano-alloy cluster. Same color conventions are used as in Fig.3.1. The numbers in the parenthesis represent the total moment and relative energy to the ground state, ΔE, respectively.

3.3.7 Projected density of states

To understand the decrease in average μ_{Co} when the environment is made more Mn-rich than Co (Fig.3.10), the integrated projected density of states (IPDOS) of the d-orbital has been investigated for the cobalt atoms in Mn_2Co_3 and Mn_4Co clusters. For the first cluster in the TBP ground state (Fig.3.3), the IPDOS of the Co-atom, which is co-planer with two Mn-atoms, is 4.41 for the majority spin channel, whereas it is 2.30 for the minority spin. For a off-plane Co-atom in same structure, the IPDOS is 4.30 for the majority spin channel and 2.40 for the minority spin one. The reason for this greater spin
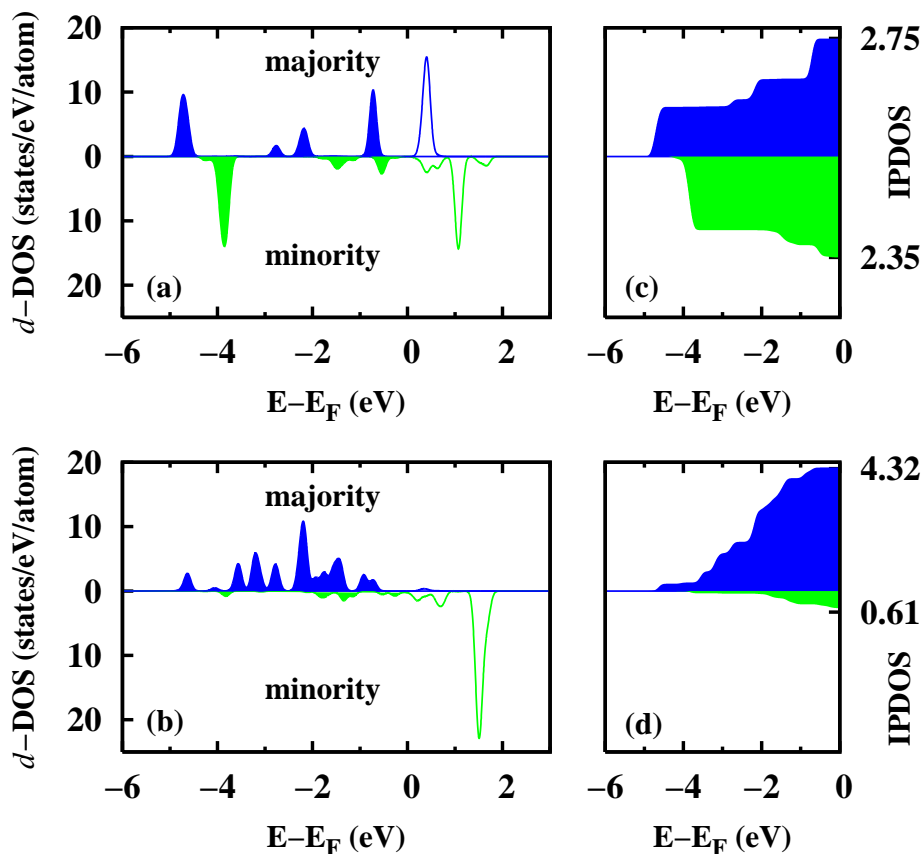
Figure 3.12: The d-projected density of states for the (a) central, and (b) surface Mn-atom of Mn_2Co_{11} cluster in its ground state (marked as 1, and 2, respectively, in Fig.3.11a). A Gaussian broadening of 0.1 eV has been used. Corresponding integrated density of states up to the Fermi level, E_F, are also shown for the (c) central, and (d) surface Mn-atoms.

polarization of the co-planar Co-atom is twofold. Firstly, the in-plane Co-atom has more (two) Co-atoms as its nearest neighbors than the off-planar ones (one). Secondly, the in-plane Mn-Co distance (2.62 A) is larger than that for the off-planar Mn-Co distance (2.41 A). Thus the effect of Mn-atoms felt by the in-plane Co-atom is less than that by the off-planar ones. This reinforces the observation that a Co-rich environment favors more spin polarization in Co than a Mn-rich environment. For the Co-atom in the second cluster, Mn_4Co, the IPDOS for the majority (minority) spin channel is 3.81 (2.50), giving rise to a decrease in spin polarization (compared to average d-polarization of Co-atoms in Mn_2Co_3), when the environment is made more Mn-rich at the cost of Co.

The d-projected density of states (d-DOS) and the corresponding IPDOS for Mn_2Co_{11} are also studied. These are shown in Fig.3.12 for the central, and apex Mn-atoms labeled as 1 and 2, respectively, in Fig.3.11a. We see that for the central Mn-atom (Fig.3.12a), the spin distribution in the majority and minority spin channels are nearly equal. Consequently, the magnitude of IPDOS (Fig.3.12c) for the majority and minority spin channels are close, 2.75 and 2.35, respectively. Thus for this central Mn-atom spin polarization is very low. On the other hand for the surface Mn-atom (Fig.3.12d), the majority spin channel is almost fully occupied (Fig.3.12b) and the magnitude of corresponding IPDOS for the majority and minority spin channels are 4.32 and 0.61, respectively. This gives a large spin polarization on this atom. This is because the surface Mn is less coordinated and hence has less hybridization than the central one. Further, the Co-atoms marked as 3 and 4 in Fig.3.11a have equal coordination number and the former has slightly larger (2.43 A) average bond length than the later one (2.38 A). Although we find that the Co-atom marked as 3 has slightly weaker spin polarization (1.74 μ_B) than that of marked as 4 (1.83 μ_B), as the former is bonded with one more Mn-atom than the later. This once again confirms our observation that μ_{Co} decreases with increasing Mn neighbors.

3.3.8   Partial charge densities

In order to take a deeper look into the electronic behavior responsible for anti-parallel alignment of one μ_{Mn} to other Co- and Mn-atoms in Mn_4Co, we have investigated the eigenvalue spectrum of the occupied levels. We find among the eight highest occupied levels (i.e., HOMO $- n'$ levels, where $n' = 0 - 7$), four of them are occupied by minority spins. On the other hand, among the eleven deepest occupied levels, six levels are occupied by minority electrons. Comparing this spin distribution picture with that of Mn_3Co, we see that for this ferromagnetic cluster also, only four of the eight highest occupied levels are occupied by minority spins likewise in the ferri-magnetic Mn_4Co. However, only one of the deepest eleven states are occupied with minority spin. Therefore, it seems that these deep valence levels play a major role in determining the magnetic structure of these two clusters.

We have further looked at the charge density distribution of the six minority spin

electrons in ferri-magnetic Mn_4Co nanocluster, which occupy these deepest molecular orbitals. At large isosurface values the charge densities are localized on the $Mn_\downarrow$ and are distributed mostly between this $Mn_\downarrow$ and the Co-atom for lower isosurface values (Fig.3.13). The shape of the charge densities indicates that these electrons are d-electrons. Thus, single Co-doping in ferromagnetic Mn_4 makes Mn_4Co ferri-magnetic. On the other hand, the charge densities of the majority electrons are spread out among the Co-atom and the three $Mn_\uparrow$-atoms at small isosurface values. Charge densities for two of these majority electrons are shown in Fig.3.14. The shape of these charge density isosurfaces also exhibits d-orbital character. It is interesting to observe that the $Mn_\downarrow$ is completely devoid of majority charge contribution for these deep valence levels. Thus it must be so that the $Mn_\downarrow$ goes from the $4s^2 3d^5$ to $4s^1 3d^6$ configuration in Mn_4Co. Due to Co doping the $Mn_\downarrow$-$Mn_\uparrow$ separation in the cluster is reduced, which consequently enhances the hybridization and cause the six d-electrons in this $Mn_\downarrow$ to belong to the minority spin channel.
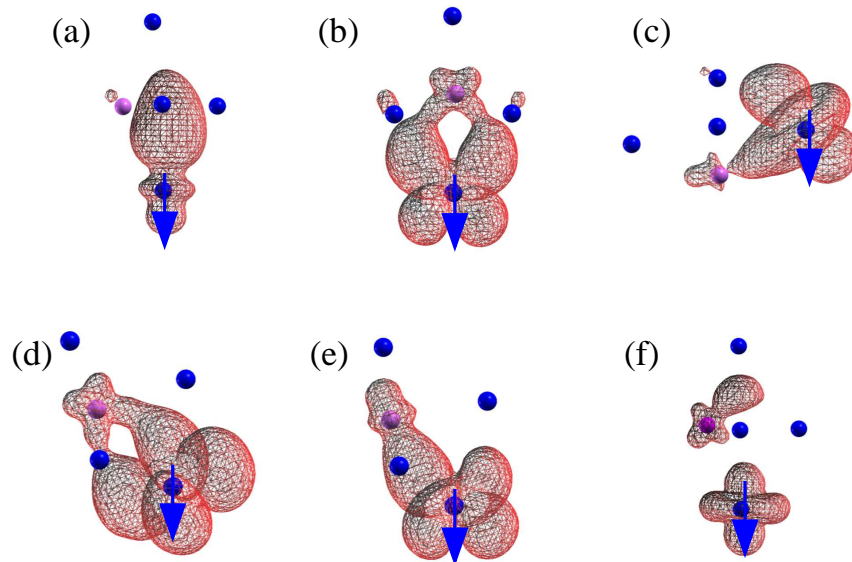
Figure 3.13: The charge density isosurfaces of the six down electrons in the deepest energy levels for Mn_4Co cluster. They are shown at (a) 0.04, (b) 0.01, (c) 0.01, (d) 0.01, (e) 0.01, and (f) 0.03 e/A^3, respectively. Blue and magenta color represent Mn- and Co-atoms, respectively, and the $Mn_\downarrow$ is marked by down arrow.
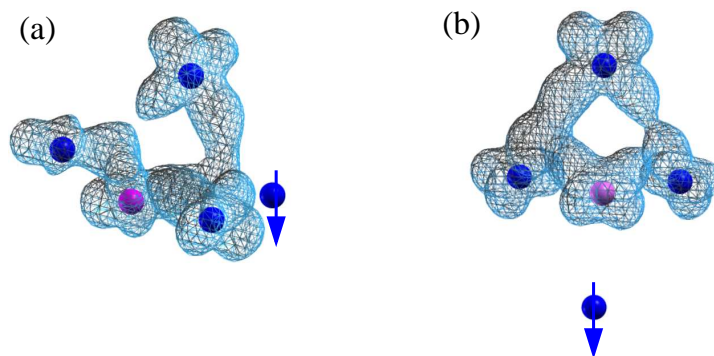
Figure 3.14: The charge density distribution for two of the majority electrons in the deep levels for Mn_4Co cluster. Blue and magenta color represent Mn- and Co-atoms, respectively, and the $Mn_\downarrow$ is marked by down arrow. The isosurfaces are drawn at 0.04 e/A^3 density.
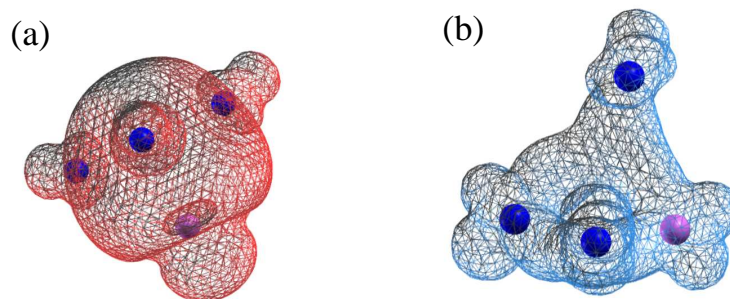
Figure 3.15: The charge density distribution for (a) the minority electron at 0.01 e/A^3 isodensity and (b) for one of the majority electrons at 0.03 e/A^3 isodensity in the deep levels of Mn_3Co cluster. Blue and magenta color represent Mn- and Co-atoms, respectively.

In contrast the charge density of the electrons occupying the deepest energy levels of Mn_3Co cluster exhibits quite a different picture. The charge densities of both the majority and minority electrons for small isosurface value (Fig.3.15) are spread out amongst all the four atoms in the cluster and not localized on any one of them.

3.4   Summary

We have studied structure, bonding, and magnetism in small bimetallic Mn_xCo_y ($x+y$=2-5) clusters from first-principles DFT calculation. Due to van der Waals like weaker bonding among Mn-atoms and relatively strong Co-Co bonding than Mn-Co bonding, the binding energies of the alloy clusters decrease with increasing Mn-concentration. Interesting effects in binding energy, stability and magnetism in the nanoalloy clusters are explained through the interplay between bond length and coordination. The Co-rich clusters are found to be ferromagnetic unlike the bulk alloy and the corresponding magnetic moment is higher than the pure Co_n clusters as is seen in the recent SG experiments. [Knickelbein 2007, Yin *et.al.* 2007] Moreover, the magnetic moment of Co-rich nano-alloy clusters increase with Mn-concentration and this increment is 2 μ_B/Mn-substitution and is independent of cluster size and composition. Co-atoms are found to be more magnetically polarized in a Co-rich environment than in Mn-rich one, i.e., likewise in bulk alloy, as the environment is made more Mn-rich, the average μ_{Co} decreases.

Chapter 4

A study of the electronic structure of MnO clusters

In this chapter[1] we observe an unusual evolution of structure and magnetism in stoichiometric MnO clusters based on an extensive and unbiased search through the potential-energy surface within the Density Functional Theory (which is discussed in details in an earlier chapter). The smaller clusters, containing up to five MnO units, adopt two-dimensional structures; and regardless of the size of the cluster, magnetic coupling is found to be anti-ferromagnetic in contrast to previous theoretical findings. Predicted structure and magnetism are strikingly different from the magnetic core of Mn-based molecular magnets, whereas, they were previously argued to be similar. Both these features are explained through inherent electronic structures of the clusters.

4.1   Introduction

Transition metal oxide nanoclusters have recently attracted extensive multidisciplinary research activities because of their diverse and tunable magnetic and catalytic properties. Manganese oxide nanoclusters are an important example [Sessoli *et.al.* 1993, Wernsdorfer *et.al.* 2002, Zouni *et.al.* 2001, Ferreira *et.al.* 2004, Brimblecombe *et.al.* 2010, Ruettinger 2000, Jiao and Frei 2010]. Generally, compared to bulk, the local magnetic moment is enhanced at smaller dimension due to a reduction in the number of neighboring atoms (coordination), and results in either an overall enhancement of the total moment for the ferromagnetic (FM) case or a finite moment even for the anti-ferromagnetic (AFM)

---

case due to unequal compensation of spin up and down electrons. Magnetic coupling also evolves with particle size, however, such size evolution for MnO nanoclusters is non-monotonic. MnO nanoclusters with a diameter of 5-10 nm show FM behavior [Li *et.al.* 1997, Lee *et.al.* 2002] even though their bulk phase is AFM [Ketelle 1949, Towler *et.al.* 1994]. In contrast, Mn-based single molecular magnets (magnetic core < 1.5 nm) show a 'layered' anti-ferromagnetic/ferri-magnetic structure within the mixed-valent Mn centers, resulting in a large magnetic moment and spin anisotropy [Sessoli *et.al.* 1993, Wernsdorfer *et.al.* 2002]. In this respect $Mn_{12}O_{12}$ derivatives are very popular as single-molecule magnets(SMM) [Boskovic *et.al.* 2000, Heersche *et.al.* 2006]. This is because these possess a large spin(S=10) and a very large energy barrier to relaxation of their magnetization direction. Recently Mn_8O_8 cluster derivatives has been found to act as SMM with the highest yet known spin(S=16) for a Mn species [Tasi *et.al.* 2003].But the magnetic state of small $(MnO)_x$ clusters (x=1 to 9) still remain a matter of debate. While some theoretical studies claim these clusters to be ferromagnetic [Nayak and Jena 1998, Nayak and Jena 1999, Pederson and Khanna 1999] others have found them to be anti-ferromagnetic like bulk [Han *et.al.* 2005, Wang *et.al.* 2010]. Since experiments on such clusters are not available in literature thus the only way to resolve this controversy regarding magnetic state of small MnO cluster is through a very systematic and rigorous theoretical study. It has become essential to determine the ground state of these oxide clusters correctly because with the advent of great development in the synthetic methodology for mass production of magnetic oxide nanoparticles and their shape and size control [Hyeon] a theoretical understanding of their structural, magnetic and electronic properties have become essential. Moreover depending upon whether the small $(MnO)_x$ clusters are ferro or anti-ferromagnetic there is a drastic transition of the magnetic state of Mn_n clusters with oxygen addition either above or below n=5. This is because pure Mn_n clusters are ferromagnetic for $n < 5$ and ferri-magnetic in the size range $n = 5 - 20$ [Kabir *et.al.* 2006]. This ability to chemically tune the magnetic property of transition metal clusters can prove to be of potential technological importance in ultrahigh-density storage devices [Zarur and Ying 2000]. Moreover, the MnO nanoclusters take essential part in a variety of biological (catalytic) processes from photosynthesis to bacterially mediated organic matter decomposition. One of the most crucial processes for life on earth is photosynthesis which

converts solar energy into chemical energy. Light initiates a series of electron-transfer reactions which are carried out in the oxygen-evolving center(OEC) of the photosystem. The active inorganic center of the oxygen evolving photosystem II contains a manganese oxide cluster (Mn_4O_4Ca), which catalyzes the light-driven oxidation of water [Zouni *et.al.* 2001, Ferreira *et.al.* 2004, Brimblecombe *et.al.* 2010]. Indeed, synthetic complexes containing cuboidal Mn_4O_4 core have been found to exhibit unique reactivity in water oxidation/O_2 evolution   [Ruettinger 2000].

The first step to the study of cluster properties is the determination of the ground state structures. But there remains controversy in the ground state structures of small $(MnO)_x$ clusters. While some theoretical studies claim the structures to be fragments of the bulk cubic structure [Nayak and Jena 1998, Nayak and Jena 1999, Han *et.al.* 2005, Pederson and Khanna 1999] an experimental study done through mass spectrometry [Ziemann and Castleman 1992] suggests the clusters $(Mn_3O_3)_n$ (n is an integer)to have a structure formed by stacking of Mn_3O_3 structure. They have shown Mn_3O_3 cluster to be a "magic cluster" with exceptionally high stability. A theoretical study using an alternative approach to DFT, namely, Quantum Monte Carlo also does a careful study of geometric structure [Kino *et.al.* 2009] and finds them to differ from that of Jena *et al.* But unfortunately this study mainly scans the higher moment magnetic states only. So, it does not give a complete picture of the ground state of the clusters. The electronic and magnetic properties of clusters depend critically on their structure. So an extremely careful search of ground state structure is the key to determination of magnetic properties of clusters conclusively. Starting with an arbitrary geometric structure and performing molecular dynamics simulation with it we first generate several probable initial geometries which we force-optimize in order to avoid landing up in some local minima. This is computationally expensive task but extremely efficient in correctly determining the ground state structure. We first study $(MnO)_x$ clusters with x=1-8 using this technique. Mn_8O_8 cluster has been studied since there is a claim of it showing magnetic bistability by studies which has claimed it structure to be a fragment of the bulk. [Nayak and Jena 1998, Nayak and Jena 1999]. Our technique allows us to even investigate clusters like $(MnO)_5$ whose structure can not be made to have the symmetry of the bulk and thus could not be investigated by earlier studies.

Our stability analysis shows Mn_3O_3 cluster to indeed have high stability and $(Mn_3O_3)_2$ cluster to have the Mn_3O_3 structure as its unit. Mn_4O_4 cluster is also very stable and thus $(Mn_4O_4)_2$ cluster has Mn_4O_4 cluster as its unit. The clusters are all anti-ferromagnetic like bulk. Indeed, in contrast to the previous theoretical reports, in this study we report through a rigorous PES search that the $(MnO)_x$ clusters show AFM coupling and also show unusual two-dimensional (2D) structures up to a certain size. Thus there is a transition of magnetic state of Mn_n clusters with n=2,3 and 4 from ferromagnetic to anti-ferromagnetic upon oxygen addition(transition from ferri-magnetic to anti-ferromagnetic occurs for n=5 and above). There is also a structural transition of Mn_n clusters, n=4 and 5 from 3D to 2D upon oxygenation.

4.2   Computational Details

Like the study of MnCo clusters as discussed in the previous chapter, for MnO clusters as well calculations are performed using DFT based pseudo-potential plane wave method. [Kresse *et.al.* 1999] Here too we have chosen the projector augmented wave method, [Blöchl 1994] and used the Perdew-Bruke-Ernzerhof exchange-correlation functional [Perdew *et.al.* 1996] for the spin-polarized generalized gradient correction. The $3d$ and $4s$ electrons of Mn and $2s$ and $2p$ electrons of O are treated as valence electrons. The wave functions are again expanded in a plane wave basis set within 270 eV kinetic energy and reciprocal space integrations are carried out at the Γ point. For each x for $(MnO)_x$ (x=1-8) we have chosen our initial geometric structures through first-principles (spin-polarized) Born-Oppenheimer molecular dynamics simulation. The ionic phase space of the cluster is sampled classically in a canonical ensemble using the method proposed by Nosé [Nosé 1984]. Starting from a high symmetry structure, for example a cubic structure (core of the Mn_{12}-molecular magnet [Sessoli *et.al.* 1993]) for the $(MnO)_4$ cluster initial geometry we have heated our cluster up to 2000k (above the melting temperature of bulk MnO) and performed Born-Oppenheimer molecular dynamics (BOMD) simulations for 6 - 10 psec. The clusters evolve through various geometric structures through this process. We have chosen different initial geometries by closely observing this evolution. We have also considered all possible spin multiplicities for each of these structures.Then symmetry

unrestricted optimizations (of both geometry and spin) are performed using the conjugate gradient and quasi-Newtonian methods until all the force components are less than a threshold value of 0.005 eV/$\underline{r}A$. This ensures the robustness of the ground state search. It should be mentioned here that calculations are done within the collinear spin assumption.

The binding energy per MnO unit (E_B) is defined as,

$$E_B[(MnO)_x] = [E(Mn) + E(O) - \frac{E[(MnO)_x]}{x}],$$ (4.1)

where x is the number of MnO units in our cluster, $E[(MnO)_x]$, $E(Mn)$, and $E(O)$ are the total energies of $(MnO)_x$ cluster, and an isolated Mn- and O-atom, respectively. For a given x , the structure with the highest binding energy is considered to be the *ground state*.

4.3   Results and Discussions

Although the magnetic structure is strongly coupled with the cluster geometry, we first discuss the geometric evolution alone. As expected for the MnO dimer, the Mn-O distance is much smaller (1.65 A) than bulk, in agreement with experimental [Merer 1989] and diffusion Quantum Monte Carlo (DMC) results [Wagner and Mithas]. Calculated Mn-O stretching frequency (920 cm^{-1}) is slightly higher than the experimentally assigned values (832 cm^{-1} Ref. [Merer 1989] and 899 cm^{-1} Ref. [Hocking *et.al.* 1980]) in the gas phase. The average Mn-O distances increase with cluster size, and the lowest energy structures are shown in Fig. 4.1. Interestingly, the presence of oxygen alters the geometry of MnO nanocluster (compared to pure Mn clusters [Kabir *et.al.* 2006]), and we find that clusters containing five MnO units pose two-dimensional (2D) structures (Fig. 4.1), where the lowest-lying 3D structures are separated by a large energy gap (Fig. 4.2(a)). The energy separation ΔE_{2D-3D} is 1.28 and 1.11 eV (equivalent to internal vibrational temperatures of 1650 and 1075 K) for $(MnO)_4$ and $(MnO)_5$ clusters, respectively. However, the scenario is reversed from the $(MnO)_6$ cluster (Fig. 4.1), whose energy gap is 0.61 eV (472 K). However, the present findings contradict the previous theoretical reports, where the PES search were highly biased [Nayak and Jena 1998, Nayak and Jena 1999, Pederson and Khanna 1999]. In contrast, DMC calculations *biased with only FM coupling* predicts a
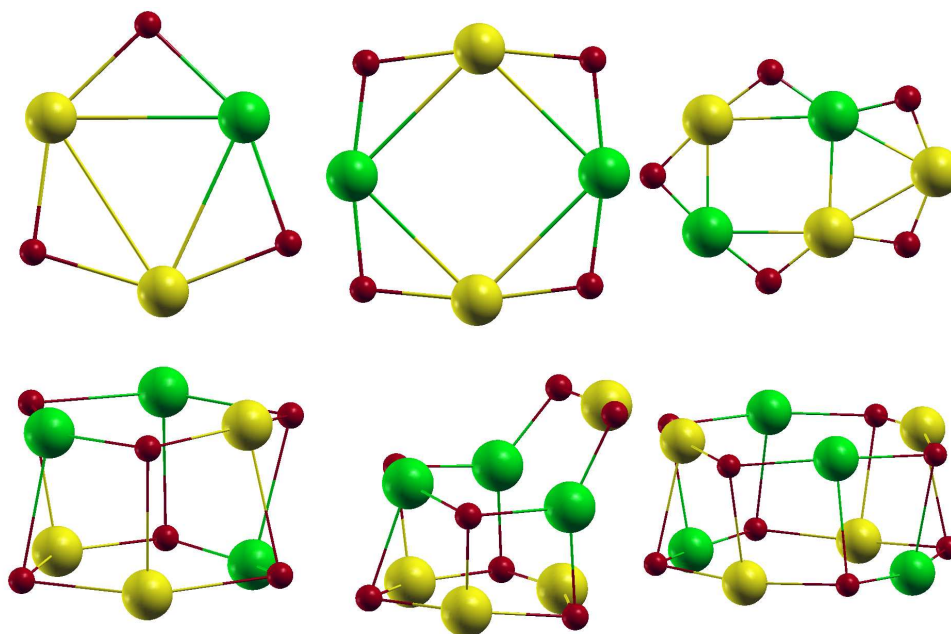
Figure 4.1: 2D to 3D transition takes place at $(MnO)_6$. Minimum energy structures are always found to be anti-ferromagnetic. The up (down) Mn-atoms are shown with yellow (green) color. Oxygen atoms are shown in red. For large clusters Mn-Mn bonds are not shown for clarity. The Mn-O (1.80 - 2.18 A) and Mn-Mn (2.55 - 3.10 A) distances, and the Mn-O-Mn angles (78°-108°) in these clusters are comparable to the molecular magnets [Sessoli *et.al.* 1993, Wernsdorfer *et.al.* 2002].

similar structural trend for $x \leq 4$ [Kino *et.al.* 2009]. However, present results are in accordance with the prediction of mass spectra [Ziemann and Castleman 1992], where Ziemann and Castleman proposed non-cubic structural growth, and larger clusters are composed of relatively more stable hexagonal $(MnO)_3$ and rhombic $(MnO)_2$ units. Similarly, we find that the $(MnO)_3$ cluster is more stable (magic cluster) and serves as the building block for larger cluster. It was believed earlier that the small MnO nanoclusters serve as the magnetic core of Mn-based single molecular magnets [Pederson and Khanna 1999]; the present study confirms that there is no such structural resemblance in terms of symmetry. The planar structure of $(MnO)_4$ (Fig. 4.1) is substantially different from the magnetic core of $[Mn_4O_3Cl_4(O_2CEt)_3(py)_3]_2$ [Sessoli *et.al.* 1993], $[Mn_{12}O_{12}(CH_3COO)_{16}(H_2O)_4]$ [Wernsdorfer *et.al.* 2002] molecular magnets and the oxygen evolving center (Mn_4O_4Ca) in pho-
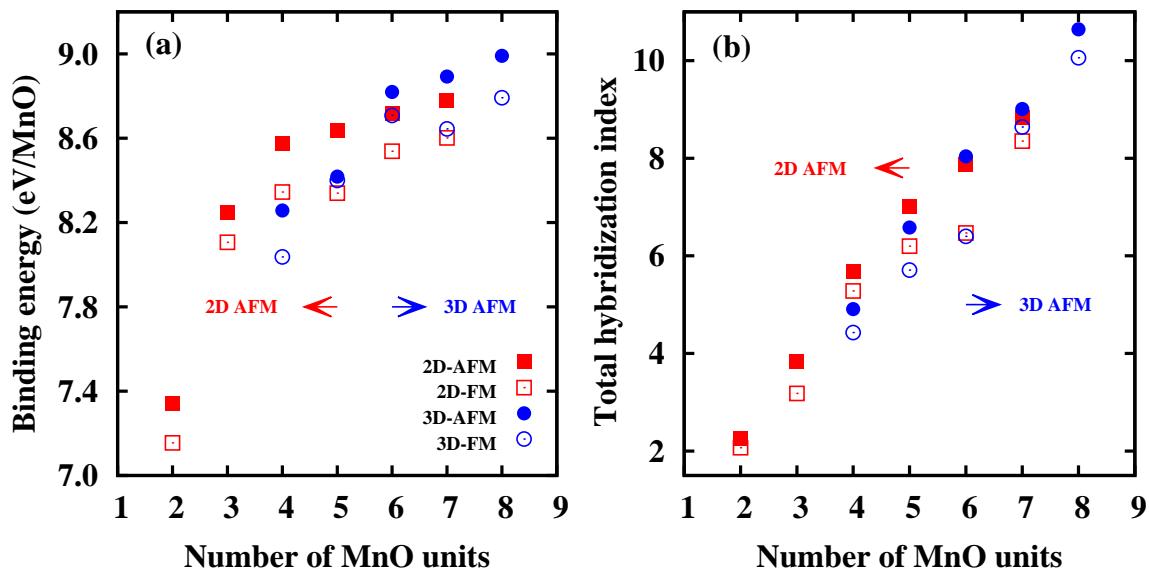
Figure 4.2: (a) The trend in binding energy shows that the nanoclusters adopt 2D structures until they contain five MnO units, above which they are 3D. The Mn-Mn magnetic coupling is always anti-ferromagnetic for the most stable solution. Moreover, the AFM coupling is always favorable over the FM coupling, in both 2D and 3D. (b) Total hybridization index, $\mathcal{H} = \mathcal{H}_{sp} + \mathcal{H}_{pd} + \mathcal{H}_{sd}$, shows a direct correspondence to the energy.

tosystem II [Zouni *et.al.* 2001]. The structural symmetry of $(MnO)_6$ is much different than that observed in an octahedral $[Mn_6(\mu_6\text{-}O)(\mu\text{-}OR)_{12}]$ molecular complex [Stamatatos *et.al.* 2009]. However, the structural parameters such as Mn-O (1.80-2.18 A), Mn-Mn (2.55-3.10 A) bond lengths, and Mn-O-Mn angles (78°-108°) in these clusters are similar compared to the molecular magnets (1.85-2.23 A, 2.77-3.44 A, and 94°-137°, respectively) [Sessoli *et.al.* 1993, Wernsdorfer *et.al.* 2002]. It should also be noted that the Mn-O distance in these nanoclusters already approached that of bulk MnO (2.25 A).

The binding increases substantially due to the presence of oxygen (Fig. 4.2), which can be explained in terms of the electronic configurations. The free Mn atom has $3d^5 4s^2$ configuration, and thus the Mn-dimer is weakly bonded [Kabir *et.al.* 2006]. In contrast, Bader charge analysis [Bader 1990, Henkelman *et.al.* 2006] shows that Mn atoms lose $1.20e$ charge to O for $(MnO)_2$, which makes binding in these clusters stronger. This amount ($\sim 1.20e$) of charge transfer remains the rule of thumb for all the minimum energy structures for the stoichiometric MnO clusters. In addition to the covalent Mn-O bonding,

this significant charge transfer suggests an ionic contribution to the bonding.

Calculated stability [$\Delta E_x = E(\text{MnO})_{x-1} + E(\text{MnO})_{x+1} - 2E(\text{MnO})_x$, where E is the total binding energy] is positive and shows a local peak for clusters with $x = 3$, 4 and 6, in agreement with experiments [Ziemann and Castleman 1992], shows exceptional stability referring to their magic nature. Clusters with three and four MnO units serve as the building blocks for larger clusters. Two $(\text{MnO})_3$ cluster units are stacked in 3D for the ground state (Fig. 4.1), when the similar staking in 2D (with similar AFM magnetic ordering) is 0.61 eV higher in energy (Fig. 4.2(a)). Similarly, as shown in Fig. 4.1, a $(\text{MnO})_3$ unit is stacked in 3D with a distorted $(\text{MnO})_4$ to form the most stable $(\text{MnO})_7$; whereas the $(\text{MnO})_8$ nanocluster is build with two $(\text{MnO})_4$ units.

To understand this morphological transition, we plot the orbital projected density of states (DOS) for the clusters (Fig. 4.3), which shows a clear trend: The energy spread of the orbitals is higher for the minimum energy structure and also has a larger orbital overlap. For example, a $(\text{MnO})_4$ nanocluster has larger orbital spread and also has higher *s-d* and *p-d* hybridization in 2D compared to the respective optimal 3D structure. In contrast, the situation is reversed for $(\text{MnO})_6$ cluster, where the larger spread and higher *s-d* and *p-d* hybridization makes 3D structure more favorable over the 2D one. The orbital hybridization can be quantified, and could explain the cluster morphology, which was applied earlier to explain the 2D nature of the gold clusters by Häkkinen *et al.* [Häkkinen *et.al.*]. We calculate the (*k-l*) hybridization index,

$$\mathcal{H}_{kl} = \sum_I \sum_i w_{ik}^I w_{il}^I, \tag{4.2}$$

where k, l are the orbital indices, $w_{ik}^I (w_{il}^I)$ is the square projection of the i-th Kohn-Sham orbital on to the k (l) spherical harmonics centered at atom I and integrated over a sphere (radius depends on the atom type, Mn/O. For a heterogeneous system, choice of the integrating radius is not unique. However, a choice of $R_{Mn} = (\langle d_{Mn-Mn}\rangle)/2$ and $R_O = 0.66\ r_A$ (the covalent radius of oxygen; B.Cordero *et al* , Dalton Trans. 2832 (2008) captures ~80% of the electrons.). Note that the spin index is inherent. However, unlike gold clusters, in a system with active *p*(O) electrons, in addition to the *s-d* hybridization index ($\mathcal{H}_{sd}$), the $\mathcal{H}_{pd}$ and $\mathcal{H}_{sp}$ would also play an important role for determining the dimensionality. Indeed, we find (Fig. 4.2(b)) that the total hybridization index $\mathcal{H}$ is
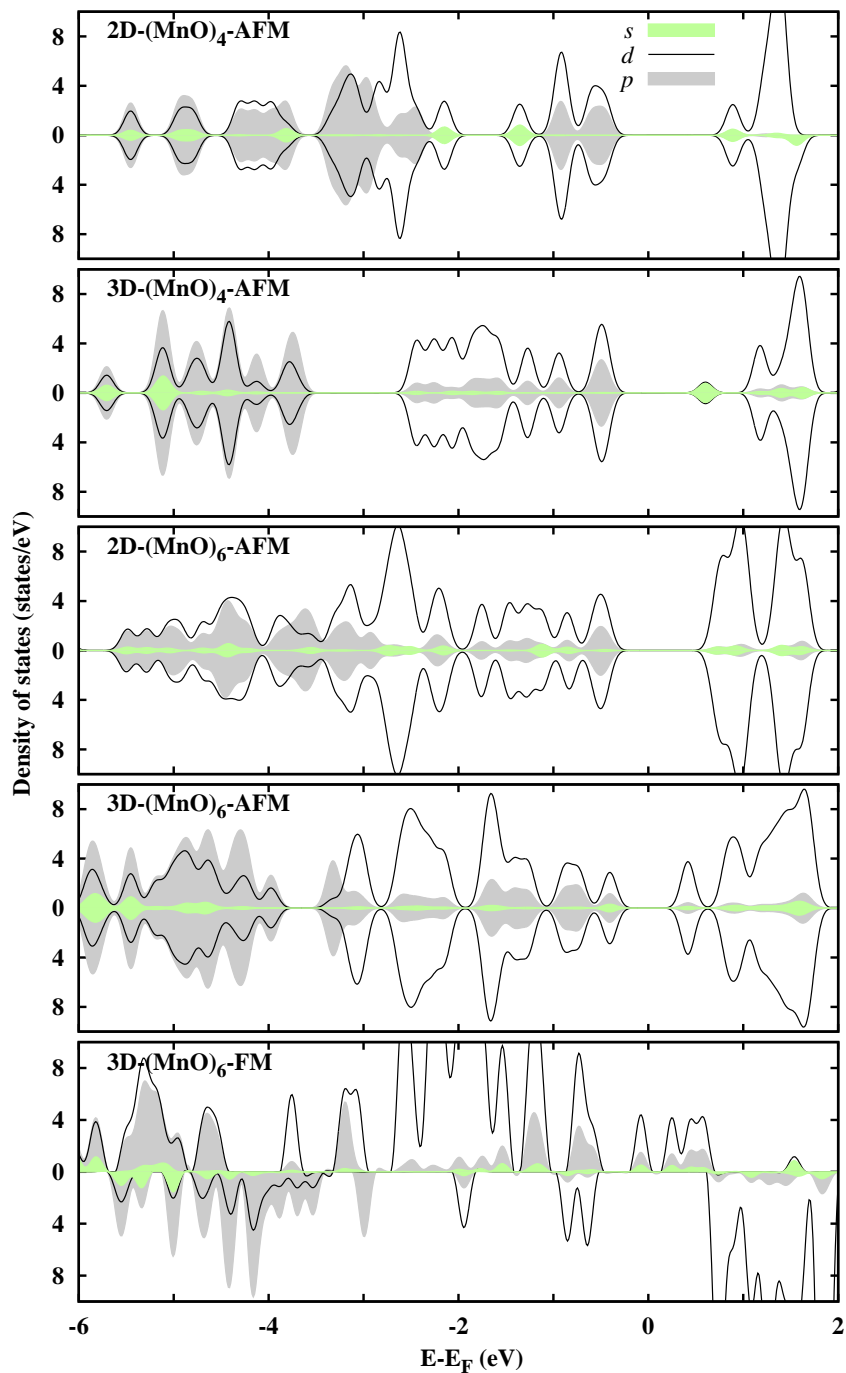
Figure 4.3: Orbital projected density of states summed over all the atoms in the nanocluster (for 2D and 3D $(MnO)_4$ and $(MnO)_6$ clusters in their AFM state; FM state for 3D $(MnO)_6$ is also shown) show that the minimum energy structures (both geometric and magnetic; 2D-AFM for $(MnO)_4$ and 3D-AFM for $(MnO)_6$) correspond to larger energy spread of the orbitals and higher hybridization. Gaussian smearing (0.1 eV) has been used.

always higher for the lowest energy structures for the entire size range.

Now we turn our attention to the magnetic structure, where we find that the Mn-atoms in all the nanoclusters are coupled antiferro-magnetically. This gives rise to a net 0 or 5 μ_B moment for the clusters with even and odd number of MnO units, respectively. It is also interesting to note here that regardless of their dimensional nature, the AFM arrangement is always energetically favorable (Fig. 4.2(a)). Although the experimental evidence of magnetic structure in such nanoclusters are scarce, the calculated results for the MnO dimer (sextet) is in agreement with the only available experiment [Merer 1989]. Although the moment is localized on the Mn-site, a small p polarization (0.02-0.15 μ_B) is observed for the oxygen atoms in the clusters. These results of the magnetic structure are in direct contradiction with the previous results including the DMC calculations [Nayak and Jena 1998, Nayak and Jena 1999, Pederson and Khanna 1999, Kino *et.al.* 2009], as all the previous studies were highly biased and only scanned a small subspace of the PES constrained either by geometrical structure with high symmetry or by FM coupling, or constrained by both. In contrast, the present approach does not employ any such *a priori* constrains. The presence of oxygen stabilizes the Mn-Mn AFM coupling. For example, the energy difference $\Delta E(\mathrm{FM} - \mathrm{AFM})$ is only -0.2 and 0.14 eV for pure $\mathrm{Mn_4}$ and $\mathrm{Mn_6}$ clusters, respectively [Kabir *et.al.* 2006], whereas this difference substantially increases to 0.92 and 0.67 eV, respectively for the $(\mathrm{MnO})_4$ and $(\mathrm{MnO})_6$ nanoclusters. It would be interesting to compare the magnetic structure of these nanoclusters with the $[\mathrm{Mn_{12}O_{12}(CH_3COO)_{16}(H_2O)_4}]$ molecular magnet [Wernsdorfer *et.al.* 2002]. The Mn atoms in the inner shell (four $\mathrm{Mn^{4+}}$) and in the outer shell (eight $\mathrm{Mn^{3+}}$) are FM coupled within both of the shells, but are AFM coupled between the shells, which is strikingly different from the nanoclusters.

Similar to the morphological stability, the magnetic stability can also be explained in terms of the total hybridization index and projected density of states. Compared to the FM structure, the AFM structure has larger orbital spread, and also accompanied by higher hybridization index. For example, the 3D-FM structure for $(\mathrm{MnO})_6$ has sharp d-states (Fig. 4.3), and in contrast, the d-states are more wide spread in energy and show larger overlap with $p(\mathrm{O})$-states. Calculated total hybridization index $\mathcal{H}$, as shown in Fig. 4.2(b), is much higher in the AFM state (8.04) than in the FM state (6.40) in 3D,

confirming the preference of AFM coupling.

Compared to AFM bulk MnO crystal [Shull and Smart 1949, Towler *et.al.* 1994], the overall exchange mechanism is complicated in MnO nanoclusters; the semi-empirical Goodenough-Kanamori rules can be employed to understand the Mn-Mn magnetic coupling. In addition to the Mn-O-Mn superexchange mechanism, direct Mn-Mn exchange mechanism is also present in these clusters as the Mn-O-Mn angle is much smaller than 180° (Fig. 4.1). As we have discussed earlier that pure Mn_4 is FM with $\Delta E(\text{FM} - \text{AFM})$ = -0.2 eV, i.e., the direct exchange prefers FM coupling. When O atoms are introduced, the magnetic structure changes to the AFM due to the stronger anti-ferromagnetic superexchange. In contrast, the direct exchange in pure Mn_6 is already AFM, and is further stabilized due to the AFM superexchange when O is introduced. Similar to the ferrimagnetic Fe_4O_6 clusters [Kirilyuk *et.al.* 2010], these stoichiometric MnO clusters also have a very large magnetic exchange (at least 0.11 eV per MnO unit), which is much larger than the Mn-based molecular magnets [Sessoli *et.al.* 1993, Wernsdorfer *et.al.* 2002]. Therefore, the Curie temperature of these $(MnO)_x$ clusters would be much higher than the corresponding AFM bulk MnO ($\sim$ 118 K), which can be exploited to tailor new materials.

4.4 Summary

In summary, we have demonstrated, through a rigorous and unbiased potential energy search, that the stoichiometric MnO nanoclusters show unusual 2D structures, and that Mn atoms are AFM coupled, and both the features are explained in terms of the inherent electronic structure of these nanoclusters. Present results deviate from the earlier theoretical predictions as the previous studies explored only a subspace of the potential energy surface limited by the high symmetry structure and ferromagnetic coupling [Nayak and Jena 1998, Nayak and Jena 1999, Pederson and Khanna 1999, Kino *et.al.* 2009]. Although the experimental results on such clusters are scarce, the present results agree well with the limited experimental predictions on the cluster structure and stability [Ziemann and Castleman 1992]. However, there is no experimental evidence on the evolution of magnetic structure; we believe the complementary infrared dissociation spectroscopy [Kirilyuk *et.al.* 2010] will be helpful to unambiguously determine the geometric

and magnetic structures of such transition metal oxide clusters in the gas phase.

Chapter 5

Electronic structure calculation in random binary alloys : Introduction to the Recursion and Augmented Space methods.

In this chapter we shall discuss the recursion technique introduced by Haydock as a very efficient method to calculate electronic structure properties of even those systems which lack lattice translational symmetry. Along with this we shall also introduce and discuss the Augmented Space Formalism which is a very useful technique for disorder averaging in random systems. These together form the Augmented Space Recursion technique, a method which we have used extensively to calculate various properties of model and real disordered systems in the subsequent chapters.

5.1 The Recursion Technique.

Bloch's theorem [Ashcroft and Mermin 1976] has rigid requirements of lattice translational symmetry. Although Bloch's theorem is mathematically very elegant, it does not apply to systems with surfaces or randomness.

The recursion technique, introduced by Haydock [Haydock *et.al.* 1972] (details given in Mookerjee 2003) on the other hand, expands solution to the Schrödinger equation in a sequence of increasingly delocalized functions. Considering $|0\}$ to be the orbital on which the solutions are to be projected, the recursion method uses the electronic Hamiltonian H to generate a sequence of orbitals $|1\}, |2\}, \ldots |n\}, \ldots$ which are the successively less-localized . These orbitals are related to one another by H according to the three-term

recurrence relation,

$$H|n\} = \alpha_n|n\} + \beta_{n+1}|n+1\} + \beta_n|n-1\} \tag{5.1}$$

where $|-1\}$ is taken to be zero, and the dependence of these orbitals on position, spin and other coordinates has not been considered. The projection of the solution onto $|0\}$, the projected density of states (PDOS), is the singular part of a solution to the above recurrence, namely the continued fraction,

$$G(E) \;=\; \cfrac{1}{E - \alpha_0 - \cfrac{\beta_1^2}{z - \alpha_1 - \cfrac{\beta_2^2}{z - \alpha_2 - \cfrac{\beta_3^2}{z - \alpha_3 - \cfrac{\beta_4^2}{\ddots}}}}} \tag{5.2}$$

Now, the parameters $\{\alpha_n, \beta_n\}$ need to be determined.

The construction of the three term recurrence relation and its solution as a continued fraction can be carried out either analytically or numerically; the only real difference being whether the parameters $\{\alpha_n, \beta_n\}$ can be expanded as functions of n. In analytic applications, the electronic states are mapped onto systems of orthogonal polynomials which satisfy the same recurrence as the Hamiltonian. When this happens, the PDOS is the weight distribution for the polynomials, and the eigenstates of the Hamiltonian can be expanded in the polynomials. In such cases, the mathematical properties of the many known polynomial systems can be applied to physical problems. Otherwise, the $\{\alpha_n, \beta_n\}$ can be computed using some basis for the $\{n\}$.

In a numerical approach to recursion, the orbitals $\{n\}$ must be expanded in some basis which should be as similar to the recursion orbitals as possible. Though the recursion orbitals are not known beforehand, which is why the numerical approach is essential, still a good choice of basis helps a lot. The best basis is the one for which the Hamiltonian is most sparse, has most of the matrix elements zero. It is seen that this criterion is usually achieved by functions similar to the valence orbitals of atoms, not necessarily orthogonal, but decaying exponentially at large distances. Another essential requirement for the choice

of basis is that it should be easy to calculate the matrix elements of the Hamiltonian. This is facilitated by the use of a two-center approximation (involving a two-center integral). The tight-binding approximation is such an approximation [Bullett D.W.]. It gives very simple parametrization of the Hamiltonian matrix elements for various orientations of the orbitals and atoms. The assumption behind tight-binding is that there are negligible contributions from the potential centered on one atom to Hamiltonian matrix elements for hopping from an orbital centered on a second atom to an orbital centered on a third atom. The d-electrons in transition metals are sufficiently localized for this approximation to work well, but fails quantitatively for less localized valence electrons such as the s- and p-electrons.

In the recursion approach Haydock devised a scheme to transform the basis in such a way that the Hamiltonian of the system has a tri-diagonal form. A new orthonormal basis set $|n\}$ in which the Hamiltonian is tri-diagonal is constructed by the three term recurrence formula mentioned earlier. The first recursion orbital $|0\}$, is assumed to have a normalization of unity, and is the one on which the states are to be projected. Thus this orbital plays a significant role in determining the specific physical property which we shall discuss in our subsequent chapters. Now, we define the new state $|1\}$ as,

$$\beta_1|1\} = H|0\} - \alpha_0|0\} \tag{5.3}$$

The whole set of orthonormal states are generated by the following three term recurrence relation:

$$\beta_{n+1}|n+1\} = H|n\} - \alpha_n|n\} - \beta_n|n-1\} \tag{5.4}$$

α_n and β_n are the coefficients to orthogonalize $H|n\}$ to the preceding vectors $|n\}$, $|n-1\}$ and β_{n+1} is the coefficient to normalize $|n+1\}$ to unity. β_0 is assumed to be unity. In the new basis, the Hamiltonian matrix elements are,

$$\{n|H|n\} = \alpha_n \ ; \ \{n-1|H|n\} = \beta_n \ \text{and} \ \{n|H|m\} = 0 \tag{5.5}$$

In this new representation, the Hamiltonian has the following tri-diagonal form,

$$
\begin{pmatrix}
\alpha_0 & \beta_1 & 0 & 0 & 0 & 0 & 0 \\
\beta_1 & \alpha_1 & \beta_2 & \ddots & 0 & 0 & 0 \\
0 & \beta_2 & \alpha_2 & \beta_3 & \ddots & 0 & 0 \\
0 & \ddots & \beta_3 & \alpha_3 & \beta_4 & \ddots & 0 \\
0 & 0 & \ddots & \ddots & \ddots & \ddots & 0 \\
0 & 0 & \ddots & \ddots & \ddots & \ddots & 0
\end{pmatrix}
\tag{5.6}
$$

The above transformation can be graphically represented as the transformation of a d-dimensional system to a semi-infinite linear chain. $\{\alpha_n\}$ and $\{\beta_n\}$ are represented as the on-site term and the coupling between two sites.

As we have discussed earlier since for systems where the lattice symmetry breaks down, we can not apply Bloch's theorem, so we take recourse to an alternative approach to calculate the electronic properties instead of solving Schrodinger equation. In this approach, properties are extracted from the corresponding Green function of the system which is defined as the resolvent of the Hamiltonian :

$$
G(z) = (zI - H)^{-1}
$$

In the recursion method, we use the same approach and calculate the diagonal elements of the Green function which is directly related to the density of states, spectral functions, structure factors etc. and most of the material properties follow thereafter. The starting state of recursion is then :

$$
|0\} = |R, \alpha\rangle
$$

where R indicates the position of the R-th unit cell and α the Cartesian direction.

The diagonal element of the Green function by definition is,

$$
G_{00}(E) = \{0|(EI - H)^{-1}|0\} = \frac{M_1(E)}{M_0(E)} = \frac{1}{G_1(E)}
$$

where M_0 and M_1 are the determinant of the matrix $(EI - H)^{-1}$ (represented in the new basis $\{|n\}\}$) and the determinant of the matrix obtained from the original matrix by deleting the first row and column respectively.

Using Cauchy's expansion theorem,

$$
\begin{aligned}
M_n(E) &= (E - \alpha_n)M_{n+1} - \beta_{n+1}^2 M_{n+2} \\
G_{n+1} &= E - \alpha_n - \frac{\beta_{n+1}^2}{G_{n+2}}
\end{aligned}
\tag{5.7}
$$

This suggests that it is possible to express the Green function as a continued fraction expansion characterized by a set of coefficients,

$$
G_{00}(E) = \cfrac{1}{E - \alpha_0 - \cfrac{\beta_1^2}{E - \alpha_1 - \cfrac{\beta_2^2}{E - \alpha_2 - \cfrac{\beta_3^2}{E - \alpha_3 - \cfrac{\beta_4^2}{\ddots}}}}}
\tag{5.8}
$$

where the coefficients $\{\alpha_n\}$ and $\{\beta_n\}$ are the ones appearing in the tri-diagonal matrix H.

However, as we will see in the subsequent chapters, for the study of superconductivity the off-diagonal elements of the Green matrices are required as well. For full Green matrices and not only the diagonal elements, a generalization of the recursion method of Haydock *et.al.* 1972 is required. The block recursion technique had been introduced earlier by [Godin and Haydock 1988-Godin and Haydock 1992] in the very different context for obtaining the scattering S-matrix for finite scatterers attached to perfect leads. We shall borrow their ideas and set up a block recursion in the space of electrons and holes of superconductors directly. Using this method we can calculate the Green function for the system which is given by (considering local interaction alone) ::

$$
\mathbf{G}(E) = (E\mathbf{I} - \mathbf{H})^{-1}
\tag{5.9}
$$

Here the bold operators are 2×2 (it is to be noted that this is the case for single-band superconductors, for m-band superconductors the operators have dimension 2m×2m, the rest of the mathematics follows as usual) operators in a space spanned by 'electron' (labeled by +) and 'hole' excitations (labeled by -) :

$$\mathbf{I} = \left(\begin{array}{cc} I & O \\ O & I \end{array} \right) \qquad \mathbf{H} = \left(\begin{array}{cc} H & \Delta \\ \Delta^* & -H^\dagger \end{array} \right)$$

The basis elements are labeled by the site index i, and the electron-hole index α (= + or -) : $\{\Phi_{i\alpha}\}$.

The vector recursion is essentially a change of basis $\{\Phi_{i\alpha}\} \Rightarrow \{\mathbf{V}^{(n)}\}$ with $n = 1, 2, \ldots$, in which the Hamiltonian assumes a block tri-diagonal form. We begin by choosing

$$\mathbf{V}^{(1)} \;=\; (\Phi_{1+} \quad \Phi_{1-}) \;=\; (V_+^{(1)} \quad V_-^{(1)})$$

each member of the row are themselves $2N$ dimensional columns (N being the number of sites i).

The subsequent basis members are generated recursively from the three term recursion relation suggested by Godin and Haydock:

$$\mathbf{H}\mathbf{V}^{(n)} \;=\; \mathbf{V}^{(n-1)}\mathbf{B}_n^\dagger + \mathbf{V}^{(n)}\mathbf{A}_n + \mathbf{V}^{(n+1)}\mathbf{B}_{n+1} \tag{5.10}$$

where $\mathbf{A}_n, \mathbf{B}_{n-1}$ are 2×2 matrices.

The recurrence relation (5.10) gives $\mathbf{A}_n$ from the condition of orthogonality of $\mathbf{V}^{(n)}$ to $\mathbf{V}^{(n+1)}$:

$$\mathbf{A}_n = \left((\mathbf{V}^{(n)})^\dagger \odot \mathbf{V}^{(n)} \right)^{-1} \left((\mathbf{V}^{(n)})^\dagger \odot \mathbf{H}\mathbf{V}^{(n)} \right) \tag{5.11}$$

To calculate $\mathbf{B}^{(n+1)}$ we use the condition of orthogonality of the two columns of $\mathbf{V}^{(n+1)}$. In order to impose this condition we consider:

$$\mathbf{W}^{(n)} \;=\; \mathbf{H}\mathbf{V}^{(n)} - \mathbf{V}^{(n)}\mathbf{A}_n - \mathbf{V}^{(n-1)}\mathbf{B}_n^\dagger \tag{5.12}$$

We construct two (2N) column vectors ξ_+ and ξ_- from the two rows of $\mathbf{W}^{(n)}$ and then set about to Gram-Schmidt orthonormalizing this set:

$$
\begin{aligned}
\xi_+ &= V_+^{(n+1)} \, b_{11} \Rightarrow b_{11} = \left(\xi_+^\dagger \xi_+ \right)^{1/2} \\
\xi_- &= V_+^{(n+1)} \, b_{12} + V_-^{(n+1)} \, b_{22} \\
\Rightarrow b_{12} &= V_+^{(n+1)} \xi_- \quad ; \quad b_{22}^2 = \xi_-^\dagger \xi_- - b_{12}^2
\end{aligned}
$$

By comparing Eqns. (5.10) and (5.12) it is evident that

$$
\mathbf{B}_{n+1} = \begin{pmatrix} b_{11} & 0 \\ b_{12} & b_{22} \end{pmatrix}
$$

Thus initially knowing $\mathbf{V}^{(1)}$ we can calculate $\mathbf{A}_1$ from (5.11). Then we can construct $\mathbf{W}^{(1)}$ (5.12) ($\mathbf{B}_1$ is taken to be zero). Knowing $\mathbf{W}^{(1)}$ (thus corresponding ξ_+ and ξ_-) the different components of $\mathbf{B}_2$ can be obtained by the Gram-Schmidt orthonormalization procedure described above. Then the two columns of $\mathbf{V}^{(2)}$ can be calculated from 5.13 and 5.13 and the procedure repeated resulting in calculation of $\mathbf{A}_2$ and $\mathbf{B}_3$ and so on recursively. $\mathbf{V}^{(n)}$ represents a basis for solution of Schrödinger equation in regions increasingly remote from initial state with increase in n, yielding the coefficients $\mathbf{A}_n, \mathbf{B}_n$ which are in turn less and less significant in determining the local density of states with increasing n.

After performing the above recursion we can write the representation of the Green operator as:

$$
(EI - H)^{-1} = \begin{pmatrix}
E\mathbf{I} - \mathbf{A}_1 & -\mathbf{B}_2 & \mathbf{0} & \mathbf{0} & \ldots \\
-\mathbf{B}_2^\dagger & E\mathbf{I} - \mathbf{A}_2 & -\mathbf{B}_3 & \mathbf{0} & \ldots \\
\mathbf{0} & -\mathbf{B}_3^\dagger & E\mathbf{I} - \mathbf{A}_3 & -\mathbf{B}_4 & \ldots \\
\mathbf{0} & \mathbf{0} & -\mathbf{B}_4^\dagger & \ddots & \\
\vdots & \vdots & \vdots & \vdots & \ddots
\end{pmatrix}^{-1}
\tag{5.13}
$$

where the elements are zero apart from the diagonal and just upper and lower diagonal positions. The (11) element of this can be calculated by repeated applications of the partition theorem or downfolding :

$$
\mathbf{G}(1,1,E) = \left(E\mathbf{I} - \mathbf{A}_1 - \mathbf{B}_2^\dagger \mathbf{G}^{(1)} \mathbf{B}_2 \right)^{-1}
$$

$$\mathbf{G}^{(1)} \;=\; \left(E\mathbf{I} - \mathbf{A}_2 - \mathbf{B}_3^\dagger \mathbf{G}^{(2)}\mathbf{B}_3\right)^{-P_1}$$

$$\mathbf{G}^{(n)} \;=\; \left(E\mathbf{I} - \mathbf{A}_{n+1} - \mathbf{B}_{n+2}^\dagger \mathbf{G}^{(n+1)}\mathbf{B}_{n+2}\right)^{-P_n}$$

n = 1,2, ...   (5.14)

where $\mathbf{O}^{-P_n}$ is an inverse of the operator $\mathbf{O}$ in the sub-space spanned by $\{\mathbf{V}^{(n+1)}, \mathbf{V}^{(n+2)}, \ldots\}$

The recursive calculation described earlier gives rise to a set of continued fraction coefficients $\{\alpha_n, \beta_n\}$ [or $\{A_n, B_n\}$ for Block recursion]. In any practical calculation we can go only up to a finite number of steps, consistent with our computational process. This limits the number of atoms that can be modeled, and also implies that one is always studying a finite system. The terminating continued fraction obtained in this process yields a number of isolated bound states, appropriate for a finite cluster. For most purpose this is an unphysical approximation to the problem under investigation and one needs to overcome these finite size effects by the embedding the cluster in an infinite medium. Mathematically a suitable terminator should be appended to the continued fraction so as to obtain a Green function with a branch cut, rather than a set of simple poles. Several terminators are available in the literature which reflects the asymptotic properties of the continued fraction expansion of the Green function accurately. The advantage of such a termination procedure is that the approximate resolvent retains the analytic properties of the Green function, called the Herglotz properties which are as follows :

- All the singularities of G(z) lie on the real z-axis.

- $\Im m\ [G(z)]>0$ when $\Im m\ (z)<0$ and $\Im m\ [G(z)]<0$ when $\Im m\ (z)>0$.

- G(z)$\rightarrow 1/z$ when $\mathcal{R}e(z)\rightarrow \infty$ along the real axis. Terminator preserves the first 2n-moments of the density of states exactly.

In case the coefficients converge, i.e. if $|\alpha_n - \alpha| \leq \epsilon$, $|\beta_n - \beta|] \leq \epsilon$ for $n \geq N$, we may replace $\{\alpha_n, \beta_n\}$ $[\{A_n, B_n\}]$ by $\{\alpha, \beta\}$ $[\{A, B\}]$ for all $n \geq N$. In that case the asymptotic part of the continued fraction may be analytically summed to obtain :

$$T(E) = (1/2)\left(E - \alpha - \sqrt{(E-\alpha)^2 - 4\beta^2}\right)$$

which gives a continuous spectrum $\alpha - 2\beta \leq E \leq \alpha + 2\beta$. Since the terminator coefficients are related to the band edges and widths, a sensible criterion for the choice of these

asymptotic coefficients is necessary, so as not to give arise to spurious structures in our calculations. Beer and Pettifor 1984 suggested a sensible criterion : given a finite number of coefficients, we must choose $\{\alpha, \beta\}$ in such a way so as to give, for this set of coefficients, the minimum bandwidth consistent with no loss of spectral weight from the band.

5.2   Configuration averaging in disordered systems : Introduction to Augmented Space.

The kind of systems that would be of interest to us in the subsequent chapters of our thesis are binary substitutionally disordered alloys constituted by A and B species having concentrations x and y respectively ($A_x B_y$, $x + y = 1$). We know the amount of A and B species in our system, what we do not know is how are these species arranged on the lattice sites. Or "what is their configuration ?". In order to compare with experiment we need to carry out configuration averaging. The question that we are then encountered with is : "Is such a configuration averaging meaningful?" The problem will be clearly understood if we analyze a specific example. Suppose an experimentalist is carrying out an energy resolved photo-emission study on a disordered metallic alloy. By varying the energy of his incident photon , he can map out the density of states of valence electrons for the alloy. If he carries out the experiment on ten different samples of the same alloy, he should obtain slightly different results. This is because the alloy is random and different samples will have different atomic arrangements of its constituents. What the experimenter actually observes is an average result ; averaged over different realizable configurations of atomic arrangements in the alloy. The same is true for other bulk properties like specific heat, conductivity and different response functions. However if we measure local properties with local probes, the situation is quite different. Configuration averaging will be meaningless if we wish to look at the local properties.

Another point of interest is " Why do we observe configuration averaged results even in a single sample ? " To understand this, we must examine the idea of *spatial ergodicity*. We visualize a macroscopically large system as made up of subsystems each of which resembles a configuration of the system. Spatial ergodicity implies that in the limit of size and the number of subsystems becoming infinitely large, the subsystems of a single

sample exactly replicates all its possible configurations. A global property which averages over the subsystems becomes the same as the averages over all configurations.

Our technique of disorder averaging, namely the augmented space technique goes beyond the usual mean-field approaches like the coherent potential approximation (CPA) [] and is able to consider configuration fluctuations of the local environment. One may find difficulty in physically interpreting this approach for the problem in visualization of the configuration space. But it is possible to overcome this conceptual hurdle through the parallel example of Ising Models with which most of us are well-accustomed. The model consists of a set of *spins* $\{\sigma_R\}$ arranged on a discrete lattice labeled by $\{R\}$. Each spins can have two possible states or *configurations* : $|\uparrow_R\rangle$ and $|\downarrow_R\rangle$. The collection of all linear combinations of these two states i.e. $\{a|\uparrow_R\rangle + b|\downarrow_R\rangle\}$ is called the configuration space of $\{\sigma_R\}$. It is of rank 2 and is spanned by the states $\{|\uparrow_R\rangle , |\downarrow_R\rangle\}$. Let us call this space ϕ_R.

The set of N-spins then have 2^N possible configurations, each of which can be written as a sequence of m-up states and (N-m) down-states. The number (N-m) is defined as the *cardinality* of the configuration and the sequence $\{C\}$ of sites $\{R_{i1}, R_{i2}, R_{i3}, \ldots R_{i_{N_m}}\}$ where the down states sit is called the *cardinality sequence* of configuration. For example take a particular configuration of 4-spins $|\uparrow_1 \downarrow_2 \downarrow_3 \uparrow_4 \rangle$. It has a cardinality 2 and a cardinality sequence $\{2\ 3\}$. Another configuration $|\downarrow_1 \uparrow_2 \uparrow_3 \downarrow_4 \rangle$ also has cardinality 2 but its cardinality sequence is $\{1\ 4\}$ which is distinct from the previous one. For a set of N-spins, the configuration space Φ is of rank 2^N and can be written as the direct product of the configuration spaces of individual spins

$$\Phi = \prod_R^{\otimes} \phi_R$$

For spins having $n > 2$ numbers of realizations, it is quite straight forward to generalize these ideas. The configuration of an individual spin can be labeled as $|\kappa_R\rangle$ where $\kappa_R = 1, 2, \ldots \ldots, n$. The rank of ϕ_R is now n. Also the set of N-spins will have n^N possible configurations.

We can now translate our ideas from spins $\{\sigma_R\}$ to the random occupation variables $\{n_R\}$ for a tight binding model of a binary alloy. The occupation variables associated with a site take the values 0 and 1 when the site is occupied by an atom of the A or B

types. We can immediately visualize the configuration space of the Hamiltonian variable. Whenever a set of random variables $\{n_R\}$ have a binary distribution, their configuration space is isomorphic to the one for a collection of Ising spins.

The random occupation variables $\{n_R\}$ are taken to be independently distributed with positive definite probability densities $p_R\{n_R\}$ and we assume that the $p_R\{n_R\}$ has finite moments to all orders. Clearly it is a reasonable assumption for almost all physical distributions. Since probability densities are positive definite functions therefore it is always possible to express them as spectral densities of positive definite operator N_R as:

$$p_R(n_R) = -\frac{1}{\pi} \, \Im m \left[\langle \emptyset_R | (zI - N_R)^{-1} | \emptyset_R \rangle \right] \qquad (5.15)$$

where $z \to n_R + i\,\delta \; ; \delta \to 0$, and in general if n_R takes k different values with probability x_k , then the configuration space is spanned by k *states* : $|k\rangle$ which are the eigenstates of N_R with eigenvalue k. In that case the *average state* $|\emptyset_R\rangle$, is $\sum_k \sqrt{x_k}|k\rangle$ where x_k is the probability of the variable N_R to take the value k. Thus $|\emptyset_R\rangle$ is the *average* state defined in such a way that for any related quantity containing n_R, $\langle \emptyset_R | \eta | \emptyset_R \rangle$ gives average value of η.

For the binary disorder case, since the resolvent $(zI - N_R)^{-1}$ is Herglotz, and $p_R\{n_R\}$ is assumed to be such that it has finite moments to all orders, so one can expand it as a continued fraction,

$$p_R(n_R) = -\frac{1}{\pi} \Im m \; \cfrac{1}{z - a_0 - \cfrac{b_1^2}{z - a_1}} \qquad (5.16)$$

If n_R takes the value 0 and 1 with probabilities x, $y = (1-x)$ then $p_R(n_R) = y\delta(n_R - 1) + x\delta(n_R)$ we have : $a_0 = x, a_1 = y$ and $b_1 = \sqrt{xy}$, and a representation of N_R is

$$\begin{pmatrix} x & \sqrt{xy} \\ \sqrt{xy} & y \end{pmatrix}$$

As discussed earlier the "average state" $|\emptyset_R\rangle$, is given in terms of the eigenstates of N_R, x_k with eigen values k, as $\sum_k \sqrt{x_k}|k\rangle$. The other members of the countable basis $|n\rangle$ may be obtained recursively from the average state through :

$$\begin{aligned} |0\rangle &= |\emptyset_R\rangle \\ b_1|1\rangle &= N_R \, |0\rangle - a_0|0\rangle \end{aligned}$$

$$\ldots \qquad \ldots \qquad \ldots \qquad \ldots$$

$$b_n|n\rangle \;\; = \;\; N_R\,|n-1\rangle - a_{n-1}|n-1\rangle - b_{n-1}|n-2\rangle$$

In this basis, the operator N_R thus has the traditional form,

$$
\begin{pmatrix}
a_0 & b_1 & 0 & 0 & 0 & \ldots \\
b_1 & a_1 & b_2 & 0 & 0 & \ldots \\
0 & b_2 & a_2 & b_3 & 0 & \ldots \\
0 & 0 & b_3 & a_3 & b_4 & \ldots \\
\ldots & \ldots & \ldots & \ldots & \ldots & \ldots
\end{pmatrix}
$$

We can see that there is a close relationship between the above procedure and the recursion method described in the former section. This is not surprising, since the projected density of states and the probability density are both positive definite and integrable functions. and in both the cases finite moments to all orders exist.

5.2.1 The Augmented Space Theorem

The problem addressed involves the configuration averaging of a function of many independent random variables. e.g. $\ll f(\{n_R\}) \gg$ where R labels a set of lattice points. The first step is to associate with each random variable n_R an operator N_R such that the spectral density of this operator is the probability density of the random variable :

$$p(n_R) = -(1/\pi)\langle \emptyset_R|(n_R I - N_R)^{-1}|\emptyset_R\rangle \tag{5.17}$$

Also to each variable n_R there is associated a *configuration* space ϕ_R spanned by the *states* $\{|\uparrow_R\rangle, |\downarrow_R\rangle\}$ then the augmented space theorem states that the average of any physical quantity $f(n_R)$, which is a function of the set of random variables $\{n_R\}$ is given by

$$\ll f(\{n_R\}) \gg = \langle \emptyset|\tilde{f}(\{N_R\})|\emptyset\rangle \tag{5.18}$$

where $\tilde{f}(\{N_R\})$ is an operator which is a functional of $\{N_R\}$ and has the same form as function $f(\{n_R\})$ of n_R has. Further, $|\emptyset\rangle = \prod_R^{\otimes}|\uparrow_R\rangle$ is the *average configuration state* in the product space $\Phi = \prod_R^{\otimes}\phi_R$. Therefore information about all possible configurations of the disordered system with random variables n_R are kept in the product space Φ. The statement of the theorem will be clear if we see the following mathematical steps.

Let us start with a function $f(n_R)$ of a single random variable n_R. The generalization for a function of the set of many random variables is quite straight forward. The average value of $f(n_R)$ can be expressed as:

$$\ll f(n_R) \gg \; = \; \int_{-\infty}^{\infty} f(n_R) \, p_R(n_R) dn_R$$

$$= \; -\frac{1}{\pi} \Im m \int_{-\infty}^{\infty} f(n_R) \langle \uparrow_R |(n_R I - N_R)^{-1}| \uparrow_R \rangle dn_R$$

Since the eigen vectors of the operator N_R on the configuration space is a complete set, we can write

$$\ll f(n_R) \gg \; = \; -\frac{1}{\pi} \Im m \sum_k \sum_{k'} \int_{-\infty}^{\infty} f(n_R) \langle \uparrow_R |k\rangle \langle k|(n_R I - N_R)^{-1}|k'\rangle \langle k'| \uparrow_R \rangle dn_R$$

But $(n_R I - N_R)^{-1}$ is diagonal in the eigen-basis of N_R and is equal to $\delta_{kk'}(1/n_R - k)$, so

$$\ll f(n_R) \gg \; = \; \sum_k \int_{-\infty}^{\infty} f(n_R) \langle \uparrow_R |k\rangle \left[-\frac{1}{\pi} \Im m(n_R - k)^{-1} \right] \langle k| \uparrow_R \rangle dn_R$$

$$= \; \langle \uparrow_R | \sum_k |k\rangle \int_{-\infty}^{\infty} [f(n_R)\delta(n_R - k)dn_R] \langle k| \uparrow_R \rangle$$

$$= \; \langle \uparrow_R | \{ \sum_k |k\rangle f(k)\langle k| \} | \uparrow_R \rangle \tag{5.19}$$

Now $\sum_k |k\rangle f(k)\langle k|$ is nothing but the spectral representation of the functional $\tilde{f}(N_R)$ of the operator N_R constructed by simply replacing the variable n_R with the associated operator N_R in $f(n_R)$. Hence

$$\ll f(n_R) \gg \; = \; \langle \uparrow_R |\tilde{f}(N_R)| \uparrow_R \rangle \tag{5.20}$$

In general if there are independent random variables $\{n_R\}$ involved then the joint probability distribution is given by :

$$P(n_{R_1}, n_{R_2}, \ldots n_{R_i} \ldots) = \prod_i p_i(n_{R_i})$$

Proceeding in the same way we shall get average of functions of the set of random variables as:

$$\ll f(\{n_R\}) \gg = \langle \emptyset |\tilde{f}(\{\widetilde{N}_R\})|\emptyset \rangle$$

The operator $\widetilde{N}_R$ are built up from the operators N_R as :

$$\widetilde{N}_R = I \otimes I \otimes \ldots \otimes N_R \otimes I \otimes \ldots$$

and $|\emptyset\rangle$ is the average state in the full configuration space Φ.

This theorem makes an extremely strong statement - the configuration average of the function of a set of random variables is equal to the matrix element of the function in the augmented space constructed according to the prescription given above by using probability distribution of the random variables. The price that one has to pay for this simplification is that now one has to define the disordered function or operators in a much enlarged space formed as a combination of the configuration space and real Hilbert space. However, it has been shown [Saha *et.al.* 1994b,Dasgupta *et.al.* 1995] that the point group symmetries of the underlying lattice, the symmetry of the starting state and the underlying symmetries of the configuration space (in case the disorder is homogeneous), drastically reduce the rank of the invariant sub-space on which the recursion effectively acts. In the subsequent chapters we are going to discuss how the theorem can be utilized for performing configuration averaging in different disordered binary systems and a generalized version of this formalism even deals with correlated random fluctuations.

Chapter 6

A study of single-band superconductivity in binary disordered alloys using the augmented space formalism.

6.1 Introduction

Superconductivity is a phenomenon which is quite common in nature since there are several hundred superconducting materials known to mankind. Before 1986 the highest known T_c values were in materials like Nb_3Ge ($T_c = 23K$). This, and the closely related compound Nb_3Sn ($T_c = 18K$) are very popular in superconducting magnet industry.

In 1986 Bednorz and Müller discovered that the material $La_{2-x}Ba_xCuO_4$ becomes superconducting with a T_c which is maximum at 38K for $x \approx 0.15$. Within a short time the related compound $YBa_2Cu_3O_7$ was discovered to have T_c=92K. This discovery marked the beginning of the era of "high temperature superconductivity". Other high temperature superconductors have been discovered in chemically related systems.

Other than high temperature superconductors, there are also many other interesting superconducting materials. Some of these have such exotic properties which are still a matter of active study for clearer understanding. These include other oxide-based superconducting materials, organic superconductors, C_{60} based fullerene superconductors, and "heavy fermion" superconductors (typically compounds containing the elements U or Ce) which have strong electron-electron interaction effects. Other superconductors have surprising properties, such as coexistence of magnetism and superconductivity, or evidence of exotic "unconventional" superconducting phases.

In 1957 Bardeen, Cooper and Schrieffer (BCS) published the first truly microscopic theory of superconductivity. The theory explained a number of important experimental phenomena and was soon established to be correct in all essential respects. BCS theory built upon three major insights: (i) The effective forces between the electrons can sometimes be attractive in a solid rather than repulsive. This is due to coupling between the electrons and the phonons of the underlying crystal lattice. (ii) Cooper considering the simple system of just two electrons outside an occupied Fermi surface found that the electrons form a stable pair bound state irrespective of the magnitude of the attractive force between them. (iii) Finally Schrieffer constructed a many-particle wave function for the system in which all the electrons near the Fermi surface are paired up.

There has been considerable interest, during the last decade, in the study of the effects of disorder on superconducting properties of materials and inhomogeneous superconductors such as those enclosed by surfaces [Goldman and Markovic 1998] or modified by magnetic fields. The Bogoliubov-de Gennes (BdG) formalism [de Gennes 1966] provides a natural framework for a fully microscopic description of these phenomena. Unfortunately the BdG equations are difficult to solve as compared to simpler, phenomenological approaches. In the recent times, however, there has been progress in the development of new methods of solution for the BdG equations, both in real [Ghoshal *et.al.* 1998, Ghoshal *et.al.* 2001, Litak *et.al.* 1995, Martin and Annett 1998, Zhu *et.al.* 2003, Bagwell 1994, Czajka *et.al.* 2005, Morr and Yoon 2006, Hayashi and Ebisawa 2005, Covaci and Marsiglio 2006, Mizushima *et.al.* 2005] and in reciprocal spaces [Linder and Sudbo 2008]. There exists quite a large body of work where BdG equations have been solved in conjunction with the mean-field, single-site coherent potential approximation (CPA) [Moradian *et.al.* 2000, Martin *et.al.* 1999, Litak and Györffy 2000] in order to understand the physics of disordered superconductors. BdG equations have been solved in reciprocal space for realistic model Hamiltonians for the high T_c cuprates [Szotek *et.al.* 1996] . They have also been solved using the real space based recursion method to study interface properties of d and s wave superconductors [Martin and Annett 1998]. The real space based approach is attractive since lattice periodicity is not an a priori requirement. As a result large variety of problems related to inhomogeneous superconductors may be treated. This has been illustrated in several recent works [Ghoshal *et.al.* 1998, Ghoshal

et.al. 2001, Ghoshal and Kee 2004, Moradian *et.al.* 2000, Litak *et.al.* 1995, Czajka *et.al.* 2005, Morr and Yoon 2006, Martin *et.al.* 1999, Cheng and Su 2005, Aryanpour *et.al.* 2006].

The effect of disorder on superconductivity is usually discussed in the framework of the Anderson's theorem [Anderson 1959]. For *s*-wave superconductors, Anderson's theorem asserts that if the perturbation by disorder preserves the time-reversal invariance and the coherence length is long enough to guarantee that the pairing potential Δ does not fluctuate, then the absolute gap in the quasi-particle spectrum survives. The main effect of disorder is that the gap equation is modified where the density of normal state appearing in the gap equation is now replaced by its average over configurations. In contrast, for the case of superconductors whose Cooper pairs are of the exotic *p*-wave [Rieck *et.al.* 2007] or *d*-wave [Martin *et.al.* 1999, Cheng and Su 2005, Asano *et.al.* 2006, Ghoshal and Kee 2004] character, even simple potential scattering, which does not break time-reversal symmetry causes pair breaking. The above scenario, discussed in the framework of Anderson's theorem, is applicable only in the low disorder regime where the mean free path is much larger than the Fermi wave vector.

In this chapter[1] we present a real-space approach to study the effect of disorder on superconductivity. Our method of disorder averaging is the augmented space formalism which was introduced in the previous chapter. We shall apply our method to two situations : first, a tight-binding, negative U Hubbard model with only on-site disorder and next a random negative U Hubbard model where electrons attract each other provided they are near certain randomly placed centers. In the second example, we shall address the issue of how many such centers are necessary to make the ground state superconducting. In this model the pairing potential will fluctuate and Anderson's theorem as described above may not be applicable. We shall examine our method in this limit. Having established our method in these two well studied limits, we shall consider the physics of superconducting alloys with correlated disorder. Since the mean-field CPA techniques cannot deal with

---

[1]The contents of this chapter has been published in two papers : (1) Shreemoyee Ganguly, A. Venkata-subramanium, K. Tarafder, Indra Dasgupta and A. Mookerjee, *Augmented space recursion study of the effects of disorder on superconductivity*, Phys Rev B **79**, 224204 (2009) (2) Shreemoyee Ganguly, Indra Dasgupta and Abhijit Mookerjee, *A real space approach to study the effect of off-diagnonal disorder on superconductivity*, Physica C **470**, 640 (2010)

short-ranged order, the advantage of the augmented space technique which goes beyond mean-field approximations for configuration averaging, will become immediately evident.

In the present chapter we will also illustrate the viability of our methodology for systems with off-diagonal randomness. Off-diagonal randomness for example is realized in alloys where there is a local lattice distortion because of size mismatch of the constituents, and introduces disorder in the off-diagonal hopping integral in a tight-binding model. Thus the nearest neighbour hopping integral for a binary AB alloy with off-diagonal disorder takes values t^{AA}, t^{BB} and t^{AB}, according to whether there is AA, BB or AB type of alloy occupancy in neighbouring sites. It is interesting to note, a treatment of off-diagonal disorder is non-trivial. Unless simplified assumptions are made about off-diagonal disorder [2] the single-site CPA cannot deal with problems involving correlated randomness involving more than one site. The only mean-field work which included the effect of off-diagonal disorder in superconductivity was by Michalik and Wysokiński [Michalik and Wysokiński 2004, Michalik and Wysokiński 2006] who used a version of the CPA proposed by Blackman *etal* [Blackman *et.al.* 1971] to incorporate off-diagonal disorder. We emphasize here that it is in the ability to treat inhomogeneous and off-diagonal disorder that the real strength of the ASF becomes particularly evident and this will be clear from the discussions of the present chapter.

6.2   Our Model Hamiltonian.

To analyze the effect of disorder on a superconducting system we shall begin with the simplest model, namely the single-band attractive Hubbard Hamiltonian in model lattices. The Hamiltonian is given by

$$\mathbf{H} \;=\; -\sum_{\langle i,j\rangle,\sigma} t_{ij}(c_{i\sigma}^{\dagger}c_{j\sigma} + c_{j\sigma}^{\dagger}c_{i\sigma}) + \sum_{i\sigma}(\varepsilon_i - \mu_i)n_{i\sigma} - \sum_{\langle i,j\rangle,\sigma,\sigma'}|U_{ij}|n_{i\sigma}n_{j\sigma'} \qquad (6.1)$$

Here $\{c_{i\sigma}^{\dagger}, c_{i\sigma}\}$ are the usual electron creation and annihilation operators with spin σ on site labeled i of a square or a cubic lattice. The local charge density operator is $n_i = n_{i\uparrow} + n_{i\downarrow}$, where $n_{i\sigma} = c_{i\sigma}^{\dagger}c_{i\sigma}$; μ is the chemical potential, t the nearest-neighbour

---

[2]Assumptions include either $t_{ij}^{AB} = (t_{ij}^{AA} + t_{ij}^{BB})/2$ or $t_{ij}^{AB} = \sqrt{t_{ij}^{AA}t_{ij}^{BB}}$

hopping amplitude and ε_i the local on-site energy at the site labeled i. In this model, if $U_{ij} = -|U_{ii}|\delta_{ij}$ and $\sigma \neq \sigma'$, then the local attractive interaction gives rise to s-wave pairing. Whereas $U_{ij} = -|U_{ij}|(1 - \delta_{ij})$, where j is a nearest neighbour of i on the lattice, then the non-local attractive interaction gives rise to d-wave pairing.

The BdG mean field decomposition [de Gennes 1966] of the interaction terms give expectation values to the local and non-local pairing amplitudes:

$$\Delta_{ii} = -|U_{ii}| \langle c_{i\downarrow}c_{i\uparrow}\rangle \qquad \Delta_{ij} = -|U_{ij}| \langle c_{i\downarrow}c_{j\uparrow}\rangle \tag{6.2}$$

and also to the local and non-local *"densities"*:

$$\langle n_{i\sigma}\rangle = \langle c_{i\sigma}c_{i\sigma}^{\dagger}\rangle \qquad \langle n_{ij\sigma}\rangle = \langle c_{i\sigma}c_{j\sigma}^{\dagger}\rangle \tag{6.3}$$

The effective quadratic BdG Hamiltonian becomes :

$$\mathbf{H}_{\text{eff}} = -\sum_{i\neq j,\sigma} t_{ij}^{*} \, c_{i\sigma}^{\dagger}c_{j\sigma} + \sum_{i\sigma}(\varepsilon_i - \mu_i^{*}) \, n_{i\sigma} + \begin{cases} \sum_i \left(\Delta_{ii}c_{i\uparrow}^{\dagger}c_{i\downarrow}^{\dagger} - \Delta_{ii}^{*}c_{i\uparrow}c_{i\downarrow}\right) \\ \sum_{i\neq j}\left(\Delta_{ij}c_{i\uparrow}^{\dagger}c_{j\downarrow}^{\dagger} - \Delta_{ij}^{*}c_{i\uparrow}c_{j\downarrow}\right) \end{cases}$$

$$\tag{6.4}$$

where the top line refers to s-wave and the bottom to d-wave pairing. $\mu_i^{*} = \mu - |U_{ii}|\langle n_i\rangle/2$ incorporates the site dependent Hartree shift and $t_{ij}^{*} = t_{ij} + |U_{ij}|\langle n_{ij}\rangle/2$ is the renormalized hopping integral. The extra feature of the Hamiltonian is that some of its terms are random. This effective Hamiltonian can be diagonalized by using the following transformation:

$$c_{i\uparrow} = \sum_n [\beta_{n\uparrow}u_n(r_i) - \beta_{n\downarrow}^{\dagger}v_n^{*}(r_i)]$$
$$c_{i\downarrow} = \sum_n [\beta_{n\downarrow}u_n(r_i) + \beta_{n\uparrow}^{\dagger}v_n^{*}(r_i)] \tag{6.5}$$

where β and $\beta^{\dagger}$ are quasi-particle operators, and $u_n(r_i)$, $v_n(r_i)$ are the quasi-particle amplitudes associated with an eigen energy E_n.

Under the Hartree-Fock mean-field approximation incorporating charge-order and superconducting decoupling along with the above canonical-transformation we have,

$$\begin{pmatrix} H & \Delta \\ \Delta^* & -H^\dagger \end{pmatrix} \begin{pmatrix} u_n(r_i) \\ v_n(r_i) \end{pmatrix} = E_n \begin{pmatrix} u_n(r_i) \\ v_n(r_i) \end{pmatrix} \tag{6.6}$$

where (the excitation eigen-value $E_n \geq 0$)

$$\begin{aligned}
Hu_n(r_i) &= -\sum_j \left(t + \frac{1}{2}|U_{ij}|\langle n_{ij} \rangle \right) u_n(r_j) + (\epsilon_i - \mu_i^*) u_n(r_i) \\
\Delta u_n(r_i) &= \Delta_i u_n(r_i) + \Delta_{ij} u_n(r_j)
\end{aligned} \tag{6.7}$$

j is the nearest neighbour of i We can express the particle density $\langle n_i \rangle$ and the pairing potential in terms of the quasi-particle amplitude as

$$\begin{aligned}
\langle n_i \rangle &= 2 \sum_n |u_n(r_i)|^2 f_n + |v_n(r_i)|^2 (1 - f_n) \\
\Delta_i &= |U_{ii}| \sum_n v_n^*(r_i) u_n(r_i) f_n - u_n(r_i) v_n^*(r_i)(1 - f_n) \\
\langle n_{ij} \rangle &= 2 \sum_n u_n^*(r_i) u_n(r_j) f_n + v_n(r_i) v_n^*(r_j)(1 - f_n) \\
\Delta_{ij} &= |U_{ij}| \sum_n v_n^*(r_i) u_n(r_j) f_n - u_n(r_i) v_n^*(r_j)(1 - f_n)
\end{aligned}$$

$$\tag{6.8}$$

f_n is the Fermi function. A fully self-consistent solution of (6.6) can be obtained provided both the normal potentials ($|U_{ii}|n_i$ and $|U_{ij}|n_{ij}$) and anomalous potentials (Δ_i and Δ_{ij}) are determined consistently with Eqns. (6.8).

As mentioned earlier since the Hamiltonian is random so all the physical quantities of interest (6.8) in such systems require to be configuration averaged. Earlier works had used the single-site CPA for this averaging. We shall turn to the augmented space recursion method (ASR) introduced by Mookerjee [Mookerjee 1973] for this purpose.

The self-consistency criteria is set to 10^{-6} for calculation of all self-consistent parameters through out the present study. Clearly the normal Hartree-Fock term $|U_{ii}|\langle n_i \rangle / 2$ is important as it gives rise to the position dependent shift of the on-site energy. In our present case for the tight binding lattice, we shall consider only the nearest neighbor hopping interaction t. It is clear from the definition that if the coupling between the particle

and hole space via the superconducting order parameter Δ is purely local (*ie.* $U_{ij} = 0$), then the pairing potential will also be purely local (i.e., $\Delta_{ij}=0$) and when the interaction is non-local (i.e., $U_{ij} \neq 0$) , then non-local coupling between particle and hole space is present (i.e., $\Delta_{ij} \neq 0$).

6.2.1   Disorder and superconductivity.

To analyze the effect of disorder on a superconducting system we shall begin with the simplest model, namely the single-band attractive Hubbard Hamiltonian described in the equation (6.4) but with the extra feature that some of its terms are random. This disordered attractive Hubbard model as mentioned previously has also been widely used to study superconductivity in disordered s-wave [Litak and Györffy 2000, Ghoshal *et.al.* 1998, Ghoshal *et.al.* 2001, Aryanpour *et.al.* 2006, Moradian *et.al.* 2000] and d-wave [Martin *et.al.* 1999, Cheng and Su 2005] superconductors. We shall assume that the randomness will be substitutional, binary and homogeneous. It can be characterized by a set of random *occupation* variables $\{m_i\}$, which take the values 1 or 0 according to whether the site labeled i is occupied by a A or a B type of atom.

In this chapter we will be studying both s- and d-wave superconductivity in disordered systems with diagonal and off-diagonal disorder and in the following we shall define our model for disorder.

a) s-wave superconductivity

We will consider randomness in the simplest possible diagonal term, namely the on-site energy term which is diagonal in both particle-hole space and real (lattice) space.

$$\varepsilon_i \;\; = \;\; \varepsilon^B + \delta\varepsilon \; m_i \tag{6.9}$$

Physically, this implies depending on whether a site is occupied by an A or B kind of species it has corresponding on-site energy ϵ_A or ϵ_B. In addition we also consider the effect of randomness in the off-diagonal term :

$$t_{ij} \;\; = \;\; t^{BB} + t^{(1)}(m_i + m_j) + t^{(2)}m_i m_j \tag{6.10}$$

Randomness in the hopping amplitude is caused because depending upon whether a site is occupied by A or B kind of species and its nearest neighbour to which an electron may hop is of A or B kind, t_{ij} takes on values t^{AA}, t^{AB} and t^{BB}.

We will also consider randomness in U_{ii} causing randomness in Δ_i later in this chapter in the section "Random negative U Hubbard model". *b) d-wave superconductivity*

Here we shall again consider randomness in the diagonal term, namely the on-site energy term and the off-diagonal (hopping) term:

$$\begin{aligned}
\varepsilon_i &= \varepsilon^B + \delta\varepsilon\ m_i \\
t_{ij}^* &= t^{*BB} + t^{*(1)}(m_i + m_j) + t^{*(2)}m_i m_j
\end{aligned}$$

$$(6.11)$$

The renormalized hopping integral [defined below Eqn (6.4)] again may take on values t^{*AA}, t^{*AB} or t^{*BB} depending upon the kind of species that occupies the site i and its nearest neighbour j. Further we have used the notation $\delta\epsilon = D = \epsilon^A - \epsilon^B$. For off-diagonal disorder we have, $\lambda^{(1)} = \lambda^{AB} - \lambda^{BB}$, $\lambda^{(2)} = \lambda^{AA} + \lambda^{BB} - 2\lambda^{AB}$ here λ is the off-diagonal potential parameters of the model which is the hopping t for s-wave superconductivity and renormalized hopping t^* for d-wave superconductivity. In absence of any off-diagonal disorder, $\lambda^{AA} = \lambda^{BB} = \lambda^{AB} = \lambda$. In the following we shall represent the off-diagonal randomness in terms of λ *viz.* $\lambda^{AA} = \kappa\lambda$, $\lambda^{BB} = \beta\lambda$ and $\lambda^{AB} = \Gamma\lambda$, such that

$$\lambda^{(1)} = (\Gamma - \beta) \qquad \lambda^{(2)} = \kappa + \beta - 2\Gamma \qquad (6.12)$$

in units of λ. Further the parameter $\delta = (\lambda^{AA} - \lambda^{BB}) = (\kappa - \beta)\lambda$ characterize the strength of off-diagonal disorder similar to $\delta\epsilon$ for diagonal disorder.

The class of systems with which we shall begin our study will be substitutional binary disordered alloys. As the Hamiltonian parameters are random, our description will form a configuration averaged picture as described below:

If the concentrations of A and B-type of atoms in the solid are x and y, then the probability density of the random occupation variables m_i, is given by :

$$p(m_i) = x\delta(m_i - 1) + y\delta(m_i)$$

The 'configuration space' of m_i, Φ_i, has rank 2 and is spanned by the states $|A_i\rangle$ and $|B_i\rangle$.

The augmented space formalism associates with each random variable m_i an operator M_i acting on its configuration space Φ_i and whose spectral density is its probability density (as given by Eqn 5.17 in Chapter 5; however in the present chapter unlike Chapter 5 we have used index i to label the lattice points instead of R, m_i as our random variable instead of n_R and M_i as the corresponding operator instead of N_R)::

$$p(m_i) = -\frac{1}{\pi} \lim_{\delta \to 0} \Im m \, \langle \emptyset_i | [(m_i)I - M_i]^{-1} | \emptyset_i \rangle \tag{6.13}$$

where $|\emptyset_i\rangle = \sqrt{x}|A_i\rangle + \sqrt{y}|B_i\rangle$ is the 'reference' state . The other basis member is $|1_i\rangle = \sqrt{y}|A_i\rangle - \sqrt{x}|B_i\rangle$ which is a state with one 'fluctuation' about the reference state at the site i. The configuration states $|A_i\rangle$ and $|B_i\rangle$ are the eigenkets of $\mathbf{M}_i$ corresponding to eigenvalues 1 and 0.

A representation of this operator in the basis is :

$$M_i = x + (y - x) \, \gamma_i^\dagger \gamma_i + \sqrt{xy} \, \left(\gamma_i^\dagger + \gamma_i \right) \tag{6.14}$$

The operator $\gamma_i^\dagger$ creates a configuration fluctuation at the site i about this reference state, e.g. $\gamma_i^\dagger |\emptyset_i\rangle = |1_i\rangle$). Since each site can have only two states, only *one* fluctuation is allowed per site. Thus γ_i are fermion-like operators and $\gamma_i^\dagger |1_i\rangle = 0$ and $\gamma_i |\emptyset_i\rangle = 0$.

The augmented space theorem [Mookerjee 1973] states that the configuration average of a function of a set of independent random variables can be expressed as a matrix element in the full configuration space of the disordered system $\Phi = \prod^{\otimes} \Phi_i$,

Following the prescription given by this theorem for the purpose of configuration averaging (as discussed in Chapter 5 of the thesis in the section "The Augmented Space Theorem") we need to construct the Hamiltonian in the augmented space $\Psi = \mathcal{H} \otimes \prod_i^{\otimes} \Phi_i$ by replacing all the random variables shown in Eqns. (6.9)-(6.11) by the corresponding operators. As described earlier for $s-$wave superconductivity we have randomness both in the onsite (ϵ_i) and hopping (t_{ij}) terms (we introduce randomness in the local pairing potential U_{ii} only in the section on "Random negative U Hubbard model"). The effective

augmented space Hamiltonian becomes :

$$
\begin{aligned}
\widetilde{\mathbf{H}}_{\text{eff}} &= \sum_{i\sigma}(\langle\langle\varepsilon\rangle\rangle - \mu^*)\, n_{i\sigma} - \sum_{i\neq j,\sigma}\langle\langle t_{ij}\rangle\rangle c^\dagger_{i\sigma}c_{j\sigma} + \sum_{i\sigma}\delta\varepsilon\, n_{i\sigma}\, F_i \ldots \\
&\quad - \sum_{i\neq j,\sigma} t^{(1)}_{ij} c^\dagger_{i\sigma}c_{j\sigma}\{F_i + F_j\} - \sum_{i\neq j,\sigma} t^{(2)}_{ij} c^\dagger_{i\sigma}c_{j\sigma}\{F_i\, F_j\} \\
&\quad + \sum_i(\Delta_{ii}c^\dagger_{i\uparrow}c^\dagger_{i\downarrow} - \Delta^*_{ii}c_{i\uparrow}c_{i\downarrow})
\end{aligned}
$$

(6.15)

Here, $\langle\langle\varepsilon\rangle\rangle$ and $\langle\langle t_{ij}\rangle\rangle$ gives the concentration averaged values of on-site energy and hopping amplitudes respectively. $F_i = (y - x)\,\gamma^\dagger_i\gamma_i + \sqrt{xy}\left(\gamma^\dagger_i + \gamma_i\right)$

For d-wave superconductivity with randomness in ϵ_i, and t_{ij} the corresponding effective Hamiltonian in the augmented space becomes:

$$
\begin{aligned}
\widetilde{\mathbf{H}}_{\text{eff}} &= \sum_{i\sigma}(\langle\langle\varepsilon\rangle\rangle - \mu)\, n_{i\sigma} - \sum_{i\neq j,\sigma}\langle\langle t^*_{ij}\rangle\rangle c^\dagger_{i\sigma}c_{j\sigma} + \sum_{i\sigma}(\delta\varepsilon)\, n_{i\sigma}\, F_i \ldots \\
&\quad - \sum_{i\neq j,\sigma} t^{*(1)}_{ij} c^\dagger_{i\sigma}c_{j\sigma}\{F_i + F_j\} - \sum_{i\neq j,\sigma} t^{*(2)}_{ij} c^\dagger_{i\sigma}c_{j\sigma}\{F_i\, F_j\} \\
&\quad + \sum_{i\neq j}\left(\Delta_{ij}c^\dagger_{i\uparrow}c^\dagger_{j\downarrow} - \Delta^*_{ij}c_{i\uparrow}c_{j\downarrow}\right)
\end{aligned}
$$

(6.16)

We gather from the above equation, all the configuration space operators can be written in terms of operators involving F_i. They are either I or $\sum_i A_i F_i = \mathcal{F}^{(1)}$ or $\sum_{ij} B_{ij}F_iF_j = \mathcal{F}^{(2)}$. The operator $\mathcal{F}^{(1)}$ either counts or creates and annihilates configuration fluctuations at single sites, while the operator $\mathcal{F}^{(2)}$ counts or creates and annihilates a pair of configuration fluctuations simultaneously at two sites. In the absence of off-diagonal disorder and for off-diagonal disorder where we assume that for any two-site parameter $2\lambda^{AB} = \lambda^{AA} + \lambda^{BB}$ ($\kappa + \beta = 2\Gamma$), $\mathcal{F}^{(2)}$ vanishes, we have only single site configuration fluctuations and single site approximations like the CPA becomes applicable. In the general case, the last term describes correlated simultaneous configuration fluctuations at two sites, a natural consequence of off-diagonal disorder. In this work, our aim will be to carry out configuration averaging in the presence of off-diagonal disorder without resorting to any approximations.

The Bogoliubov-de Gennes transformation then introduces the electron and hole sub-spaces with an effective coupled electron-hole Schrödinger like equation :

$$\begin{pmatrix} \widetilde{H} & \widetilde{\Delta} \\ \widetilde{\Delta}^* & -\widetilde{H}^\dagger \end{pmatrix} \begin{pmatrix} u(E,\vec{r}_i) \\ v(E,\vec{r}_i) \end{pmatrix} = E\widetilde{I} \begin{pmatrix} u(E,\vec{r}_i) \\ v(E,\vec{r}_i) \end{pmatrix} \tag{6.17}$$

where,

$$\underline{\underline{\widetilde{H}}} = \begin{pmatrix} \widetilde{H} & \widetilde{\Delta} \\ \widetilde{\Delta}^* & -\widetilde{H}^\dagger \end{pmatrix}$$

After constructing the BdG Hamiltonian (6.17) in the augmented electron-hole space, we block tridiagonalize it using the vector recursion technique [Godin and Haydock 1988] :

$$
\begin{aligned}
|1 \gg \ &= \ \begin{pmatrix} u(E,\vec{r}_0) \otimes \{\emptyset\} \\ v(E,\vec{r}_0) \otimes \{\emptyset\} \end{pmatrix} \\
\underline{B}^\dagger_{n+1}|n+1 \gg \ &= \ \underline{\underline{\widetilde{H}}} \, |n \gg -\underline{A}_n|n \gg -\underline{B}_n|n-1 \gg
\end{aligned}
$$

The coefficients $\underline{A}_n$ and $\underline{B}_n$ are obtained from the orthogonality of the generated basis and between rows of the same basis [Godin and Haydock 1988, Godin and Haydock 1992] as described in details in Chapter 5. The configuration averaged diagonal matrix element of the Green function then follows as a matrix continued fraction :

$$\ll \underline{G}(\vec{r}_0,\vec{r}_0;E) \gg = \ll 1|\mathbf{G}|1 \gg = \underline{\underline{G}}_0(E)$$

$$\underline{G}_n(E) = \left(z\underline{\underline{I}} - \underline{\underline{A}}_n - \underline{B}^\dagger_{n+1}\underline{\underline{G}}_{n+1}(E)\underline{\underline{B}}_{n+1} \right)^{-P_{n-1}}$$

$$n \ = \ 0,1,2,\ldots N_2 - 1$$

where A^{-P_n} denotes inverse in the subspace spanned by the basis $\{|n+1 \gg, |n+2 \gg \ldots\}$. The matrix continued fraction is terminated in two steps. The matrix coefficients $\{\underline{A}_n, \underline{B}_n\}$

are calculated exactly for $n < N_1$, then : first, by putting $\underline{A}_n = \underline{A}_{N_1}$ and $\underline{B}_n = \underline{B}_{N_1}$ for all $N_1 \leq n < N_2$ and second, $\underline{G}_{N_2}(E) = (E + i\eta)^{-1} \underline{I}$

If we had started the recursion from a different starting state :

$$|1 \gg = \left(\begin{array}{c} \left[\{u(E,\vec{r}_0) + u(E,\vec{r}_1)\}/\sqrt{2} \right] \otimes \{\emptyset\} \\ \left[\{v(E,\vec{r}_0) + v(E,\vec{r}_1)\}/\sqrt{2} \right] \otimes \{\emptyset\} \end{array} \right)$$

The same vector recursion gives :

$$\ll 1|\underline{G}(E)|1 \gg = \ll \underline{G}(\vec{r}_0, \vec{r}_0; E) \gg + \ll \underline{G}(\vec{r}_0, \vec{r}_1; E) \gg$$

We have assumed that

$$\ll \underline{G}(\vec{r}_0, \vec{r}_0; E) \gg = \ll \underline{G}(\vec{r}_1, \vec{r}_1; E) \gg \quad \text{and} \quad \ll \underline{G}(\vec{r}_0, \vec{r}_1; E) \gg = \ll \underline{G}(\vec{r}_1, \vec{r}_0; E) \gg$$

The 2×2 electron-hole Green matrix is :

$$\ll \underline{G}(\vec{r}_i, \vec{r}_j; E) \gg = \left(\begin{array}{cc} \ll G^{++}(\vec{r}_i, \vec{r}_j; E) \gg & \ll G^{+-}(\vec{r}_i, \vec{r}_j; E) \gg \\ \ll G^{-+}(\vec{r}_i, \vec{r}_j; E) \gg & \ll G^{--}(\vec{r}_i, \vec{r}_j; E) \gg \end{array} \right) \tag{6.18}$$

We can express the particle density and the pair interaction potential and related terms off diagonal in real space in terms of the elements of the Green matrix as :

$$\langle n_i \rangle = -\frac{1}{\pi} \Im m \lim_{\delta \to 0} \int_{-\infty}^{\infty} \Big[\ll G^{++}(\vec{r}_i, \vec{r}_i, E + i\eta) \gg f_n \dots$$
$$\dots + \ll G^{--}(\vec{r}_i, \vec{r}_i, E + i\eta) \gg (1 - f_n) \Big] dE$$

$$\Delta_{ii} = -\frac{1}{\pi} \Im m \lim_{\delta \to 0} \int_{-E_c}^{+E_c} \Big[\ll G^{+-}(\vec{r}_i, \vec{r}_i, E + i\eta) \gg f_n + \dots$$
$$\dots + \ll G^{-+}(\vec{r}_i, \vec{r}_i, E + i\eta) \gg (1 - f_n) \Big] dE$$

$$\langle n_{ij} \rangle = -\frac{1}{\pi} \Im m \lim_{\delta \to 0} \int_{-\infty}^{\infty} \Big[\ll G^{++}(\vec{r}_i, \vec{r}_j, E + i\eta) \gg f_n + \dots$$
$$\dots + \ll G^{--}(\vec{r}_i, \vec{r}_j, E + i\eta) \gg (1 - f_n) \Big] dE$$

$$\Delta_{ij} = -\frac{1}{\pi} \Im m \lim_{\delta \to 0} \int_{-E_c}^{+E_c} \Big[\ll G^{+-}(\vec{r}_i, \vec{r}_j, E + i\eta) \gg f_n + \dots$$
$$\dots + \ll G^{-+}(\vec{r}_i, \vec{r}_j, E + i\eta) \gg (1 - f_n) \Big] dE \tag{6.19}$$

The vector recursion method in the augmented space provides an elegant scheme to compute all the quantities of interest in the BdG formalism. In the following section we shall discuss our results.
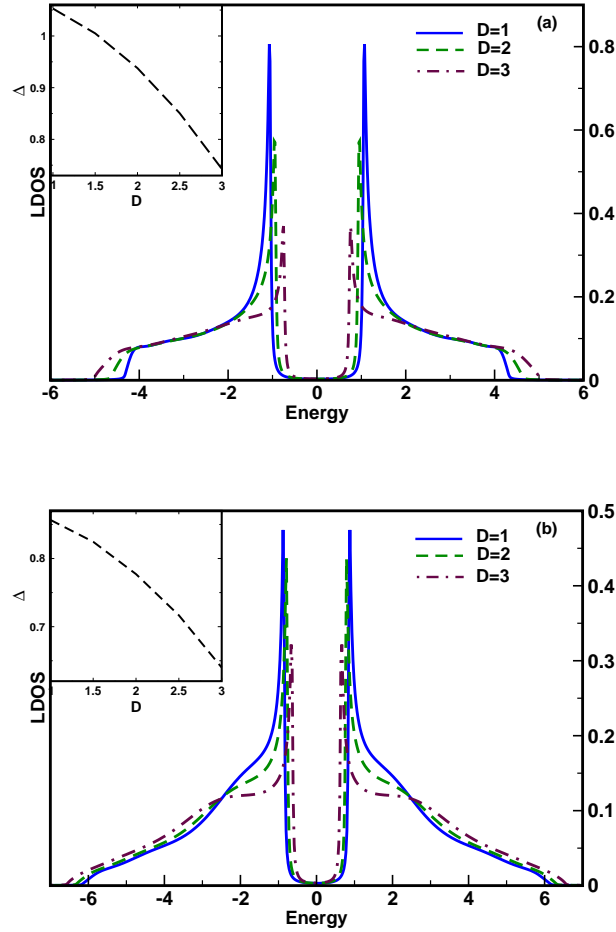
Figure 6.1: Local DOS for (a) square lattice and (b) cubic lattice with local interaction $U_{ii} = -3.5$. The system is homogeneously disordered with the strengths of disorder D =1, 2 and 3. The insets exhibit the variation of Δ with increasing D for the respective lattices.

6.3   Superconducting alloys with disorder in on-site energy

First we have studied the case of s-wave superconductivity where $|U_{ij}|$ is set to zero in the Hamiltonian and the local interaction U_{ii} is taken to be -3.5. We studied the half-filled 2-d square lattice and 3-d cubic lattice systems for different strengths of disorder D. The concentration x=0.5 and y=0.5 was chosen in our calculations. The results of our calculation is displayed in Fig.6.1. Our systems have homogeneous disorder with D=1, 2 and 3. With increasing disorder the LDOS that pile up at the internal gap edges decreases and states are pushed to higher energies. This observation was also made in a previous study [Ghoshal *et.al.* 1998] where randomness in the on site energy was described by an independent, continuous random variable V_i uniformly distributed over $[-V, V]$, at each site i. For both the square and cubic lattices we find that when the strength of disorder D is increased, superconductivity survives but the zero temperature pairing amplitude reduces (See inset Fig.6.1). This observation is supported by earlier studies [Goldman and Markovic 1998, Ghoshal *et.al.* 1998, Ghoshal *et.al.* 2001, Moradian *et.al.* 2000].

Having thus far kept the system fixed at half-filling, we now investigate the behaviour of zero temperature pairing amplitude (Δ) as we vary the filling fraction from 0 (empty band) to 2 (fully occupied band). For square and cubic lattices, as seen from Fig.6.2, Δ is maximum at half-filling and decreases as we move away from half-filling. The result of our calculation is similar to that obtained in CPA [Moradian *et.al.* 2000] . We gather from Fig.6.2 that Δ is maximum for the particle hole symmetric case when n=1 and $x=y$=0.5, as the order parameter fluctuation vanishes in this regime and the Anderson's theorem holds good irrespective of the strength of disorder. When the filling fraction (particle number) is either 0 or 2 then the coupling between the particle and hole space is not possible resulting in $\Delta = 0$ as can be seen in Fig.6.2.

We also studied the effect of disorder in ε_i on d-wave superconductivity. For this we set local interaction potential $U_{ii} = 0$ and the non-local interaction potential $U_{ij} \neq 0$. Now $\Delta_{ii} = 0$ and $\mu_i^* = \mu$ in Eqn (6.4). The results that we get for the 2d case is in good agreement with earlier works [McElroy *et.al.* 2005, Cheng and Su 2005, Martin *et.al.* 1999]. As seen from Fig.6.3 the behaviour of d-wave superconducting systems under disorder is distinctly different from that of s-wave superconductors. Here strikingly the
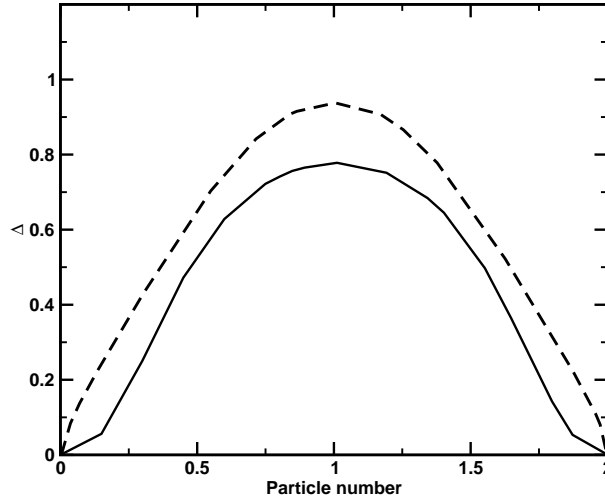
Figure 6.2: Zero temperature pairing amplitude (Δ) for (dashed line) square lattice and (solid line) a cubic lattice with D=2 as a function of filling fraction.

characteristic V-like dip that is the hallmark of non-random d-wave superconductivity (Fig.6.3) closes up, i.e. the density of states becomes non-zero with the introduction of even the slightest of disorder. This is a signature of gapless superconductivity in contrast to the gapped one in the s-wave case.

6.4   Random negative U Hubbard model

In this section we shall consider the attractive Hubbard model with a random on-site interaction term where a fraction of the sites occupied by A type of atoms have finite pairing potentials $U_{ii} = U^A \neq 0$ while others occupied by B type of atoms have zero pairing potentials $U_{ii} = U^B = 0$. For such a model we shall address the question whether there is a critical concentration x_0 of A atoms below which the system ceases to be superconducting.

The Hamiltonian under these conditions in the augmented space is:

$$\widetilde{\mathbf{H}}_{\text{eff}} = -\sum_{i \neq j, \sigma} t \; c_{i\sigma}^{\dagger} c_{j\sigma} + \sum_{i\sigma} \left(\ll\!\varepsilon\!\gg -\mu \right) \; n_{i\sigma} \ldots$$
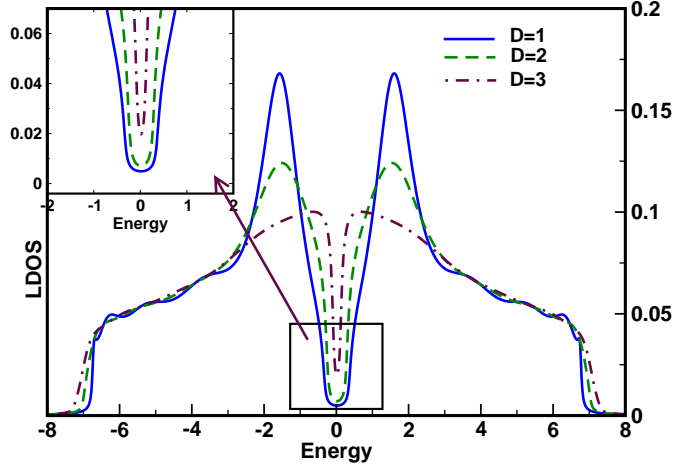
Figure 6.3: Local DOS for a 2d lattice with non-local interaction $U_{ij} = -3.5$. Here strength of disorder (D) is 0 (a) and 1,2,3 and 4 (b). The inset takes a closer view at the closing up of the V-like wedge in the DOS with increasing D.

$$+ \quad \sum_{i\sigma} \left(\delta\varepsilon - \delta\mu_i \right) \left\{ (y-x) \, \gamma_i^\dagger \gamma_i + \sqrt{xy} \, \left(\gamma_i^\dagger + \gamma_i \right) \right\} n_{i\sigma} \dots$$
$$+ \quad \sum_i \left(\delta\Delta_{ii} \, c_{i\uparrow}^\dagger c_{i\downarrow}^\dagger - \delta\Delta_{ii}^* \, c_{i\uparrow} c_{i\downarrow} \right) \left\{ (y-x) \, \gamma_i^\dagger \gamma_i + \sqrt{xy} \, \left(\gamma_i^\dagger + \gamma_i \right) \right\}$$

$$(6.20)$$

where: $\delta\varepsilon = \varepsilon^A - \varepsilon^B$, $\delta\mu_i = -|U^A| <n_i>/2$ and $\delta\Delta_{ii} = -|U^A| < c_{i\downarrow} c_{i\uparrow} >$.

In the augmented space, we see the effect of randomness in U_{ii} in two terms : $\delta\mu_i$ which is diagonal in particle-hole space and $\delta\Delta_{ii}$ which is off-diagonal in it [3].

We carried out a systematic study of the behaviour of zero temperature pairing amplitude (Δ) as a function of concentration, x, of such negative U centers for different values of pairing potential (U_{ii}) to investigate the variation of the critical concentration below which the system ceases to be a superconductor. As seen from Fig.6.4, the critical concentration necessary for the system to be superconducting increases with the decreasing value of the attractive interaction U seen as a sharp drop in Δ in Fig.6.4. In addition, for a given U with introduction of disorder in ε_i as well, the superconductivity is further

---

[3]By off-diagonal term arising from the randomness in U_{ii} we mean a term off-diagonal in the particle-hole and *not* off-diagonal in lattice space.
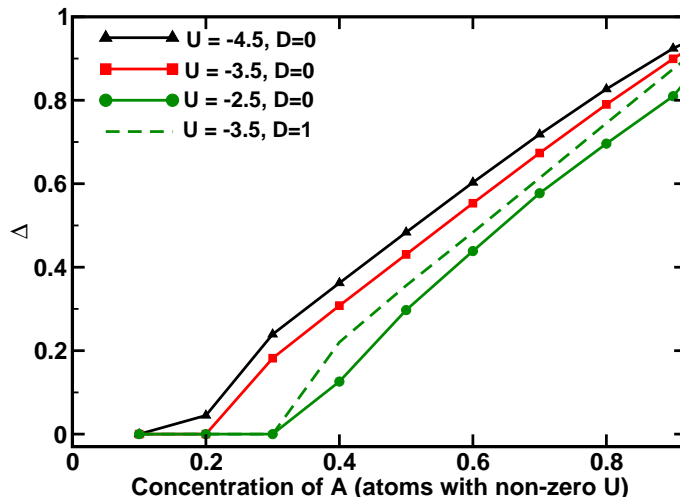
Figure 6.4: Zero temperature pairing amplitude (Δ) for the square lattice with randomness in U_{ii} as a function of concentration of atoms with non-zero pairing potential. Only for the dashed curve disorder strength D=1.

suppressed and a larger concentration of A atoms with non-zero U value are necessary for the system to be superconducting. Such critical concentration was also determined through CPA calculations [Litak and Györffy 2000].

We also did a comparative study of two type of systems. The first type (Type-1) is one where all the sites of the system have the same pairing potential U (a uniform system) and the second (Type-2) where 50 % of the sites have pairing potential $2U$ and others have pairing potential 0 (so that on the average $\ll U \gg$ is same in both the systems). The results are illustrated in Fig.6.5.

We see that when the strength of disorder (D) in ε_i is zero, and both diagonal and off-diagonal effects of disorder in U_{ii} (D=0, $\delta\mu$ and $\delta\Delta \neq 0$) is taken into account the superconducting order parameter Δ is larger for Type-2 in comparison to the uniform case (Type-1), particularly for the small value of the interaction strength. This observation was also made by an earlier work done through Monte Carlo (MC) simulations [Aryanpour *et.al.* 2006] and is attributed to the proximity effects where a finite superconducting order parameter may be realized even on non-interacting sites due to the tunneling of the Cooper
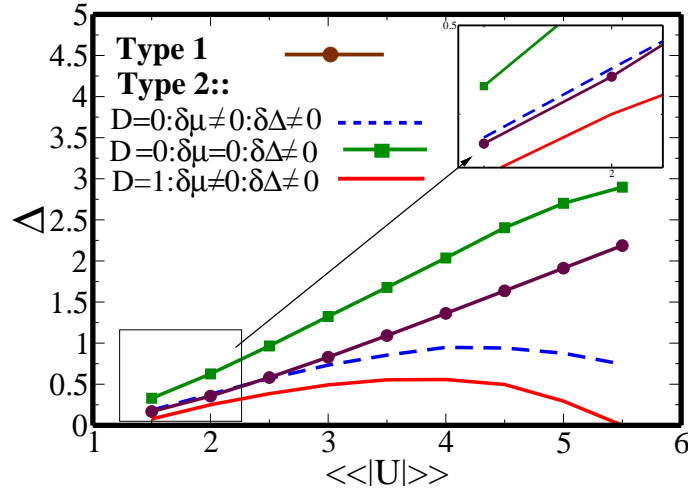
Figure 6.5: Study of pairing amplitude Δ as a function of average U. Here $\delta\mu$ is the diagonal term arising from disorder in U_{ii}. D and $\delta\Delta$ indicates disorder in ε_i and Δ_{ii} respectively. The strength of disorder in ε_i, $D=1$, wherever present. The inset takes a closer view at the behaviour of Δ_{ii} at low U_{ii}.

pairs from the interacting sites. This effect is particularly important at weak coupling (small U or Δ) where the coherence length $\xi = \frac{\hbar v_f}{\pi \Delta}$ is large.

Next we have gone further and investigated, the role of the particular terms in the Hamiltonian (6.20) that produces this behaviour. To do this (as seen from Fig.6.5) we first studied the sole effect of the term, off-diagonal in electron-hole space, arising from randomness in U_{ii} on the system (D=0, $\delta\mu = 0$ but $\delta\Delta \neq 0$). This term causes Δ to increase with increase in U_{ii} and is particularly prominent for small values of U. This is because at lower U_{ii} the coherence length is longer, thus tunneling of Cooper pairs from interacting to non-interacting sites is possible as we have argued earlier. On the other hand, the term diagonal in electron-hole space, arising from this randomness ($\delta\mu$) plays a role much like $\delta\varepsilon$ in reducing Δ. So it is the competition between the terms diagonal and off-diagonal in electron-hole space that arise from randomness in U_{ii} ($\delta\mu$ and $\delta\Delta$ respectively) which determines the behaviour of Δ. Since at lower U_{ii} tunneling of Cooper pairs is facilitated thus in this region the effect of the off-diagonal term ($\delta\Delta$) in enhancing Δ is more dominant. For non-zero on-site disorder D ($D = 1$), the superconducting order parameter Δ is further suppressed.

6.5   Superconducting alloys with correlated disorder

Instead of homogeneous disorder if there is short-ranged configuration correlations in the system, then the single-site CPA is unable to describe the situation adequately. We can use the generalized augmented space method introduced by Mookerjee and Prasad [Mookerjee and Prasad1993]. The method has been described in great detail in [Mookerjee and Prasad1993] and here we shall introduce only those essential ideas which are necessary for our exposition.

To start with, let us assume that short-range order (SRO) extends up to first nearest-neighbor only. For a square lattice the nearest neighbour cluster is shown in Fig. 6.6. Let us consider a site labeled 0 (shown as a dark sphere) and the occupation variable associated with this site n_0.
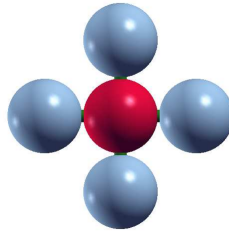
Figure 6.6: An central atom at a site 0 of a square lattice associated with its four nearest neighbours at 1-4

The occupation variables associated with its four nearest neighbours, n_k $(k = 1 \ldots 4)$ are correlated with n_0 but not with one another. Further none of the other occupation variables associated with more distant sites are correlated with n_0. We may then write the joint probability density as

$$P(\{n_m)\}) = P(n_0) \prod_{k=1}^{4} P(n_k|n_0) \prod_{m>4} P(n_m)$$

The generalized augmented space theorem also associates with the random variable n_k a corresponding operator $\widetilde{N_k}$ in augmented space. The construction of that operator has been discussed in detail in the paper [Mookerjee and Prasad1993]. We can characterize

short-ranged order by a Warren-Cowley parameter $\alpha(R) = 1 - P_{AB}(R)/x$, where x is the concentration of A-type of atom and $P_{AB}(R)$ is the probability of finding a B atom at a distance R from an A atom. Using this α, the conditional probabilities are given by

For $k = 0$ and $k > 4$

$$P(n_k) = x\delta(n_k - 1) + y\delta(n_k) \tag{6.21}$$

For $1 \leq k \leq 4$

$$P(n_k|n_0 = 1) = (x + \alpha y)\delta(n_k - 1) + (1 - \alpha)y\delta(n_k)$$
$$P(n_k|n_0 = 0) = (1 - \alpha)x\delta(n_k - 1) + (y + \alpha x)\delta(n_k)$$

$$\tag{6.22}$$

We note that when $\alpha = 0$ there is no SRO in the system and the conditional probabilities for n_k when $1 \leq k \leq 4$ reduces to the unrestricted probability for n_k when $k = 0$ and $k > 4$. While $\alpha < 0$ indicates a tendency towards ordering, $\alpha > 0$ indicates a tendency towards phase segregation.

In the full augmented space, the operators which replace the occupation variables are the same as Eqn. (6.14) for the site 0 and its far environment. However, for its nearest neighbours $k = 1 - 4$:

$$
\begin{aligned}
\widetilde{N_k} &= x + (y - x)\,\gamma_k^\dagger\gamma_k + \alpha(y - x)\,\gamma_0^\dagger\gamma_0 - 2\alpha(y - x)\,\gamma_k^\dagger\gamma_k\gamma_0^\dagger\gamma_0 + B_1\left(\gamma_k + \gamma_k^\dagger\right)\ldots \\
&\quad + B_3\left(\gamma_0 + \gamma_0^\dagger\right) + (B_2 - B_1)\,\gamma_0^\dagger\gamma_0\left(\gamma_k + \gamma_k^\dagger\right) + (B_4 - B_3)\,\gamma_k^\dagger\gamma_k\left(\gamma_0 + \gamma_0^\dagger\right)\ldots \\
&\quad + B_5\left(\gamma_k + \gamma_k^\dagger\right)\left(\gamma_0 + \gamma_0^\dagger\right)
\end{aligned}
\tag{6.23}
$$

where,

$$
\begin{aligned}
B_1 &= x\sqrt{(1-\alpha)y(x+\alpha y)} + y\sqrt{(1-\alpha)x(y+\alpha x)} \\
B_2 &= y\sqrt{(1-\alpha)y(x+\alpha y)} + x\sqrt{(1-\alpha)x(y+\alpha x)} \\
B_3 &= \alpha\sqrt{xy} = -B_4 \\
B_5 &= \sqrt{xy}\left[\sqrt{(1-\alpha)y(x+\alpha y)} - \sqrt{(1-\alpha)x(y+\alpha x)}\right]
\end{aligned}
$$

We note that as $\alpha \to 0$ the above equation is reduced to Eqn. (6.14).

We now follow the augmented space theorem and replace all the occupation variables $\{n_m\}$ by their corresponding operators. The configuration average is the specific matrix element between the *reference* state $|\{\emptyset\}\rangle$ as discussed earlier. We also note that the choice of the *central* site labeled 0 is immaterial. If we translate this site to any other and apply the lattice translation to all the sites, the Hamiltonian in the full augmented space remains unchanged. This formulation of SRO also possesses lattice translational symmetry, provided the short-range order is homogeneous in space, as we consider it to be in our present study.

We investigate the behaviour of a system with random U_{ii} where *only* the term off-diagonal in electron-hole space, arising from the disorder in U_{ii}, is considered. When we introduce short-ranged order in the system we observe that the effect of randomness in U_{ii} to be quite different from randomness in ε_i. For randomness in U_{ii}, ordering supports superconductivity. This is because ordering favors tunneling of Cooper pairs from the interacting to the non-interacting sites (now the non-interacting and interacting sites are near-neighbours of each other). Thus even the non-interacting sites develop finite value of Δ_{ii}, resulting in a larger value of the zero temperature pairing amplitude as compared to phase segregation.

6.6   Effect of Off-diagonal Randomness on Superconductivity

In order to illustrate our numerical method and the importance of the off-diagonal disorder the calculations are carried out for two different choices of parameters:

Type 1 The parameters κ, β and Γ are chosen in such a way so that the constraint $\kappa + \beta - 2\Gamma = 0$ is satisfied. As mentioned earlier this choice of the parameters exclude correlated simultaneous configuration fluctuation at two sites. Here $\delta = \kappa - \beta$ is the parameter that characterize the strength of the off-diagonal disorder.

Type 2 One in which $\kappa + \beta - 2\Gamma \neq 0$. Here the parameter $\kappa + \beta - 2\Gamma$ define the strength of off-diagonal disorder.

Further for the ease of discussion of the disorder of Type 2, we define a parameter $\chi = (\kappa - \Gamma) + (\beta - \Gamma)$ such that when:

(i) $\chi > 0 \rightarrow$ strength of hopping interaction between same kind of species is greater than that between different kind of species.

(ii) $\chi = 0 \rightarrow$ strength of hopping interaction between same kind of species is equal to that between different kind of species.

(iii) $\chi < 0 \rightarrow$ strength of hopping interaction between same kind of species is less than that between different kind of species.

Finally Table6.1 presents a correspondence between the chosen parameters defined in the methodology section and the various figures discussed in the present section.

6.6.1   Normal systems with randomness in the off-diagonal hopping term t_{ij}

We shall first present test calculations for non-superconducting systems $(U_{ii} = U_{ij}=0)$ for a two dimensional *(square lattice)* tight-binding model with disorder in the hopping term t_{ij} in order to check the feasibility and numerical accuracy of our method. The composition of the alloys is taken to be $x=y=0.5$ and the system is fixed at half-filling throughout the present analysis. The off-diagonal disorder is characterized by three parameters t^{AA}, t^{BB} and t^{AB}, where we have defined $t^{AA} = \kappa t$; $t^{BB} = \beta t$ and $t^{AB} = \Gamma t$. We have kept $\ll t_{ij} \gg = x * t^{AA} + y * t^{BB}$ fixed at 1 in units of t.

The results of our calculation for the configuration averaged local density of states are displayed in Figure 1. The type of disorder (reflected by the type of parameters) depicted by each figure is described in Table6.1. In Figs. 6.7(a) and (b) we have kept Γ constant and have varied $\delta = \kappa - \beta$ such that $\chi = \kappa + \beta - 2\Gamma = 0$. Thus disorder is of Type 1. We find from Fig. 6.7(a) that with the increase in off-diagonal disorder δ, the width of the energy spectrum *increases* due to disorder induced broadening. States pile up at the band centre and DOS at the Fermi level increases for larger values of δ. The widening

Table 6.1: Correspondence between parameters defined in the Methodology section and the various figures discussed here. $\sqrt{}$ $\rightarrow$ The corresponding potential parameter is present in the Hamiltonian and is random. $\times$ $\rightarrow$ The corresponding potential parameter is present in the Hamiltonian but is not considered to be random. — $\rightarrow$ The corresponding potential parameter is not present in the Hamiltonian. "$*$" :: $t^{AA}{=}t^{BB}$, [since here $\delta = t^{AA} - t^{BB}$, the random off-diagonal potential parameter in question being t_{ij}] so the widths of the bands for the A and B species are the same.

ϵ	t_{ij}	U_{ii} (Δ_{ii})	U_{ij} (Δ_{ij})	TYPE	Figures (in Section 3)
$\times$	$\sqrt{}$	—	—	1	FIG 6.7 a)
$\sqrt{}$	$\sqrt{}$	—	—	1	FIG 6.7 b)
$\times$	$\sqrt{}$	—	—	2	FIG 6.7 c)
$\sqrt{}$	$\sqrt{}$	—	—	2	FIG 6.7 d)
$\sqrt{}$	$\sqrt{}$	—	—	2	FIG 6.7 e)
				(with $\delta{=}0$)*	
$\times$	$\sqrt{}$	$\times$	—	1	FIG 6.8a)
$\sqrt{}$	$\sqrt{}$	$\times$	—	1	FIG 6.8b)
$\times$	$\sqrt{}$	$\times$	—	2	FIG 6.8c)
$\sqrt{}$	$\sqrt{}$	$\times$	—	2	FIG 6.8d)
$\sqrt{}$	$\sqrt{}$	$\times$	—	2	FIG 6.8e)
				(with $\delta{=}0$)*	
$\times$	$\sqrt{}$	—	$\times$	1	FIG 6.10

of the band width and enhancement of the central maximum leads to a decrease in the kurtosis of the DOS shape. With the additional presence of on-site disorder ($D{=}0.5$), the DOS becomes asymmetric [Fig. 6.7(b)].

Now, we consider disorder of Type 2 as discussed earlier, and the results are presented in Fig. 6.7(c). In Fig. 6.7(c), $\Gamma{=}0.8$, 1 and 1.2 corresponds to $\chi > 0$, $\chi = 0$ and $\chi < 0$ respectively. From this figure we see that as we go from $\chi > 0$ to $\chi < 0$ the band-width hardly changes but the weight of the DOS at the Fermi level decreases. As in the earlier case, inclusion of the on-site disorder D along with the off-diagonal disorder δ leads to asymmetry in the DOS [Fig .6.7(d)]. The reason may be attributed to the individual DOS of the A and B species having different band widths ($t^{AA} \neq t^{BB}$, since $\delta \neq 0$). The presence of the diagonal disorder causes the individual DOS of the two species to
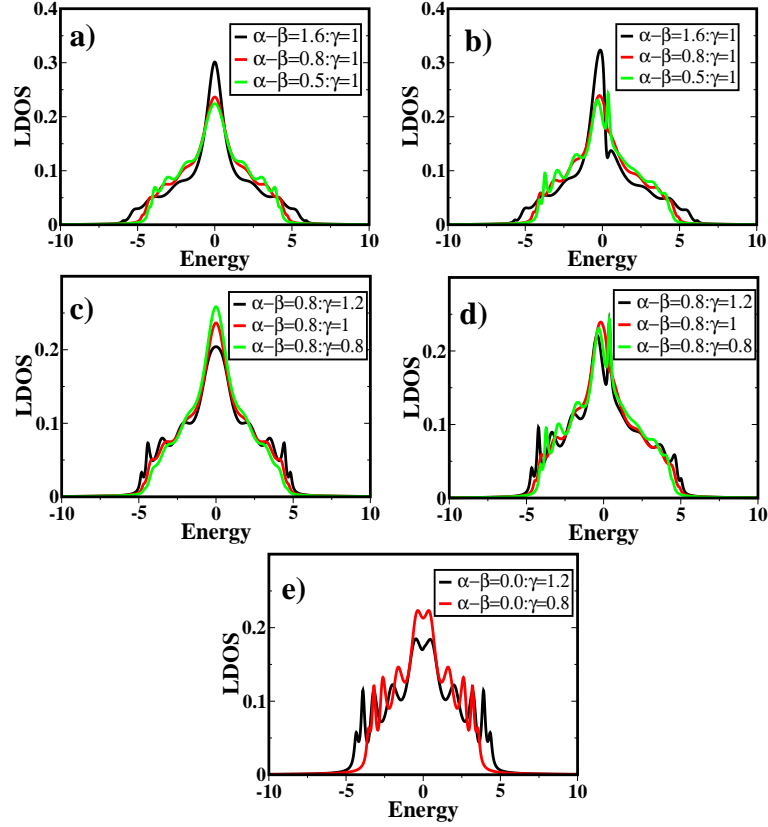
Figure 6.7: A study of the variation of the normal state DOS with $(\kappa - \beta)$ [(a)] and Γ [(c)]. The presence of randomness simultaneously in diagonal(ϵ_i) as well as off-diagonal (t_{ij}) terms make even the normal state DOS asymmetric provided $(\kappa - \beta) \neq 0.0$ [(b) and (d)]. But when $(\kappa - \beta) = 0.0$ then the DOS remains symmetric even when diagonal and off-diagonal randomness are present simultaneously [(e)].

be centre-shifted (since $\epsilon_A \neq \epsilon_B$) resulting in the combined DOS being asymmetric. We have verified this by choosing D=0.5, but $\delta = 0$, $\Gamma \neq 0$. The results are shown in Fig. 6.7(e), where in spite of the presence of both diagonal and off-diagonal disorder the DOS of the binary substitutional alloy remains symmetric, since the widths of both the A and B species remain the same and their partial DOS is centre-shifted. Thus simultaneous presence of randomness in diagonal and off-diagonal terms of the Hamiltonian causes asymmetry of the DOS of a binary substitutional alloy only under the special condition, $\delta \neq 0$ i.e. the widths of the individual DOS of the component species are unequal.
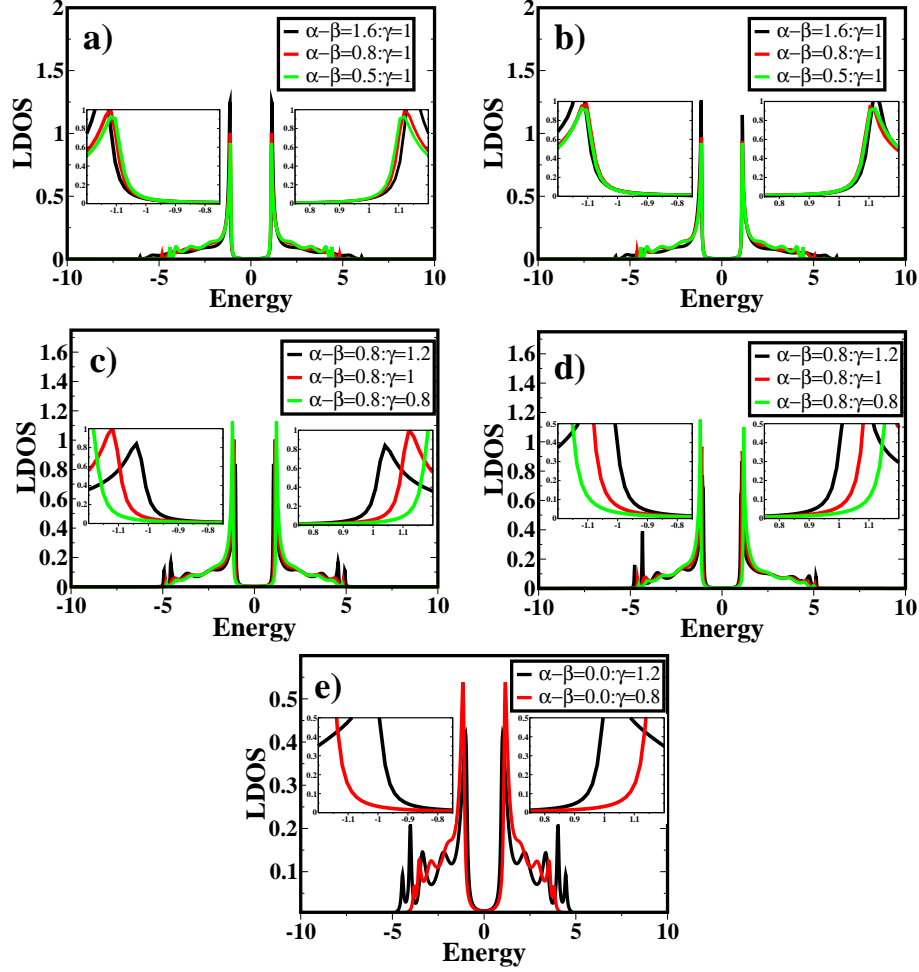
Figure 6.8: s-wave superconductivity in the presence of off-diagonal disorder. While (a) and (b) are studies of the DOS of the system with increasing value of disorder parameter δ with and without diagonal randomness respectively, (c) and (d) are corresponding studies of the effect of off-diagonal disorder parameter χ. For definitions of δ and χ the text may be referred. The presence of randomness simultaneously in diagonal(ϵ_i) as well as off-diagonal (t_{ij}) terms make the DOS asymmetric provided $(\kappa - \beta) \neq 0.0$ [(b) and (d)]. But when $(\kappa - \beta) = 0.0$ then the DOS remains symmetric even when diagonal and off-diagonal randomness are present simultaneously [(e)]

Finally we would like to comment on the fine structure observed in the various graphs of Fig. 6.7 and all subsequent figures on the density of states. It has been known for a long time that, in low dimensions, the exact averaged density of states has considerable fine structure, particularly near the band edges. Numerical works on one-dimensional disordered chains with diagonal disorder by Dean [Dean 1959-Dean 1961] clearly showed the existence of such structures. It was also clear that such structures are not reproduced by the single site coherent potential approximation. Foo *et al* [Foo *et.al.* 1971] showed that in linear chains with off-diagonal disorder as well, such fine structures were seen near the band edges and in impurity bands. They argued that these arose mainly due to the random formation of clusters in a disordered background. Later Oguchi *et al* [Oguchi *et.al.* 1973] confirmed this in a disordered Heisenberg model (i.e. where the off-diagonal term is disordered). The ASR method allows us to take into account the effect of clusters. We have checked that the fine structure seen in our density of states is not due to effect of terminators. Modifying the length of the terminator or changing the parameter η in it hardly affects the structures. We propose therefore that the fine structures are due to random clustering effects. They are particularly prominent when $\kappa - \beta$ and Γ are very different leading to either AA,BB or AB clusters. Since our models are on a square lattice, the effects are much more prominent than in three dimensional lattices.

6.6.2 *s*-wave and *d*-wave superconductors with randomness in the off-diagonal hopping integral t_{ij}

We shall study the effect of disorder in the off-diagonal hopping integral t_{ij} on an *s*-wave superconductor. We shall keep $U_{ij} = 0$ and U_{ii} fixed at 3.5. As before, $\ll t_{ij} \gg$ is kept fixed at 1 in units of t.

The results are shown in Fig. 6.8(a). To understand the kind of disorder depicted by each figure one may refer to Table6.1.

In Figs. 6.8(a) and (b) we have kept Γ constant and have varied $\delta = \kappa - \beta$ such that $\chi = \kappa + \beta - 2\Gamma = 0$. Thus disorder is of Type 1.

We see from Fig. 6.8(a) that the magnitude of the gap in the DOS is nearly independent of the variation in δ implying that off-diagonal disorder of TYPE1 has hardly any

influence on s-wave superconductivity.

However, for Type 2 disorder shown in Fig. 6.8(c), as we go from $\chi > 0$ to $\chi < 0$ the DOS gets smeared (as also seen in the normal system) and the gap in the DOS decreases.

The variation of Δ with χ is seen more clearly in Fig. 6.9(a). *Here Δ is the local pairing amplitude Δ_{ii} described in Eqn(6.19) which is the order parameter for superconductivity.* Here we keep δ fixed and vary χ which as discussed previously is a measure of the difference in hopping strengths between similar and dissimilar sites. We see clearly from Fig. 6.9(a) that as χ is varied from the negative to the positive end, Δ increases showing greater hopping interaction strength between similar species supports and enhances superconductivity. Earlier in this chapter we had seen that phase segregation (similar species clustering together) enhances superconductivity more than AB ordering. This is consistent with our present finding. Our results clearly demonstrate that the gap in the quasi-particle spectrum survives even in the presence of the off-diagonal disorder and Anderson's theorem [Anderson 1959] remains valid.

The presence of diagonal disorder (D=0.5) along with the off-diagonal disorder (δ) makes the DOS asymmetric [Figs. 6.8(b) and (d)] similar to the non-superconducting systems. Here also the cause of asymmetry can be identified as different widths of constituent bands ($t_{AA} \neq t_{BB}$) combined with the fact that their centers do not coincide ($\epsilon_A \neq \epsilon_B$). This is confirmed by Fig. 6.8(e) where we again see if $t_{AA} = t_{BB}$ ($\delta = 0$) then in spite of the presence of both diagonal (D=0.5) and off-diagonal ($\chi \neq 0$) disorder the DOS of the system remains symmetric. Such disorder induced asymmetry of DOS may be relevant for the tunneling experiments done on $Ba_2Sr_2CaCuO_{8+\delta}$ [Renner *et.al.* 1998].

We have studied next the variation of the gap parameter Δ as a function of κ, where β and Γ are put equal to zero. In such a situation there is hopping of electron only from a site occupied by species A provided its nearest neighbour site is also occupied by A. As we see from (Fig. 6.9(b)) superconductivity does survive in the material, but with increase of κ, the pairing amplitude Δ decreases. This is because here $\delta = \kappa$ and as it increases it enhances the strength of off-diagonal disorder and therefore suppresses superconductivity.

Similarly for disordered d-wave superconductors (U_{ii}=0,$U_{ij} \neq 0$) we studied the effect
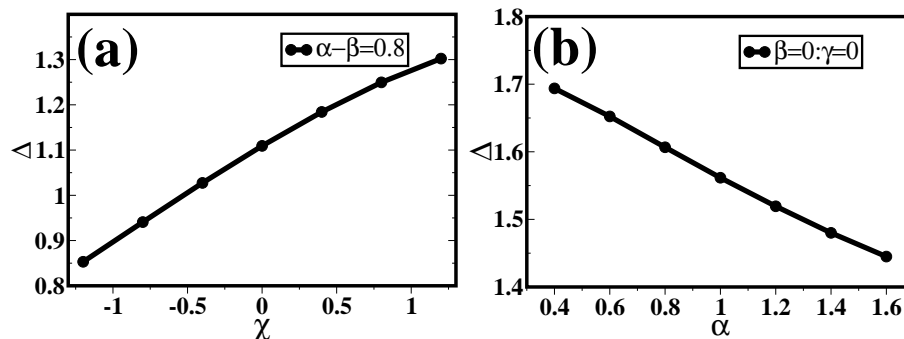
Figure 6.9: Variation of the superconducting gap with variation of the off-diagonal disorder parameter (a) χ, with $(\kappa - \beta)$ kept fixed at 0.8. (b) κ, with β and Γ kept at zero.

of randomness in the hopping integral t_{ij}. Here we keep $\ll t_{ij} \gg = 1$ as before. We study the DOS of the system with variation of δ (See Table6.1). We see, from Fig. 6.10, that similar to diagonal disorder for d-wave superconductivity [Godin and Haydock 1988, Godin and Haydock 1992], the off-diagonal disorder in t_{ij} also closes up the V-like dip in the DOS characteristic of non-random d-wave superconductors. The DOS at the band centre becomes non-zero even with the introduction of a slightest amount of disorder. This observation agrees with earlier CPA studies [Michalik and Wysokiński 2004, Michalik and Wysokiński 2006]. But unlike diagonal disorder parameter D, change in off-diagonal disorder parameter δ does not affect the gap in the DOS appreciably (see Fig. 6.10 - inset).

6.7 Summary

In this chapter we have proposed the augmented space vector recursion method as a very effective real space approach to study the effect of disorder on superconductivity beyond the mean-field approximation. We have established the accuracy of our method by comparing its results with those obtained by other techniques, for both s- and d-wave superconductors. We have seen that while for s-wave superconductors the gap in the
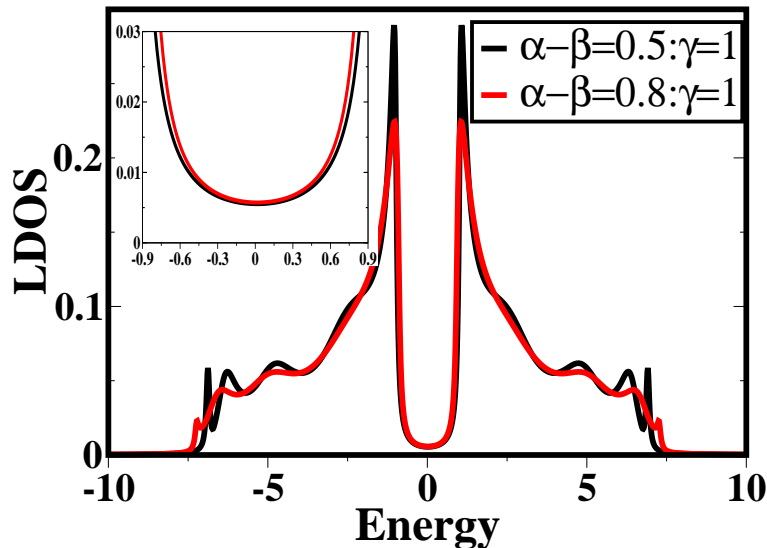
Figure 6.10: Density of states for d-wave superconductor in the presence of disorder in the hopping amplitude t_{ij}.

quasi-particle spectrum survives even in the presence of disorder, (the system being in the limit of validity of Anderson's theorem), for the exotic *d*-wave case it vanishes in the presence of slightest disorder. In addition, considering a system where electrons attract each other provided they are near certain centers, we see a critical number of such centers are necessary for superconductivity to survive in the system. Our results using the ASR method are in excellent agreement with that available in the literature.

Satisfied about the reliability of our method, we use it to study the effect of environment dependent randomness of various terms of the Hamiltonian. This would not have been possible using any single-site mean-field approximations like the CPA. For correlated disorder in ε_i segregation tendency support superconductivity while for a system where only some sites are interacting, ordering facilitates tunneling of Cooper pairs from interacting to non-interacting sites and thus favors superconductivity. However for higher value of the effective pair interaction potential U the coherence length falls off and such tunneling of Cooper pairs become difficult.

In the present chapter we have also applied the augmented space vector recursion

(ASVR) method to study the effect of randomness in the off-diagonal terms of the attractive Hubbard Hamiltonian on s- and d- wave superconductivity. For binary substitutional alloys we see that for s-wave superconductivity inclusion of correlated simultaneous configuration fluctuation at two sites ($\chi \neq 0$) has a strong influence on the superconducting gap which cannot be captured using methods involving single site approximation. It is in the ability to successfully deal with off-diagonal disorder that the strength of our technique (ASVR) is especially manifested. Further in the presence of off-diagonal disorder s-wave superconductivity is favoured by greater hopping integral strength between same kind of species as compared to that between different kinds. For d-wave superconductors randomness in t_{ij} causes gap-less superconductivity similar to the case when disorder is included in the diagonal terms. Combined diagonal and off-diagonal randomness causes asymmetry of DOS in both normal and superconducting binary substitutional alloys only when the band widths of the individual DOS of the A and B species are different.

The advantage as well as the strength of the recursion method is that it can easily be generalized to many band Hubbard models. This will be illustrated in the next chapter. Coupled with first principles techniques like the tight-binding linear muffin-tin orbital method, we can establish a methodology for the study of realistic materials.

Chapter 7

A study of multi-band superconductivity in binary disordered alloys using the augmented space recursion approach.

7.1 Introduction

In this chapter we will extend our methodology to study the effect of disorder on single band systems to analyze the effect of disorder on multi-band systems. We again use the augmented space formalism to handle disorder. In the ordered regime our results for both intra-band and inter-band pairing are in excellent agreement with the existing results. Having verified the reliability of our method we use it to investigate the survival of superconductivity in the presence of disorder in multi-band systems.

In the recent years study of superconductivity in multi-orbital systems received considerable interest due to the discovery of many superconducting materials where the Fermi surface is dominated by several bands. Experimentally, in 2001, superconductivity with T_c=39K was observed in MgB_2[Nagamatsu $et.al.$ 2001]. In MgB$_2$ the Fermi surface is determined by the σ and π bands arising from the B-p orbitals. It is now confirmed that the superconductivity in this material can be explained with the aid of BCS theory with two different superconducting gaps in agreement with experiments [Choi $et.al.$ 2002]. A description of unusual $p-$ wave superconductivity in strontium ruthenate also necessitates a multi-orbital model for superconductivity [Wysokinski $et.al.$ 2007, Annett $et.al.$ 2002]. Very recently the discovery of superconductivity in Fe pnictides where the Fermi surface is defined by the t_{2g} orbitals of Fe have again emphasized the importance of the study of

superconductivity in multi-band systems [Daghofer *et.al.* 2008, Raghu *et.al.* 2008].

The issue of superconductivity (SC) in multi-band systems was first studied by Suhl *et al.* [Suhl *et.al.* 1959] using a tight-binding model Hamiltonian with two bands. The model included intra-band pairing and also the inter-band tunnelling of pairs of electrons belonging to the same band. They showed that pairing could occur in each band and, because electron-phonon interactions may have different strengths in different bands, therefore this can give rise to two different superconducting gaps. But in the special case of only inter-band scattering a single gap was found to be present in the density of states unless the band structure of the two bands had different shapes [1]. A similar model was also investigated by Machida *et. al.* [Machida *et.al.* 2002] for the study of superconductivity in multi-band systems. Recently Moreo *et. al.* [Moreo *et.al.* 2009] revisited the theory of SC in multi-orbital system in the context of Fe pnictides. In particular they have emphasized the importance of inter-band pairing in multi-orbital systems where in contrast to earlier studies [Suhl *et.al.* 1959, Machida *et.al.* 2002] Cooper pairs are formed by electrons belonging to two different bands. The calculations by Moreo *et. al.* [Moreo *et.al.* 2009] revealed that three different regions can result from a purely inter-band pairing as a function of the interaction parameter: (1) a normal regime where the ground state is not superconducting ; (2) an exotic superconducting "breached" regime where one of the bands is gapped at the Fermi level while the other is not, and (3) a superconducting regime resembling the BCS states, at large attractive coupling.

The preceding discussion suggests that superconductivity in multi-orbital system is not only interesting but markedly different from its single band counterpart. In this context it will also be important to understand the role of disorder in multi-band superconducting system as disorder is an important parameter that has profound impact on superconductivity. While the effect of disorder on superconductivity in single band system have been actively investigated but there is hardly any systematic study on the role of disorder in multi-band systems. Some experimental studies done on MgB_2 [Xu *et.al.* 2001] with substitution of nonmagnetic $[(Mg_{1-x}Zn_x)B_2]$ and magnetic $[(Mg_{1-x}Mn_x)B_2]$ impurities show that though the transition temperature T_c drops sharply for magnetic

---

[1] The shape of a band is determined by the diagonal and the hopping matrix elements of the corresponding tight-binding Hamiltonian.

impurity with increasing x, it is unaffected by nonmagnetic impurity. But for $LuFe_3Si_5$ compound substitutional disorder with both magnetic and nonmagnetic impurities causes sharp drop in T_c [Watanabe *et.al.* 2009]. The effect of disorder in single band systems is usually discussed in the framework of Anderson's theorem [Anderson 1959]. For *s*-wave superconductors Anderson's theorem guarantees the survival of an absolute gap in the quasi-particle spectrum of the system provided the perturbation due to disorder preserves time reversal invariance and the coherence length is long enough to ensure that the pairing amplitude Δ does not fluctuate. There exists quite a large body of work where the Bogoliubov-de Gennes (BdG) equations [de Gennes 1966] which provide a natural framework for a fully microscopic description of the phenomena of supercondutivity have been solved [Moradian *et.al.* 2000, Martin *et.al.* 1999, Litak and Györffy 2000] in conjunction with the mean-field single-site coherent potential approximation (CPA) in order to understand the physics of superconductivity in single-band disordered systems.

In the last chapter we have proposed an efficient scheme to solve BdG equations for single band disordered attractive Hubbard model. The aim of the present chapter is to propose a real-space, vector recursion based approach to study the effect of disorder on a multi-band attractive-U Hubbard model where the configuration averaging like our earlier study will be based on the augmented space recursion (ASR) formalism introduced by one of us [Mookerjee 2003]. The ASR gives us the flexibility of introducing the effects of random configuration fluctuations in the local environment of a site. It does not violate analytical properties of the configuration-averaged Green's function, which form an essential ingredient of the solution. It can deal easily with the effect of either off-diagonal disorder or inhomogeneous disorder such as clustering, segregation, and short-ranged order which usually occur intrinsically in most disordered materials due to different chemical affinities of the constituents.

We shall begin by studying superconductivity in multi-band ordered systems using our vector recursion technique in a two-band, tight-binding, attractive-U Hubbard model. Then, having satisfied ourselves with the reliability of our methodology, we shall proceed to study the effect of disorder on the system again in a tight-binding attractive U Hubbard model for a two band system. In particular, we shall consider a model where disorder is introduced in one of the bands and study its effect on the other. The remaining of

the chapter is organized as follows, in Section 7.2 we shall discuss our method in some details and Section 7.3 will be devoted to results and discussions for multiband ordered and disordered systems. Finally in Section 7.4 we will summarize our study.

7.2   Methodology

7.2.1   The multi-band attractive-U Hubbard model

To study the effect of disorder on a multi-band s-wave superconducting system we shall begin with the simplest model, namely, the two band attractive Hubbard Hamiltonian in model lattices. The Hamiltonian is given by :

$$
\begin{aligned}
\mathbf{H} \;=\; & -\sum_{\langle i,j\rangle}\sum_{m,m',\sigma} t_{im,jm'}\,c^{\dagger}_{im\sigma}c_{jm'\sigma} + \sum_{i,m,\sigma}(\epsilon_{im}-\mu)\,n_{im\sigma} \\
& -\sum_{i,m}|U_{mm}(i)|\,n_{im\uparrow}n_{im\downarrow} - \sum_{i}\sum_{m,m',\sigma,\sigma'}|U_{mm'}(i)|\,n_{im\sigma}n_{im'\sigma'}
\end{aligned}
\tag{7.1}
$$

This Hamiltonian is a generalization of the single-band Hubbard Hamiltonian and similar to earlier studies by Annett *et al.* [Wysokinski *et.al.* 2007, Annett *et.al.* 2002]. Our model Hamiltonian allows for both intra-band as well as inter-band pairing. The inter-band pairing term is similar to that of Annett *etal* [Wysokinski *et.al.* 2007, Annett *et.al.* 2002] and Moreo *etal* [Moreo *et.al.* 2009] which allows for the Cooper pairs formed by electrons belonging to two different bands. The earlier studies by Suhl *etal* [Suhl *et.al.* 1959] and Machida *etal* [Machida *et.al.* 2002] did not consider the pairing of electrons belonging to two different bands but a pair tunnelling term given by::

$$
-\sum_{i}\sum_{m,m',\sigma,\sigma'}|U^{t}_{mm'}(i)|\,(c_{im\sigma}c_{im\sigma'})^{\dagger}c_{im'\sigma}c_{im'\sigma'}
\tag{7.2}
$$

that allowed for the tunneling of the Cooper pairs from one band to the other. The tunnelling strength is given by $U^{t}_{mm'}$.

In Eqn.(7.1), $\{c^{\dagger}_{im\sigma}, c_{im\sigma}\}$ are the usual electron creation and annihilation operators for orbital m with spin σ on site labeled i of a square or simple-cubic lattice. Here the

index m runs over the two bands labeled s- and l-. The local charge density operator for orbital m is $n_{im} = n_{im\uparrow} + n_{im\downarrow}$, where $n_{im\sigma} = c_{im\sigma}^{\dagger}c_{im\sigma}$; μ is the chemical potential and ε_{im} the local on-site energy at the site labeled i and band m. The hopping integral $t_{im,jm'}$ has four components:: $t_{is,js} = t_s$ is the hopping integral in the s-band from a site i to one of its nearest neighbours j and $t_{il,jl} = t_l$ is that in the l-band form a site to one of its nearest neighbours. The inter-band hopping integrals are $t_{is,il} = t_{sl}$ which is the hopping integral from a site in the s-band to the same site in the l-band (or vice-versa) and $t_{is,jl} = t_{sl}^{nn}$ which is the hopping integral from the a site i in the s-band to one of its nearest neighbours j in the l-band (or vice-versa). In this work we have not included the inter-band inter-site hopping integral t_{sl}^{nn}. However, we do consider the effect of on-site inter-band hopping integrals t_{sl} in some of our analysis. As we will see subsequently, t_{sl} will not alter the qualitative features of our results. In this model, $U_{mm}=-|U_s|$ corresponds to a local Hubbard parameter leading to a pairing interaction potential for s-band electrons and $U_{mm}=-|U_l|$ correspond to a local Hubbard parameter for l-band electrons. Here, both the attractive interactions give rise to s-wave pairing since they are local. The inter-band pairing interaction $U_{mm'}=-|U_{sl}|$ is the local attractive potential between electrons in the s- and l- band.

The BdG mean field decomposition [de Gennes 1966] of the interaction terms give expectation values to the intra and inter band pairing amplitudes:

$$
\begin{aligned}
\Delta_s &= -|U_s| \langle c_{is\downarrow}c_{is\uparrow}\rangle \\
\Delta_l &= -|U_l| \langle c_{il\downarrow}c_{il\uparrow}\rangle \\
\Delta_{sl} &= -|U_{sl}| \langle c_{il\downarrow}c_{is\uparrow}\rangle
\end{aligned}
\tag{7.3}
$$

and also to the intra and inter band *"densities"*:

$$
\begin{aligned}
\langle n_{is\sigma}\rangle &= \langle c_{is\sigma}c_{is\sigma}^{\dagger}\rangle \\
\langle n_{il\sigma}\rangle &= \langle c_{il\sigma}c_{il\sigma}^{\dagger}\rangle \\
\langle n_{isl\sigma}\rangle &= \langle c_{il\sigma}c_{is\sigma}^{\dagger}\rangle
\end{aligned}
\tag{7.4}
$$

The effective quadratic BdG Hamiltonian becomes :

$$
\mathbf{H}_{\text{eff}} = -\sum_{\langle i,j\rangle}\sum_{m,m',\sigma} t_{im,jm'}\, c_{im\sigma}^{\dagger}c_{jm'\sigma} + \sum_{im\sigma}(\varepsilon_{im} - \mu_{im}^{*})\, n_{im\sigma}\ldots
$$

$$-\frac{1}{2} \sum_{im,m',\sigma} |U_{mm'}| \langle n_{imm'\sigma} \rangle \; c^\dagger_{im\sigma} c_{jm'\sigma} + \sum_{im} \left(\Delta_m c^\dagger_{im\uparrow} c^\dagger_{im\downarrow} - \Delta^*_m c_{im\uparrow} c_{im\downarrow} \right) \ldots$$

$$+ \sum_{i,m,m'} \left(\Delta_{mm'} c^\dagger_{im\uparrow} c^\dagger_{im'\downarrow} - \Delta^*_{mm'} c_{im\uparrow} c_{im'\downarrow} \right) \tag{7.5}$$

where $\mu^*_{im} = \mu - |U_{mm}| \langle n_{im} \rangle / 2$ incorporates the site dependent Hartree shift.

This effective Hamiltonian can be diagonalized by using the Hartree-Fock-Bogoliubov (HFB)[Satpathy *et.al.* 1969] transformation:

$$
\begin{aligned}
c_{im\uparrow} &= \sum_n [\beta_{n\uparrow} u_m(r_i, E) - \beta^\dagger_{n\downarrow} v^*_m(r_i, E)] \\
c_{im\downarrow} &= \sum_n [\beta_{n\downarrow} u_m(r_i, E) + \beta^\dagger_{n\uparrow} v^*_m(r_i, E)]
\end{aligned}
\tag{7.6}
$$

where β and $\beta^\dagger$ are quasi-particle operators , and $u_m(r_i, E)$, $v_m(r_i, E)$ are the quasi-particle amplitudes associated with an eigen energy E_n.

In the Hartree-Fock mean-field approximation incorporating charge-order and superconducting decoupling along with the above canonical transformation we have,

$$
\begin{pmatrix}
H_{ss} & \Delta_s & -N_{sl} & \Delta_{sl} \\
\Delta^*_s & -H_{ss} & \Delta^*_{sl} & N_{sl} \\
-N_{ls} & \Delta_{ls} & H_{ll} & \Delta_l \\
\Delta^*_{ls} & -N_{ls} & \Delta^*_l & -H_{ll}
\end{pmatrix}
\begin{pmatrix}
u_s(r_i, E) \\
v_s(r_i, E) \\
u_l(r_i, E) \\
v_l(r_i, E)
\end{pmatrix}
= E
\begin{pmatrix}
u_s(r_i, E) \\
v_s(r_i, E) \\
u_l(r_i, E) \\
v_l(r_i, E)
\end{pmatrix}
\tag{7.7}
$$

where (the excitation eigen-value $E \geq 0$)

$$
\begin{aligned}
H_{mm} u_m(r_i, E) &= (\epsilon_{im} - \mu^*_{im}) \, u_m(r_i, E) - \sum_j t_m u_m(r_j, E) \\
N_{mm'} u_{m'}(r_i, E) &= \left\{ \frac{1}{2} |U_{mm'}| \langle n_{mm'} \rangle + t_{mm'} \right\} u_{m'}(r_i, E) + \sum_j t^{nn}_{mm'} u_{m'}(r_j, E)
\end{aligned}
$$

$$\tag{7.8}$$

j is the nearest neighbour of i We can express the particle densities and the pairing amplitudes in terms of the quasi-particle amplitude as

$$\langle n_{im} \rangle \; = \; 2 \int dE |u_m(r_i, E)|^2 f(E) + |v_m(r_i, E)|^2 [1 - f(E)]$$

$$\langle n_{imm'} \rangle \; = \; 2 \int dE u_{m'}(r_i, E) u_m^*(r_i, E) f(E) + v_{m'}^*(r_i, E) v_m(r_i, E) [1 - f(E)]$$

$$\Delta_m \; = \; |U_m| \int dE v_m^*(r_i, E) u_m(r_i, E) f(E) - u_m(r_i, E) v_m^*(r_i, E)[1 - f(E)]$$

$$\Delta_{mm'} \; = \; |U_{mm'}| \int dE v_m^*(r_i, E) u_{m'}(r_i, E) f(E) - u_m(r_i, E) v_{m'}^*(r_i, E)[1 - f(E)]$$

$$(7.9)$$

where $f(E)$ is the Fermi function. A fully self-consistent solution of (7.7) can be obtained provided all the normal potentials ($|U_m| n_{im}$ and $|U_{mm'}| n_{imm'}$) and anomalous potentials (Δ_{im} and $\Delta_{imm'}$) are determined self consistently from Eqn. (7.9). The self-consistency criteria is set to 10^{-6} for calculation of all self-consistent parameters throughout the present study.

7.2.2   Disorder and Multi-band superconductivity.

The class of systems which we shall study here will be binary substitutionally disordered alloys with randomness in the diagonal site-energies, $\{\varepsilon_{il}\}$, of one of the two bands, say the l-band only. We shall introduce site occupation variables $\{m_i\}$ which take values 1 or 0 according to whether the site labeled i is occupied by a A-type or a B-type of atom.

$$\varepsilon_{il} = \varepsilon_A m_i + \varepsilon_B (1 - m_i) \tag{7.10}$$

where ε_A and ε_B are the possible on-site energies corresponding to l band. We define the strength of disorder D as $|\varepsilon_A - \varepsilon_B|$.

If the concentrations of A and B-type of atoms in the solid are x and y, then using the same formalism as given in the previous chapter, Chapter 6;Section "Disorder and Superconductivity", we get,

$$\varepsilon_{il} \; = \; \varepsilon_B + \delta\varepsilon \; m_i \quad \text{is replaced by}$$

$$\Rightarrow \quad \ll \varepsilon_{il} \gg + (y - x)\delta\varepsilon \; \gamma_i^\dagger \gamma_i + \sqrt{xy} \; \delta\varepsilon \; \left(\gamma_i^\dagger + \gamma_i \right)$$

$$(7.11)$$

where $\ll \varepsilon_l \gg = x\varepsilon_A + y\varepsilon_B$, $\delta\varepsilon = \varepsilon_A - \varepsilon_B$ and $D = |\delta\varepsilon|$.

For the present system the Hamiltonian contains the random variables $\{\varepsilon_{il}\}$. So we need to construct the Hamiltonian in the augmented space $\Psi = \mathcal{H} \otimes \prod_i^{\otimes} \Phi_i$ (like we had done in the previous chapter, Chapter 6 of the thesis) by replacing all the random variables ε_{il} by the corresponding operators shown in Eqn. (7.11). The effective augmented space Hamiltonian becomes :

$$
\begin{aligned}
\widetilde{\mathbf{H}}_{\text{eff}} \;=\; &- \sum_{\langle i,j\rangle, m, m', \sigma} t_{im,jm'} \, c^{\dagger}_{im\sigma} c_{jm'\sigma} + \sum_{i\sigma}(\ll \varepsilon_l \gg -\mu^*_{il}) n_{il\sigma} \ldots \\
&+ \sum_{i\sigma} \delta\epsilon \, n_{il\sigma}\{(y-x)\gamma^{\dagger}_i \gamma_i + \sqrt{xy}(\gamma^{\dagger}_i + \gamma_i)\} + \sum_{i\sigma}(\epsilon_{is} - \mu^*_{is}) n_{is\sigma} \ldots \\
&- \sum_{im, m', \sigma} |U_{mm'}| \frac{\langle n_{imm'\sigma}\rangle}{2} c^{\dagger}_{im\sigma} c_{jm'\sigma} + \sum_{im}\left(\Delta_m c^{\dagger}_{im\uparrow} c^{\dagger}_{im\downarrow} - \Delta^*_m c_{im\uparrow} c_{im\downarrow}\right) \ldots \\
&+ \sum_{i, m, m'}\left(\Delta_{mm'} c^{\dagger}_{im\uparrow} c^{\dagger}_{im'\downarrow} - \Delta^*_{mm'} c_{im\uparrow} c_{im'\downarrow}\right)
\end{aligned}
$$

$$(7.12)$$

Here all the symbols have the same meaning as before.

After constructing the Hamiltonian in augmented space the augmented space theorem then automatically ensures that the configuration average is a projection onto the state with no 'fluctuations' [Mookerjee 1973] :

$$
\ll \underline{\mathbf{G}}(i,i,E) \gg = \langle \emptyset | \widetilde{\underline{\mathbf{G}}}(i,i,E) | \emptyset \rangle
$$

where $\widetilde{\underline{\mathbf{G}}} = (E\widetilde{\underline{\mathbf{I}}} - \widetilde{\underline{\mathbf{H}}}_{\text{eff}})^{-1}$. All operators here are 4×4 matrices in the space spanned by the two bands and the electron-hole degrees of freedom.

The Green functions are then obtained using the vector recursion technique introduced by Haydock and Godin [Godin and Haydock 1988, Godin and Haydock 1992]. The vector recursion has been described in great detail in the given references. We shall indicate the main points and the interested reader may refer to the quoted references for details. Once the BdG Hamiltonian is set up as in Eqn.(7.7) and the effective augmented

space transformation carried out as in Eqn.(7.5), the vector recursion technique essentially changes the basis in order to block tridiagonalize the effective Hamiltonian. The basis is recursively generated :

$$
|1 \gg \;=\; \begin{pmatrix} u_s(\vec{r}_i, E) \otimes \{\emptyset\} \\ v_s(\vec{r}_i, E) \otimes \{\emptyset\} \\ u_l(\vec{r}_i, E) \otimes \{\emptyset\} \\ v_l(\vec{r}_i, E) \otimes \{\emptyset\} \end{pmatrix}
$$

$$
\underline{B}^\dagger_{n+1}|n+1 \gg \;=\; \widetilde{\underline{H}}\,|n \gg -\underline{\underline{A}}_n|n \gg -\underline{\underline{B}}_n|n-1 \gg
$$

The coefficients $\underline{A}_n$ and $\underline{B}_n$ are obtained from the orthogonality of the generated basis and between rows of the same basis The configuration averaged diagonal matrix element of the Green function then follows as a matrix continued fraction :

$$
\ll \underline{G}(\vec{r}_i\vec{r}_i; E) \gg = \ll 1|\mathbf{G}|1 \gg = \underline{G}_0(E)
$$

$$
\underline{G}_n(E) = \left(z\underline{I} - \underline{\underline{A}}_n - \underline{B}^\dagger_{n+1}\underline{G}_{n+1}(E)\underline{\underline{B}}_{n+1} \right)^{-P_{n-1}}
$$

$$
n \;=\; 0, 1, 2, \ldots N_2 - 1
$$

where A^{-P_n} denotes inverse in the subspace spanned by the basis $\{|n+1 \gg, |n+2 \gg \ldots\}$. The matrix continued fraction is terminated in two steps. The matrix coefficients $\{\underline{A}_n, \underline{B}_n\}$ are calculated exactly for $n < N_1$, then : first, by putting $\underline{\underline{A}}_n = \underline{\underline{A}}_{N_1}$ and $\underline{B}_n = \underline{B}_{N_1}$ for all $N_1 \leq n < N_2$ and second, $\underline{G}_{N_2}(E) = (E + i\eta)^{-1}\underline{I}$

The physical quantities of interest (Eqn.(7.9)) relevant to the study can be expressed as appropriate matrix elements of the Green's function.

$$
\langle n_m \rangle \;=\; -\frac{1}{\pi}\lim_{\eta \to 0}\,\mathrm{Im}\,\int_{-\infty}^{\infty}\left[\mathbf{G}^{++}_{mm}(i, i, E + i\eta)f_n + \mathbf{G}^{--}_{mm}(i, i, E + i\eta)(1 - f_n)\right]dE
$$

$$
\Delta_m \;=\; -\frac{1}{\pi}\lim_{\eta \to 0}\,\mathrm{Im}\,\int_{-E_c}^{+E_c}\left[\mathbf{G}^{+-}_{mm}(i, i, E + i\eta)f_n + \mathbf{G}^{-+}_{mm}(i, i, E + i\eta)(1 - f_n)\right]dE
$$

$$
\langle n_{mm'} \rangle \;=\; -\frac{1}{\pi}\lim_{\eta \to 0}\,\mathrm{Im}\,\int_{-\infty}^{\infty}\left[\mathbf{G}^{++}_{mm'}(i, i, E + i\eta)f_n + \mathbf{G}^{--}_{mm'}(i, i, E + i\eta)(1 - f_n)\right]dE
$$

$$\Delta_{mm'} = -\frac{1}{\pi} \lim_{\eta \to 0} \text{Im} \int_{-E_c}^{+E_c} \left[\mathbf{G}_{mm'}^{+-}(i,i,E+i\eta) f_n + \mathbf{G}_{mm'}^{-+}(i,i,E+i\eta)(1-f_n) \right] dE$$

$$(7.13)$$

Where the energy interval $[-E_c, +E_c]$ is the short interval around the Fermi-energy of the system where the interaction has its effect.

7.3   Discussion of Results.

7.3.1   Ordered Systems.

In this section we shall present results on ordered two band (both the bands having s-orbital character) superconductors in a square and cubic lattice for both local intra and inter-band Hubbard parameter. The system is kept fixed at half-filling unless otherwise mentioned. Since these results are well known from other approaches, so a comparison will ascertain the viability and numerical accuracy of our proposed methodology.

For our model system the hopping integrals are chosen as follows : in Figs. 7.1 (a),(b),(c) and (d) the intra-band nearest neighbour hopping elements are t_s=1.0 and t_l=0.5 and the inter-band on-site hopping t_{sl}=0.0.

The s- and l-band local density of states (LDOS) for the case when $U_s = U_l = U_{sl} = 0$ for the ordered system is shown in Fig.7.1 (a) and (c) for the square and cubic lattice respectively. The two sets of LDOSes exactly match the standard calculations using Bloch's theorem. One can clearly see in Fig. 7.1 (a) the band-center integrable Van Hove singularity, the two flanking kink singularities and the square-root singularities at the band edges that are characteristic of a square lattice. The cubic lattice LDOS [see Fig.7.1 (c)] is characterized by constant DOS at the band center and kink singularities at two ends. The band (s-band) with greater intra-band hopping integral is wider, as expected.

Next we investigate the situation when the intra-band Hubbard parameter is finite but the inter-band pairing is zero. This corresponds to the system studied by Suhl *et al* [Suhl *et.al.* 1959] in the absence of inter-band tunnelling of electrons. Thus $|U_{mm'}|$ (that is U_{sl}) in Eqn.(7.1) is set to zero. In Fig.7.1 (b) and (d) we consider U_s=$U_l = -4.0$ and both the bands are equally filled for a square and cubic lattice respectively and the system is kept
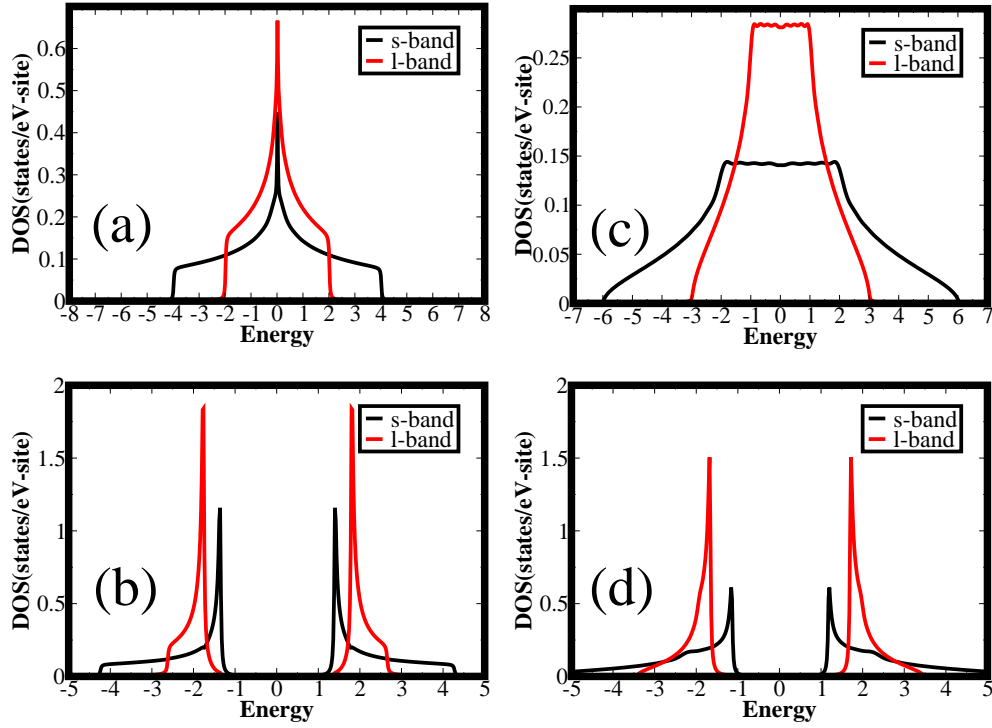
Figure 7.1: Study of superconductivity in an ordered 2d system [(a) and (b)] and 3d system[(c) and (d)] having two bands s and l. (1) Intra-band hopping integrals : $t_s=1.0$ and $t_l=0.5$ and (2) Hubbard parameters are for (a) and (c) $U_s=U_l=U_{sl}=0.0$ and (b) and (d) $U_s=U_l=4.0$ and $U_{sl}=0$.

fixed at half filling. The BdG equations are solved recursively and self-consistently as described earlier. After self-consistency the superconducting order parameter Δ_s and Δ_l are found to be finite. The s and l LDOS for the system are calculated by using the relation

$$n_s(E) = -\frac{1}{\pi}\lim_{\eta\to 0}\Im m\, G_{ss}^{++}(1,1,E+i\eta)$$

$$n_l(E) = -\frac{1}{\pi}\lim_{\eta\to 0}\Im m\, G_{ll}^{++}(1,1,E+i\eta)$$

where η is an infinitesimal positive imaginary part of the energy and + and - refer to electron and hole degrees of freedom of the BdG formalism.

The LDOS for these parameters is shown in Fig7.1(b) and (d) for the square and cubic lattices respectively. Though the interaction U_s=U_l, we find from the s and l partial DOS that Δ_s and Δ_l are different. This is due to the difference in band width (W) as $t_s \neq t_l$, and the effective parameter $\frac{U_m}{W}$ (m=s or l) is responsible for the magnitude of the gap seen in the local DOS.

In view of above we have also investigated the situation only with intra-band interaction but $U_s \neq U_l$. We have considered $U_s = -3.0$ and $U_l = -1.0$. Since the effective parameter $\frac{|U_s|}{W}$=0.75 > $\frac{|U_l|}{W}$=0.5 is larger for the s-band we did find $\Delta_s > \Delta_l$. The earlier study by Suhl et al. [Suhl *et.al.* 1959] had also found two different band gaps arising in a two band model system when the inter-band interaction is zero but the intra-band interactions are finite. Two different band gaps were first observed in MgB_2 [Wang *et.al.* 2001, Bouquet *et.al.* 2001, Yang *et.al.* 2001, Szabo *et.al.* 2001, Giubileoo *et.al.* 2001, Chen *et.al.* 2001, Tsuda *et.al.* 2001]. The theoretical study explaining this result [Choi *et.al.* 2002] had argued that the cause of the different band gaps to be different strengths of coupling to the phonons resulting in different strengths of electron pairing in two different bands.

We now consider a situation where the inter-band interaction is finite but the intra-band interaction is zero. Let us consider the intra-band hopping integrals for the two bands to be t_s=1.0 and t_l=0.1 respectively, then by varying the inter-band Hubbard parameter (keeping the intra-band parameter to be zero) as expected we get the three regimes as discussed by Moreo *et al.* [Moreo *et.al.* 2009] : the "normal" regime or non-superconducting state, the "breached" regime where one of the bands is superconducting and the other is not and the "BCS" regime where both the bands are gapped. These regimes are shown in Fig. 7.2(a),(b) and (c) for a 2D system and (d),(e) and (f) for a 3D system respectively. For these systems we observe from Fig. 7.2 that the wider band (*s*-band with t_s=1.0) remains gapped (thus superconducting) in the "breached" regime, the inter-band Hubbard parameter being the cause of the gap in the DOS. In future we intend to develop our method in k-space to be able to obtain some other quantities of interest (like the mean-field state population as a function of momentum obtained by Moreo *et.al.* 2009) inorder to have a better insight into the electronic behaviour in the very special "breached regime" where while some of the electrons are paired up into "Cooper pairs"
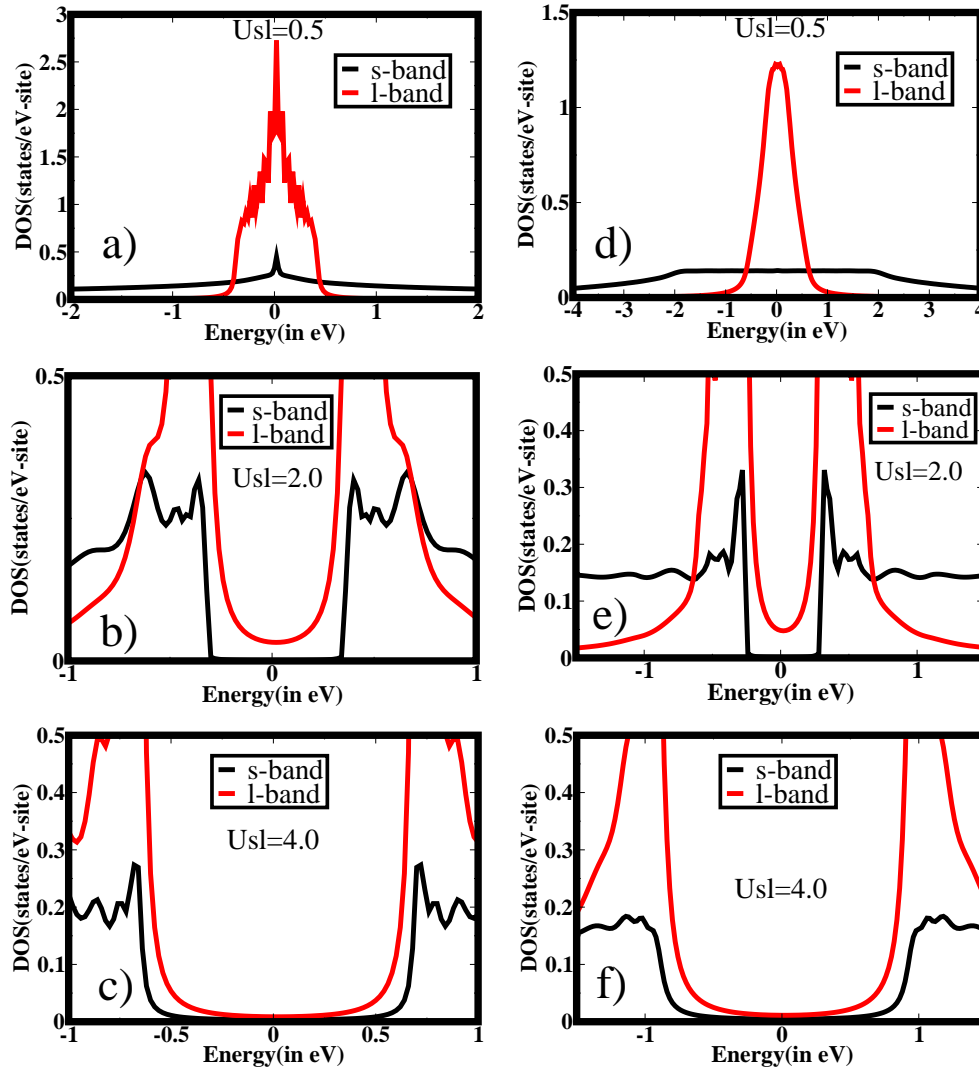
Figure 7.2: Study of DOS for an ordered system where intra-band interaction potential is zero but inter-band interaction potential is finite. Here the intra-band hopping integrals are t_s=1.0 and t_l=0.1 respectively. The inter-band hopping integral $t_{sl} = 0$. (a),(b) and (c) corresponds to the system being in the "normal", "breached" and "superconducting" state.

others may behave like normal unpaired electrons.
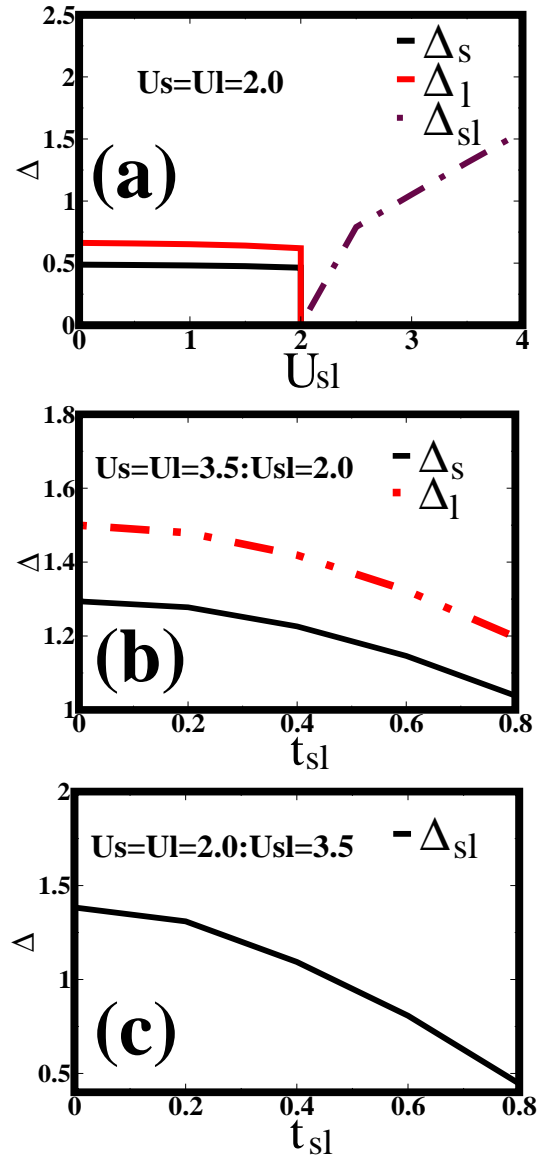
Figure 7.3: Study of Δ for a 2D ordered system when both intra and inter-band interaction potentials are finite. Here the intra-band hopping integrals are $t_s=1.0$ and $t_l=0.5$ for the s and l-bands respectively. In (a) the intra-band pairing potentials $|U_s|$ and $|U_l|$ are kept fixed at 2.0 and U_{sl} is varied. In (b) and (c) the pairing potentials are kept fixed [(b) $U_s = U_l > U_{sl}=2.0$ and (c) $U_s = U_l < U_{sl}=3.5$] and the effect of variation of inter-band intra-site hopping integral t_{sl} is studied.

In the presence of both the inter and intra-band Hubbard parameters an interesting

competitive effect sets in as seen from Fig.7.3(a). We keep the intra-band attractive Hubbard parameter fixed ($U_s=U_l=2.0$), and vary the inter-band Hubbard parameter U_{sl}. The intra-band hopping integrals are $t_s=1.0$ and $t_l=0.5$ and inter-band on-site hopping integral $t_{sl}=0.2$. We see (from Fig.7.3(a)) when $U_s=U_l \geq U_{sl}$ then it is the intra-band pairing amplitude is finite and the inter-band pairing amplitude that is zero. On the other hand, When $U_s=U_l < U_{sl}$ (Fig.7.3(c))then it is the inter-band pairing amplitude that is finite and inter-band pairing amplitude is zero. Our calculations show depending on the strength of the attractive interaction, a particular kind of pairing either intra-band or inter-band is only possible for s-like bands in half-filled systems. Finally, we examine the effect of the inter-band (on-site) hopping integral t_{sl} on the pairing amplitude Δ for a half-filled system. In Fig.(7.3)(b) where $U_s=U_l=3.5 > U_{sl}=2.0$, both Δ_s and Δ_l, the pairing amplitudes for the s- and l-bands respectively, decreases with increase in t_{sl}. Here Δ_{sl} is zero. In Fig.7.3 (a) its seen when $U_s=U_l=2.0 < U_{sl}=3.5$, with increase in t_{sl} the inter-band pairing amplitude Δ_{sl} decreases. Here the intra-band pairing amplitudes are zero. Therefore inclusion of intra-band on-site hopping hardly changes the qualitative picture for a two band system.

Having studied the ordered system we shall now consider the role of disorder in multi-band systems.

7.3.2   Homogeneously disordered systems.

We shall now look into an attractive-U Hubbard model of a binary, randomly substitutional alloy on a square lattice, with two bands. For systems with disorder we shall confine our study only to 2D systems. We consider randomness in the on-site energy in one of the two channels, namely the l-channel, and study its effect on the other channel. We introduce randomness in the on-site energy using Eqn.(7.11) and our Hamiltonian takes the form given in Eqn.(7.12). The concentrations are $x = y = 0.5$ and the system is half-filled throughout the study.

To begin with, we study the systems under situations similar to those under which we had investigated the corresponding ordered system. We keep $t_s = 1.0$ and $t_l = 0.5$ and the strength of disorder $D = |\epsilon_a - \epsilon_b| = 1$ throughout the cases considered in Fig.7.4.

First we study the case when the system is non-superconducting ($U_s = U_l = U_{sl} = 0.0$). From Fig.7.4(a) we find due to the absence of hybridization between the s and l bands the s-DOS is hardly affected by randomness in the l-channel. The l-DOS (Fig.7.4(b)), however, has characteristic features of disordered DOS-namely increase in band-width and smoothing out of Van Hove singularities. So, the total DOS (Fig.7.4(c)) has signatures of disorder as well.

Next, we investigate the DOS of the same system considering only the intra-band Hubbard parameters to be finite i.e., $U_s = U_l = 4.0$ and $U_{sl} = 0.0$ (Fig.7.4(d),(e) and (f)). In this case the intra-band pairing amplitudes Δ_s and Δ_l are only finite (see Eqn(7.3)). We see that though the s-DOS remains unaffected by randomness in the l-channel (comparing Fig.7.4(d) with Fig.7.1(b)), the disorder influences the l-DOS(comparing Fig.7.4(e) with Fig.7.1(b)). But since both the s-DOS and l-DOS are gapped, the total DOS remains gapped (Fig.7.4(f)). Similar behaviour also prevails with the inclusion of attractive inter-band interaction U_{sl}, such that $U_{sl} < U_l$ and U_s. The variation of the zero temperature superconducting order parameter Δ_s, Δ_l and Δ_{sl} is plotted as a function of the strength of disorder in Fig.7.5(a) where $U_s=U_l=2.0 > U_{sl}=1.0$. As expected only the intra-band pairing are finite and Δ_s does not change as it does not register the effect of the disorder in the l-channel. The effect of disorder is to reduce Δ_l as the strength of disorder increases but Δ_l remains finite indicating the existence of superconductivity. Therefore in the chosen parameter regime for the two band system the situation is similar to that predicted by Anderson theorem for single band system, where the gap survives in the quasi-particle spectrum even in the presence of disorder.

Next, we investigate what happens when $U_s=U_l=0.0$ and U_{sl} is finite. For the disordered case with inter-band pairing alone, here we set the intra-band hopping integrals for the s- and l-bands (we choose $t_s=1.7$ and $t_l=0.3$ respectively). t_s and t_l are very different and the s- and l- channel DOS are quite different, so that they have different gap structures at the Fermi level even with a single inter-band gap parameter or pairing amplitude. Interestingly the 3 regimes survive even in the presence of disorder. In the "breached" regime again the wider band (for us the s-band) is the one that is capped and the l-band has finite density of states at the Fermi-level. We find that superconductivity in disordered multi-band system with only inter-band interaction preserves the feature for

the system without disorder provided the inter-band coupling is strong.
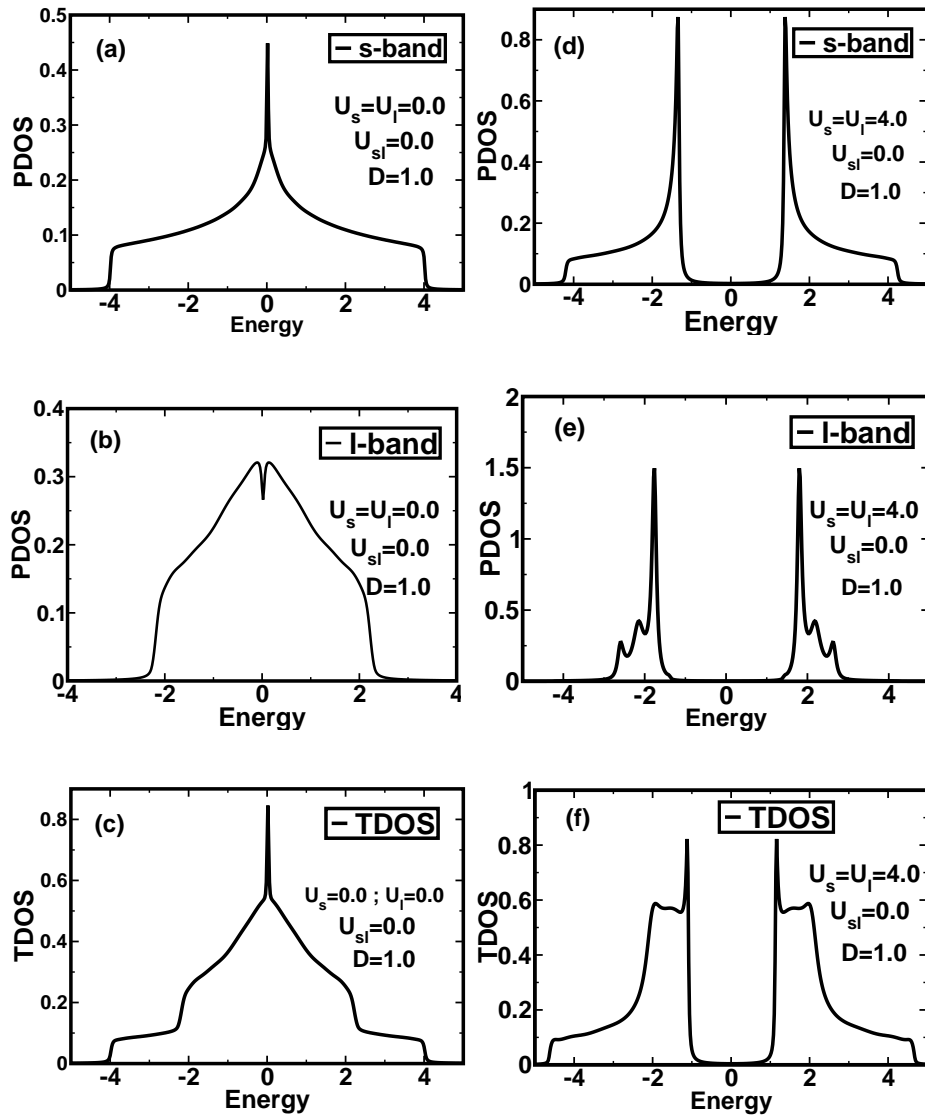
Figure 7.4: Study of a 2-band superconducting system in square lattice with disorder in the *l*-channel with strength D=1.0. While (a),(b) and (c) studies the s, l and Total DOS respectively for the non-superconducting case (where intra and inter-band Hubbard potential $U_s=U_l=U_{sl}=0.0$) (d), (e) and (f) studies the effect of disorder on the corresponding superconducting system when intra-band interaction is finite and inter-band interaction is 0. This is basically Suhl's system in the absence of inter-band tunnel-ling of Cooper pairs.
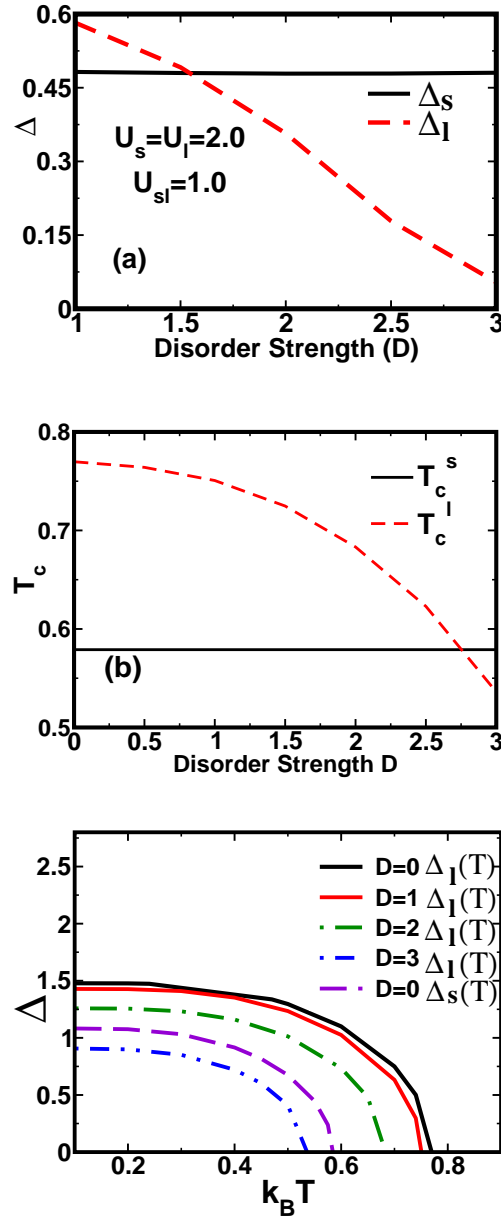
Figure 7.5: (a) Variation of Δ as a function of disorder strength (D) in the l-band when $U_s = U_l > U_{sl}$. (b) Variations of s-band and l-band critical temperatures T_{cs} and T_{cl} as a function of disorder strength D when only intra-band pairing occurs in a two-band s-wave superconductor in a square lattice. (c) Variation of $\Delta_s(\text{T})$ and $\Delta_l(\text{T})$ with T for various strengths of disorder D in the l-band.
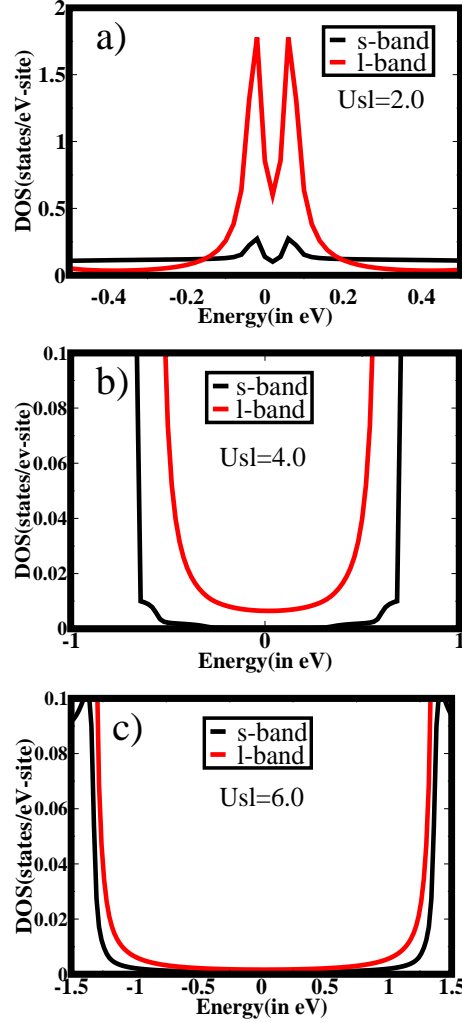
Figure 7.6: A study of DOS for a superconducting system with disorder in the *l*-band (strength of disorder D=1.0) when intra-band interaction potential is zero but inter-band interaction potential is finite. Here the on-site hopping integral for the *s*- and *l*-band are wide apart (t_s=1.7 and t_l=0.3 respectively). Inter-band hopping integral t_{sl}=0. a),b) and c) corresponds to the system being in the "normal", "breached" and "superconducting" state.

Suhl *et al.* [Suhl *et.al.* 1959] using a generalized BCS Hamiltonian for the two band superconductor proposed a generalized expression for temperature dependent pairing amplitude. Now as said earlier our 2-band Hubbard Hamiltonian without the inter-band pairing term is identical to Suhl *et al.*. The corresponding expression for temperature dependent pairing amplitude to obtain a corresponding expression for T_c for the *s*- and *l*-bands (T_{cs} and T_{cl} respectively) which are given by:

$$1 = |U_s| \int_{-\infty}^{\infty} dE \frac{\bar{N}_s(E)}{2E} \tanh \left(\frac{E}{2k_B T_{cs}} \right) \tag{7.14}$$

and

$$1 = |U_l| \int_{-\infty}^{\infty} dE \frac{\bar{N}_l(E)}{2E} \tanh \left(\frac{E}{2k_B T_{cl}} \right) \tag{7.15}$$

where $\bar{N}_s(E)$ and $\bar{N}_l(E)$ are the *s* and *l*-band configuration averaged density of states in the normal state at energy E, when we have diagonal disorder D in the *l*-band. Setting $U_s = U_l = -3.5$, $x = y = 0.5$ and keeping the system fixed at half-filling, we obtain the corresponding T_{cs} and T_{cl} for different D (see Fig.7.5(b)). As seen from the Figure T_{cs} remains constant with increasing disorder strength D. This is because randomness in the *l*-band does not affect the *s*-band in the presence of intra-band pairing alone. T_{cl} is however suppressed with increasing D. At this point however it must be noted that only the higher of the two critical temperatures [T_{cs} and T_{cl}] is physically significant in this respect. So in the present case, T_c first decreases with disorder and then becomes constant when $T_{cs} > T_{cl}$.

These conclusions are further strengthened by a study of the pairing amplitude as a function of temperature. For the 2-band *s*-wave superconductor in square lattice when intra-band pairing occurs only then the expressions for the temperature-dependent pairing amplitudes are :

$$1 = |U_s| \int_{-\infty}^{\infty} dE \frac{\bar{N}_s(E)}{2 \left(E^2 + \Delta_s^2(T) \right)^{\frac{1}{2}}} \tanh \left(\frac{\left(E^2 + \Delta_s^2(T) \right)^{\frac{1}{2}}}{2k_B T} \right) \tag{7.16}$$

and

$$1 = |U_l| \int_{-\infty}^{\infty} dE \frac{\bar{N}_l(E)}{2 \left(E^2 + \Delta_l^2(T) \right)^{\frac{1}{2}}} \tanh \left(\frac{\left(E^2 + \Delta_l^2(T) \right)^{\frac{1}{2}}}{2k_B T} \right) \tag{7.17}$$

for the s- and l-bands respectively.

We see that with increase in disorder strength D in the l-band the temperature dependent pairing amplitude Δ_l reduces much like the zero-temperature pairing amplitude (see Fig. 7.5(c)). Since randomness in the l-channel does not affect the s-band thus $\Delta_s(T)$ is not affected by D so we plot $\Delta_s(T)$ vs T only at D=0 (see Fig. 7.5(c)). But the significant conclusion from Fig. 7.5(b) and (c) is that for temperatures below the critical temperatures though D suppresses $\Delta(T)$, but does not reduce it to zero.

The next set of studies is the investigation of the effect of increasing strength of disorder D on a 2 band attractive U Hubbard model with dominant inter-band attractive interaction $U_{sl} > U_{ss}, U_{ll}$. In the parameter regime $U_s=U_l=1.0 < U_{sl}$ as expected the dominant pairing is the inter-band pairing U_{sl} that affects both the bands. In contrast to the case where the intra-band pairing interaction is dominant, here for a critical disorder study D > 2 the pairing amplitude Δ_{sl} vanishes indicating the possible disappearance of superconductivity [see Fig. 7.7(a)]. This is further illustrated in the DOS plot for the s and l channel in Fig. 7.7(b) and Fig. 7.7(c) respectively. Here the presence of randomness in the l channel affect Δ_{sl} and this in turn affects both s and l-DOS. With increasing disorder D in the l-channel the gaps both in the s-DOS and l-DOS reduce and eventually finite DOS at the Fermi level is realized. So in the case of inter-band pairing and in the presence of disorder superconductivity may not survive in contrast to single band systems. But why is inter-band pairing more sensitive to disorder than intra-band pairing is an issue which needs to be looked into in greater details in future.

7.3.3   Summary.

In this chapter we have developed a real space approach to study the effect of disorder on multi-band superconductivity using a 2-band Hubbard Hamiltonian to model our system and augmented space vector-recursion method to handle randomness in our system. We have established the accuracy of our method by comparing our results with those obtained using other techniques in the ordered situation. We have seen two-gapped situation in the presence of intra-band pairing. In the presence of inter-band pairing although there is only a single kind of pairing thus a single pairing amplitude, two different gaps open
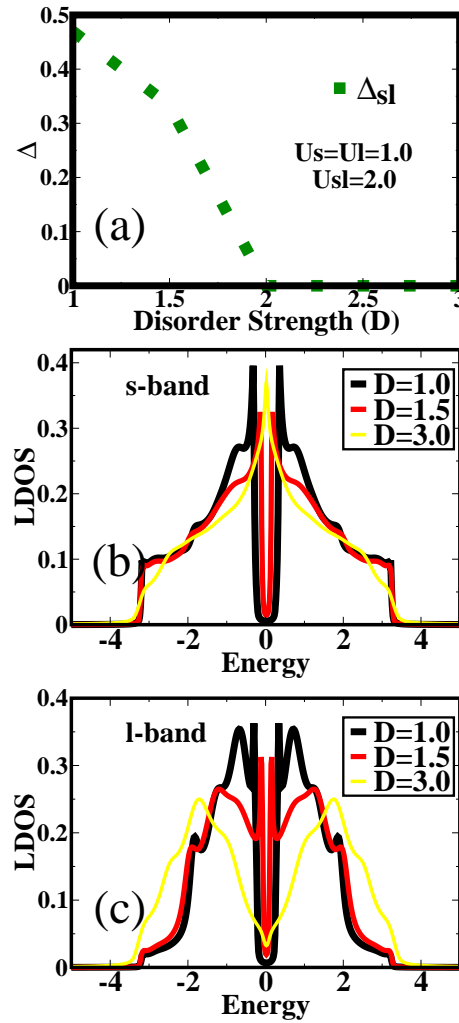
Figure 7.7: (a) studies Δ as a function of Disorder Strength (D) in the l-band when $U_s=U_l < U_{sl}$.(b) and (c) studies DOS for a 2D superconducting system with disorder in the l-band when $U_s= U_l < U_{sl}$.

up if the band structure of the bands are different. For this kind of pairing we have also obtained the non-superconducting, the breached and the BCS superconducting regimes by varying the inter-band pairing potential.

We have studied the effect of randomness in one channel on the other. When only intra-band pairing occurs, then randomness in one channel does not affect the other. But in the presence of inter-band pairing both the bands are affected by randomness in any one of the channels. Here too by varying the inter-band Hubbard parameter the three paradigms, namely, the non-superconducting, breached and BCS superconducting regimes may be obtained, but the threshold potential required to crossover from one regime to another is much higher.

By increasing the strength of disorder its seen that although superconductivity survives when intra-band pairing occurs, in the presence of inter-band pairing the gaps in both the channels close up with increasing disorder.

Our calculation indicates inter-band pairing which was not considered in earlier work is not only interesting but opens up a paradigm beyond Anderson's theorem to understand superconductivity in disordered systems. But we need to further investigate the physical reason behind this striking phenomena in future projects.

Chapter 8

Non-collinear magnetism in disordered alloys : application to MnPt

8.1 Introduction

In this chapter[1] we have developed a formalism by combining the tight binding linearized muffin-tin orbital and the recursion methods with the augmented space formalism (TB-LMTO-ASR) to study non-collinear magnetism in disordered alloys. We apply the TB-LMTO-ASR to study disordered MnPt alloy. Electronic structure of this alloy in different magnetic structures have been calculated and compared to the previous theoretical results.

Anti-ferromagnetic materials have attracted attention because of their potential candidature for giant magneto-resistance (GMR) devices. From a microscopic viewpoint, it is interesting to examine how lattice structure, composition, long-ranged disorder and short-range ordering determine the magnetic structure of anti-ferromagnetic alloys. In many random alloys with closed packed lattice configurations, magnetic structures can become quite complex as compared to the simple collinear anti-ferromagnetic picture usually assumed. Atomic arrangement and randomness may introduce frustration effects in such alloys. Neutron diffraction experiments have often suggested complex magnetic alignments in mostly Mn-based disordered alloys like FeMn, MnPt, Mn_3Pt and Mn_3Rh due to the presence of almost half-filled Mn 3d orbitals. Non-collinear magnetism has

---

been studied within the density functional theory in formalisms, where the energies are functionals not of charge density but density matrices in spinor space. This has been done for ordered alloys [Kübler *et.al.* 1988, Sticht *et.al.* 1989 and Uhl *et.al.* 1994], amorphous materials [Lorenz *et.al.* 1995 and Kakehashi *et.al.* 1998] and disordered alloys [Shulthess *et.al.* 1999 and Sakuma 2000] based on both the Korringa-Kohn-Rostocker (KKR) and linear muffin-tin orbitals (LMTO) methods, coupled with the single-site coherent potential approximation (CPA) to deal with disorder.

In this work we propose to generalize the augmented space recursion [Mookerjee 1973] (ASR) based on the tight-binding version of the LMTO (TB-LMTO) so that it is capable of describing non-collinear magnetism. We have shown earlier [Mookerjee and Bishop 1974 and Razee *et.al.* 1991] that the CPA appears as a specific approximation within the augmented space formalism, so that in usual cases the ASR will subsume the CPA. However, wherever effects of statistical clustering [Kumar *et.al.* 1982], short-ranged order [Mookerjee and Prasad1993-Saha *et.al.* 1994], partial disorder [Chakrabarti and Mookerjee 2001] and local lattice distortions due to large size mismatch of constituent atoms in the alloy [Saha and Mookerjee 1996] become important, the ASR provides an analyticity and symmetry preserving generalization to the CPA capable of addressing these situations accurately.

The rest of the chapter is arranged as follows : In the following section we shall briefly discuss the Kohn-Sham equation generalized within the density-matrix functional theory to take care of non-collinear magnetism. Subsequently, we shall obtain a representation of the Kohn-Sham 'Hamiltonian' in the TB-LMTO basis. In the next section we shall introduce substitutional disorder and the augmented space formalism to take care of configuration averaging. The fourth section will be a brief description of the scalar recursion method. Finally, in the last section we shall apply our formalism to study the possibility of non-collinear magnetism in disordered MnPt alloy.

8.2   Basic Formulation

8.2.1   The Kohn-Sham equation with non-collinear magnetism

Since our aim is to study alloys via the augmented space recursion technique, we would like to develop a methodology which gives rise to a sparse Hamiltonian representation with matrix elements obtained self-consistently through a density functional formulation. The generalization of the collinear local spin-density approximation (LSDA) begins at the level of the Kohn-Sham equation. The Kohn-Sham orbitals in a spin-polarized electron liquid are spinors of the form :

$$\underline{\underline{\psi}}(E,\vec{r}) = \begin{pmatrix} \psi_1(E,\vec{r}) \\ \psi_2(E,\vec{r}) \end{pmatrix}$$

.

The magnetization density, like the charge density is a local function. We shall describe our system on a more coarse grained level. We shall start with the "rigid spin approximation" in which we shall associate with each Wigner-Seitz cell (or atomic sphere if we use the atomic sphere approximation) labeled by $\vec{R}$ a unique direction of magnetization. This direction will be the *local* quantization axis characterized by two angles θ_R, ϕ_R with respect to a set of suitably chosen global axes. With respect to these global axes the Kohn-Sham equation may be written as :

$$\left\{ \left(-\frac{1}{2}\nabla^2 \right) \mathbf{I} + \mathbf{V}^{\mathrm{KS}}(\vec{r}) \right\} \underline{\underline{\psi}}(E,\vec{r}) = E\underline{\underline{\psi}}(E,\vec{r}) \tag{8.1}$$

where the effective Kohn-Sham potential is :

$$\mathbf{V}^{\mathrm{KS}}(\vec{r}) \;=\; \sum_R \left\{ V_{\mathrm{Hart}}(\vec{r}_R) + V_{\mathrm{ie}}(\vec{r}_R) + V_{\mathrm{SR}}(\vec{r}_R) \right\} \mathbf{I} + \mathbf{V}_{\mathrm{xc}}(\vec{r}_R) + v(r)\,\vec{L}\cdot\vec{\mathbf{S}} \tag{8.2}$$

where, $\vec{r}_R = \vec{r} - \vec{R}$, $V_{\mathrm{Hart}}(\vec{r}_R)$ is the Hartree potential, $V_{\mathrm{ie}}(\vec{r}_R)$ the ion-electron potential and $V_{SR}(\vec{r}_R)$ is the scalar relativistic correction. $\mathbf{V}_{\mathrm{xc}}(\vec{r}_R) = V_{xc}^{(1)}\mathbf{I} + \vec{B}\cdot\vec{\mathbf{S}}$ is the exchange-correlation potential where,

$$\vec{B}(\vec{r}) = \sum_R V_{xc}^{(2)}(\vec{r}_R)\ \vec{e}_R$$

$\vec{e}_R$ is the unit vector along the direction of the local quantization axis within the R-th Wigner-Seitz cell.

The Kohn-Sham Hamiltonian acts on the Hilbert space $\mathcal{H} \otimes \mathcal{S}$ where $\mathcal{S}$ is the spin space spanned by the bi-spinors $\begin{pmatrix} 1 \\ 0 \end{pmatrix}$ and $\begin{pmatrix} 0 \\ 1 \end{pmatrix}$. $\vec{\mathbf{S}}$ are spin operators in the space $\mathcal{S}$.

The local and global spinor bases are related to each other through the SU(2) rotation matrix :

$$\mathcal{U} = \begin{pmatrix} \mathrm{e}^{i\phi_R/2} \cos\left(\theta_R/2\right) & \mathrm{e}^{-i\phi_R/2} \sin\left(\theta_R/2\right) \\ -\mathrm{e}^{i\phi_R/2} \sin\left(\theta_R/2\right) & \mathrm{e}^{-i\phi_R/2} \cos\left(\theta_R/2\right) \end{pmatrix}.$$

In the local axes, the exchange-correlation potential $\mathbf{V}_{xc}(\vec{r}_R)$ can be diagonalized in spinor space :

$$\mathcal{U}^{\dagger}\, \mathbf{V}_{xc}(\vec{r}_R)\, \mathcal{U} = \begin{pmatrix} V_{xc}^{\uparrow}(\vec{r}_R) & 0 \\ 0 & V_{xc}^{\downarrow}(\vec{r}_R) \end{pmatrix}$$

$V_{\mathrm{xc}}^{\sigma}(\vec{r}_R) = \delta E_{\mathrm{xc}}/\delta \rho^{\sigma}(\vec{r}_R)$ is the exchange-correlation potential referred to local quantization axes referred to by $\sigma = \uparrow, \downarrow$ in the Wigner-Seitz cell labeled by R. Furthermore,

$$V_{xc}^{(1)}(\vec{r}_R) = \frac{1}{2}\left\{V_{xc}^{\uparrow}(\vec{r}_R) + V_{xc}^{\downarrow}(\vec{r}_R)\right\}$$
$$V_{xc}^{(2)}(\vec{r}_R) = \frac{1}{2}\left\{V_{xc}^{\uparrow}(\vec{r}_R) - V_{xc}^{\downarrow}(\vec{r}_R)\right\}. \tag{8.3}$$

The spin-orbit potential, suitably spheridized within a muffin-tin is related to the spheridized Kohn-Sham potential in the absence of relativistic corrections via :

$$v(r) = \frac{1}{r}\frac{dV_{KS}(r)}{dr}$$

The use of this potential in describing the spin-orbit part has been discussed by Koelling and Harmon. [Koelling and Harmon 1977] Stiles *et.al.* [Stiles *et.al.* 2001] have argued that a more systematic approach incorporates two-body terms of the type introduced by Breit [Breit 1929]. This approach introduces not only the standard term given by us, but also a spin-other-orbit interaction, off diagonal in real space. This we have neglected for the time being in this work.

8.2.2   The TB-LMTO Hamiltonian

The Kohn-Sham equation can be represented in different bases. We shall choose the TB-LMTO in the maximally screened (or β) representation. Our choice is guided by the fact that the TB-LMTO-β representation of the Hamiltonian is sparse. This will be essential both for modelling substitutional disordered alloys and for the recursion method (which we shall subsequently use) to be computationally tractable.

The TB-LMTO basis is now set up in the usual way [Anderson and Jepson 1984] and applied to the above Kohn-Sham equation. The secular equation then leads to the TB-LMTO Hamiltonian :

$$\mathbf{H} = H^{(0)}\tilde{\mathbf{I}} + \vec{B} \cdot \vec{\mathbf{S}} + \mathbf{H}_{\mathrm{SO}}$$

where the second order spin-independent Hamiltonian is given by,

$$H^{(0)} = E_\nu + h^\beta - h^\beta \, o^\beta \, h^\beta$$

with,

$$
\begin{aligned}
h^\beta_{RL,R'L'} &= \left\{ C^{(1)}_{RL} - E_{\nu\ell} \right\} \delta_{RR'}\delta_{LL'} + \Delta^{(1)1/2}_{RL} S_{RL,R'L'} \Delta^{(1)1/2}_{R'L'} \dots \\
&\quad + \Delta^{(2)1/2}_{RL} S_{RL,R'L'} \Delta^{(2)1/2}_{R'L'} \, (\vec{e}_R \cdot \vec{e}_{R'})
\end{aligned}
\tag{8.4}
$$

The potential parameters referred to the local quantization axes are : $\Pi_{RL} \equiv \{C^\uparrow_{RL}, C^\downarrow_{RL}, \Delta^{\uparrow 1/2}_{RL},$ $\Delta^{\downarrow 1/2}_{RL}$, $o^\uparrow_{RL}$ and $o^\downarrow_{RL}\}$. Referred to the global axes these parameters transform to $\Pi^{(1)}_{RL} = (\Pi^\uparrow_{RL} + \Pi^\downarrow_{RL})/2$ and $\Pi^{(2)}_{RL} = (\Pi^\uparrow_{RL} - \Pi^\downarrow_{RL})/2$. $S_{RL,R'L'}$ is the screened structure matrix, short ranged in $|R - R'|$. The vector $\vec{e}_R$ is a unit vector in the direction of the local moment in the atomic sphere labeled by R.

$$
\begin{aligned}
\vec{B}_{RL,R'L'} &= \left(C^{(2)}_{RL} + \Delta^{(2)1/2}_{RL} S_{RL,R'L'} \Delta^{(1)1/2}_{R'L'} \right) \vec{e}_R + \left(\Delta^{(1)1/2}_{RL} S_{RL,R'L'} \Delta^{(2)1/2}_{R'L'} \right) \vec{e}_{R'} \dots \\
&\quad + \left(\Delta^{(2)1/2}_{RL} S_{RL,R'L'} \Delta^{(2)1/2}_{R'L'} \right) (\vec{e}_R \times \vec{e}_{R'})
\end{aligned}
\tag{8.5}
$$

When all spins in every Wigner-Seitz cell are collinear, $\vec{e}_R = \hat{z}$ for all R, then the first two terms in the Hamiltonian expression reduces to the usual LSDA expression, diagonal in the spinor space $\mathcal{S}$. Otherwise, the Hamiltonian has off-diagonal elements in $\mathcal{S}$

$$\mathbf{H}_{\mathrm{SO}} = \Lambda^+ \mathbf{S}^- + \Lambda^- \mathbf{S}^+ + \Lambda^z \mathbf{S}_z$$

Further,

$$
\begin{aligned}
\Lambda^+_{LR,L'R'} &= v_{R,LL'} N^+_L \, \delta_{RR'} \, \delta_{\ell,\ell'} \, \delta_{m',m+1} \\
\Lambda^-_{LR,L'R'} &= v_{R,LL'} N^-_L \, \delta_{RR'} \, \delta_{\ell,\ell'} \, \delta_{m',m-1} \\
\Lambda^z_{LR,L'R'} &= v_{R,LL'} m \, \delta_{RR'} \, \delta_{\ell,\ell'} \, \delta_{m,m'},
\end{aligned}
$$

$$(8.6)$$

with

$$
\begin{aligned}
N^+_L &= \sqrt{(\ell - m)(\ell + m + 1)} \\
N^-_L &= \sqrt{(\ell + m)(\ell - m + 1)}.
\end{aligned}
$$

The representation of the Green function in spinor space is a two-by-two matrix : $G^{\alpha\alpha'}_{RL,R'L'}$

The magnetic density of states is given by :

$$\vec{m}_{RL}(E) = -\frac{1}{\pi} \Im m \, \mathrm{Tr}_\alpha \, \left\{ \vec{\mathbf{S}} \mathbf{G}_{RL,RL}(E + i0) \right\}. \qquad (8.7)$$

Within the rigid moment approximation, the magnetic moment in the Wigner-Seitz cell labeled by R is :

$$\vec{m}_R = \sum_L \int_{-\infty}^{E_F} dE \, \vec{m}_{RL}(E) \qquad (8.8)$$

The unit vectors defined earlier are $\vec{e}_R = \vec{m}_R/m_R$.

8.2.3 The augmented space formalism and the augmented space Hamiltonian

The augmented space formalism [Mookerjee 1973] has been discussed in details in Chapter 5 of the thesis. Here we shall only describe the functional steps necessary to implement the technique.

Suppose a representation of the Hamiltonian of the disordered binary alloy in a denumerable basis $\{|R\rangle\}$ involves random potential parameters Π_R. For a substitutional, binary random alloy, this can be written in terms of a random "occupation" variable n_R as :

$$\Pi_R = \Pi_A\ n_R + \Pi_B\ (1 - n_R) = \Pi_B + \Delta\Pi\ n_R$$

where
$$n_R = \begin{cases} 1 & \text{if } R \text{ is occupied by atom } A \\ 0 & \text{if } R \text{ is occupied by atom } B \end{cases}$$

and $\Delta\Pi = \Pi_B - \Pi_A$ and the probability density is $p(n_R) = x_A\delta(n_R - 1) + x_B\delta(n_R)$, where x_A and x_B are the concentrations of the A and B species respectively. In the augmented space formalism, we associate with the random variable n_R an operator M_R in its configuration space, such that the spectral density of M_R is the probability density of n_R. For a binary variable, the configuration space of n_R, Φ_R, is of rank 2 and is spanned by the configurations $\{|A_R\rangle, |B_R\rangle\}$. We change to a basis $|0_R\rangle = \sqrt{x_A}|A_R\rangle + \sqrt{x_B}|B_R\rangle$ and $|1_R\rangle = \sqrt{x_B}|A_R\rangle - \sqrt{x_A}|B_R\rangle$.

In this basis, the representation of M_R is :

$$M_R = x_A\ I + (x_B - x_A)\ P_R^{(1)} + \sqrt{x_A x_B}\ T_R^{(01)}$$

, with $P_R^{(1)} = |1_R\rangle\langle 1_R|$ and $T_R^{(01)} = |1_R\rangle\langle 0_R| + |0_R\rangle\langle 1_R|$.

Following the prescription given by the Augmented Space Formalism (Chapter 5; Section "The Augmented Space Theorem"), corresponding to the potential parameters Π_R we get an associated operator in configuration space :

$$\widetilde{\Pi}_R = \ll \Pi \gg \tilde{I} + \mathcal{B}(\Pi)\ \widetilde{P}_R^{(1)} + \mathcal{F}(\Pi)\ \widetilde{T}_R^{(01)} \tag{8.9}$$

where, $\mathcal{B}(\Pi) = (x_B - x_A)\,\Delta\Pi$ and $\mathcal{F}(\Pi) = \sqrt{x_B x_A}\,\Delta\Pi$, $\Delta\Pi = \Pi_B - \Pi_A$.

We can now start from Eqns.(8.4)-(8.5) and rewrite the Hamiltonian as an operator in the space spanned by the TB-LMTO basis $\{|R\rangle\}$. Each element is a $(\ell_{max}+1)^2$ matrix in L space. We now allow each potential parameter to be random. Referring to Eqn.(8.9) we can construct the augmented space Hamiltonian :

$$
\begin{aligned}
\underset{\approx}{\widetilde{h}}^{\beta} &= \sum_R \underset{\approx}{\widetilde{A}}_R \otimes P_R + \sum_{RR'}\left\{ \underset{\approx}{\widetilde{B}}^{(1)}_{RR'} \otimes T_{RR'} + \left(\underset{\approx}{\widetilde{B}}^{(2)}_{RR'} \otimes T_{RR'}\right)\sum_{\mu} e^{\mu}_R e^{\mu}_{R'} \right\} \\
\underset{\approx}{\widetilde{B}}^{\mu} &= \sum_R \left(\underset{\approx}{\widetilde{D}}_R \otimes P_R + \sum_{R'} \underset{\approx}{\widetilde{B}}^{(3)}_{RR'} \otimes T_{RR'} \right) e^{\mu}_R \\
&\quad + \sum_{RR'}\left\{ \left(\underset{\approx}{\widetilde{B}}^{(4)}_{RR'} \otimes T_{RR'}\right) e^{\mu}_{R'} + \left(\underset{\approx}{\widetilde{B}}^{(2)}_{RR'} \otimes T_{RR'}\right)\sum_{\nu\xi} \varepsilon^{\mu\nu\xi}\, e^{\nu}_R e^{\xi}_{R'} \right\}
\end{aligned}
$$

where,

$$
\begin{aligned}
\underset{\approx}{\widetilde{A}}_R &= \widetilde{C}^{(1)}_R - \widetilde{E}_{\nu} \;\; ; \;\; \widetilde{D}_R = \widetilde{C}^{(2)}_R \;\; ; \;\; \underset{\approx}{\widetilde{B}}^{(1)}_{RR'} = \underset{\approx}{\widetilde{\Delta}}^{(1)^{1/2}}_R \otimes \underline{S}_{RR'}\tilde{I} \otimes \underset{\approx}{\widetilde{\Delta}}^{(1)^{1/2}}_{R'} \;\; ; \\
\underset{\approx}{\widetilde{B}}^{(2)}_{RR'} &= \underset{\approx}{\widetilde{\Delta}}^{(2)^{1/2}}_R \otimes \underline{S}_{RR'}\tilde{I} \otimes \underset{\approx}{\widetilde{\Delta}}^{(2)^{1/2}}_{R'} \\
\underset{\approx}{\widetilde{B}}^{(3)}_{RR'} &= \underset{\approx}{\widetilde{\Delta}}^{(2)^{1/2}}_R \otimes \underline{S}_{RR'}\tilde{I} \otimes \underset{\approx}{\widetilde{\Delta}}^{(1)^{1/2}}_{R'} \;\; ; \;\; \underset{\approx}{\widetilde{B}}^{(4)}_{RR'} = \underset{\approx}{\widetilde{\Delta}}^{(1)^{1/2}}_R \otimes \underline{S}_{RR'}\tilde{I} \otimes \underset{\approx}{\widetilde{\Delta}}^{(2)^{1/2}}_{R'}.
\end{aligned}
$$

Thus,

$$
\underset{\approx}{\widetilde{H}}^{(0)} = \underset{\approx}{\widetilde{E}}_{\nu} + \underset{\approx}{\widetilde{h}}^{\beta} - \underset{\approx}{\widetilde{h}}^{\beta} \otimes \underset{\approx}{\widetilde{\varrho}}^{\beta} \otimes \underset{\approx}{\widetilde{h}}^{\beta}
$$

where,

$$
\underset{\approx}{\widetilde{E}}_{\nu} = \underset{\approx}{\widetilde{E}}_{\nu} \otimes I \qquad \underset{\approx}{\widetilde{\varrho}}^{\beta} = \sum_R \underset{\approx}{\widetilde{\varrho}}_R \otimes P_R.
$$

Similarly, for the spin-orbit part :

$$
\underset{\approx}{\widetilde{\Lambda}}^{+} = \sum_R \underset{\approx}{\widetilde{v}}^{+} \otimes P_R \qquad \underset{\approx}{\widetilde{\Lambda}}^{-} = \sum_R \underset{\approx}{\widetilde{v}}^{-} \otimes P_R
$$

$$
\underset{\approx}{\widetilde{\Lambda}}^{+} = \sum_R \underset{\approx}{\widetilde{v}}^{z} \otimes P_R.
$$

So that the full augmented space Hamiltonian becomes :

$$\widetilde{\mathbf{H}} = \widetilde{\underline{\underline{H}}}^{(0)}\mathbf{I} + \sum_{\mu} \widetilde{\underline{\underline{B}}}^{\mu}\,\mathbf{S}^{\mu} + \widetilde{\underline{\underline{\Lambda}}}^{+}\mathbf{S}^{-} + \widetilde{\underline{\underline{\Lambda}}}^{-}\,\mathbf{S}^{+} + \widetilde{\underline{\underline{\Lambda}}}^{z}\mathbf{S}^{z}$$

$$(8.10)$$

The augmented space theorem then gives the averaged Green function as :

$$\ll \mathbf{G}_{RL,R'L'}(E) \gg = \ \langle RL\{\emptyset\}|\ \widetilde{\mathbf{G}}(E)\ |R'L'\{\emptyset\}\rangle \tag{8.11}$$

where

$$\widetilde{\mathbf{G}}(E) = \left(E\widetilde{\mathbf{I}} - \widetilde{\mathbf{H}}\right)^{-1}$$

and the averaged projected and magnetic density of states are :

$$\begin{aligned}
\ll n_{RL}(E) \gg &= -\frac{1}{\pi}\Im m \mathrm{Tr}_{\mathcal{S}}\left\{\widetilde{\mathbf{G}}_{RL\{\emptyset\},RL\{\emptyset\}}(E+i0)\right\} \\
\ll \vec{m}_{RL}(E) \gg &= -\frac{1}{\pi}\Im m\ \mathrm{Tr}_{\mathcal{S}}\left\{\vec{\mathbf{S}}\ \widetilde{\mathbf{G}}_{RL\{\emptyset\},RL\{\emptyset\}}(E+i0)\right\}.
\end{aligned}$$

$$(8.12)$$

8.2.4   The Recursion Method in augmented space for non-collinear systems

One of the useful $O(N)$ methods for the calculation of the Green function in systems where lattice translation symmetry is broken is the recursion method proposed by Haydock *et.al.* [Haydock *et.al.* 1972]. The augmented space theorem tells us that the Green functions calculated with the full augmented space Hamiltonian (described above) and projected onto the configuration subspace spanned by $|\emptyset\rangle = \prod_{R}^{\otimes}|0_R>$ is the configuration averaged Green function. The result is exact, and therefore, if we obtain the averaged Green function by the recursion method, the only approximations will be those related to the *termination* of the continued fraction. Haydock and coworkers [Haydock 1980] and

Beer and Pettifor [Beer and Pettifor 1984] have described various analyticity preserving terminators. Unlike mean-field theories like the CPA and its cluster generalizations, these approximations are controlled and errors can also be easily estimated [Haydock 1980].

In order to calculate a generalized non-collinear magnetization density, we need also to calculate the non-diagonal elements of the Green function in spinor space [Bergman *et.al.* 2006]. At this point we may proceed in several different ways. Either we carry out three recursions with local quantization axis rotated in the x,y or z directions by SU(2) rotation matrices, or the non-diagonal elements of the Green function can be calculated either by performing several recursions with carefully chosen starting states [Frota-Pessoa 1992] or by performing vector recursion [Nex 1989, Saha and Mookerjee 2005]. Since more accurate terminators are available for scalar recursions, this will be our preferred technique. However, vector recursion is elegant and requires a single application for both the diagonal and off-diagonal Green function spinor matrix elements. We shall postpone application of vector recursion for a future project. For the sake of completeness, we shall briefly describe the scalar recursion technique in the full augmented space.

If we do a rigid moment approximation within an atomic sphere, then we can define a local spin-axis in which $\mathbf{S}_z$ is diagonal. We can apply unitary SU(2) rotation operators $\mathcal{U}_x$, $\mathcal{U}_y$ and $\mathcal{U}_z = I$ which diagonalize $\mathbf{S}_x$ and $\mathbf{S}_y$ and $\mathbf{S}_z$. Thus,

$$
\begin{aligned}
\ll m_{RL}^{\mu}(E) \gg &= -\frac{1}{\pi} \Im m \ \mathrm{Tr} \left\{ \mathbf{S}^{\mu} \ \mathcal{U}_{\mu}^{\dagger} \mathcal{U}_{\mu} \ \mathbf{G}_{RL\{\emptyset\},RL\{\emptyset\}}(E) \ \mathcal{U}_{\mu}^{\dagger} \mathcal{U}_{\mu} \right\} \\
&= -\frac{1}{\pi} \Im m \ \mathrm{Tr} \left\{ \left(\mathcal{U}_{\mu} \mathbf{S}^{\mu} \mathcal{U}_{\mu}^{\dagger} \right) \ \left(\mathcal{U}_{\mu} \mathbf{G}_{RL\{\emptyset\},RL\{\emptyset\}}(E) \mathcal{U}_{\mu}^{\dagger} \right) \right\} \\
&= -\frac{1}{\pi} \Im m \ \mathrm{Tr} \left\{ \mathbf{S}_{\mu}' \ \mathbf{G}_{RL\{\emptyset\},RL\{\emptyset\}}'(E) \right\}
\end{aligned}
\tag{8.13}
$$

and

$$
\ll m_R^{\mu} \gg = \sum_L \int_{-\infty}^{E_F} dE \ll m_{RL}^{\mu}(E) \gg
$$

.

Since $\mathbf{S}_{\mu}'$ are diagonal in spinor space we need to calculate only the diagonal elements of $\mathbf{G}_{RL\{\emptyset\},RL\{\emptyset\}}'$. This requires two recursions per direction, so six recursions in all. Moreover,

$$
\widetilde{\mathbf{G}}'(E) = \left(E\hat{\mathbf{I}} - \widetilde{\mathbf{H}}' \right)^{-1}
$$

where,

$$\widetilde{\mathbf{H}}' = \underline{\widetilde{\underline{H}}}^{(0)}\mathbf{I} + \sum_\mu \underline{\widetilde{\underline{B}}}^\mu \; \mathbf{S}'^\mu + \underline{\widetilde{\underline{\Lambda}}}^+ \mathbf{S}'^- + \underline{\widetilde{\underline{\Lambda}}}^- \mathbf{S}'^+ + \underline{\widetilde{\underline{\Lambda}}}^z \mathbf{S}'^z$$

.
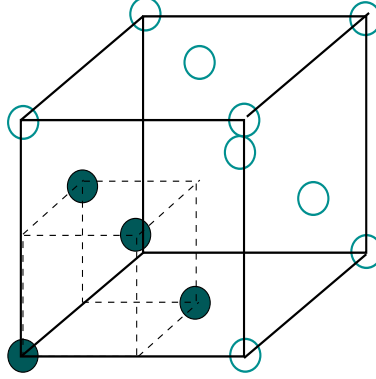
Figure 8.1: Choice of the magnetic primitive cell on a fcc lattice.

The recursion in full augmented space then follows : first, we have to have a representation of 'states' in augmented space. In the absence of disorder the representation is simple : a state is labeled by L and R. So we can represent this by a $(\ell_{max} + 1)^2 \times N$ matrix, where ℓ_{max} is the maximum angular momentum labels in the TB-LMTO minimal basis (usually 9 for s,p and d basis) and N is the maximum number of muffin-tins considered in the recursion procedure. For spin degrees of freedom each scalar in this $(\ell_{max}+1)^2 \times N$ matrix is replaced by a 1×2 spinor. So one such state may be represented by the symbol : $|\Phi^\alpha_{RL}\rangle$ with $R = 1, 2, \ldots N$, $L = 1, 2, \ldots (\ell_{max} + 1)^2$ and $\alpha = 1, 2$.

The states in configuration space can be uniquely labeled by the *cardinality sequence* : i.e. the sequence of sites $\{\mathcal{C}\}$ where we have a state $|1_R>$. For example, the configuration state

$$|0_{R_1}, \ldots 1_{R_k}, 0_{R_{k+1}} \ldots 1_{R_\ell} \ldots > \equiv |\{R_k, R_\ell, \ldots\} > .$$

A state in the full augmented space is given by $\Phi = |\Phi^\alpha_{RL} \otimes \{\mathcal{C}\}\rangle$. The inner product is defined by :

$$(\Psi \odot \Phi) = \sum_{RL\alpha} \Psi^\alpha_{RL} \Phi^\alpha_{RL} \; \delta(\mathcal{C}, \mathcal{C}'),$$
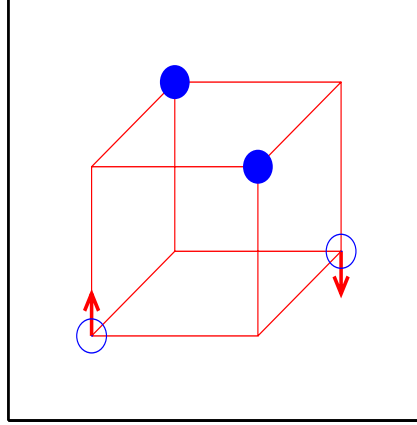
Figure 8.2: Collinear anti-ferromagnetism in ordered $L1_0$ MnPt. Mn atoms are shown as (blue) open circles while the Pt ions as (blue) closed circles.

The recursion begins with a state

$$|0\rangle = |\Phi_{RL}^\alpha \otimes \{\emptyset\}\rangle \tag{8.14}$$

The other states are generated from :

$$\beta_{n+1}|n+1\rangle = \widetilde{\mathbf{H}}|n\rangle - \alpha_n|n\rangle - \beta_n|n-1\rangle \tag{8.15}$$

Imposing orthogonality, one obtains

$$\alpha_n = \frac{\langle n|\widetilde{\mathbf{H}}|n\rangle}{\langle n|n\rangle} \quad \beta_n = \frac{\langle n-1|\widetilde{\mathbf{H}}|n\rangle}{\langle n-1|n-1\rangle} \tag{8.16}$$

This new basis tri-diagonalizes the Hamiltonian. It follows that,

$$G^{(N)}(E) = (E - \alpha_{N+1} - T(E))^{-1}$$
$$G^{(n)}(E) = (E - \alpha_{n+1} - \beta_{n+1}^2 G^{(n+1)}(E))^{-1}$$
$$\text{for} \quad n \leq N-1$$
$$G^{(0)}(E) = \ll G_{RL\alpha,RL\alpha}(E) \gg, \tag{8.17}$$
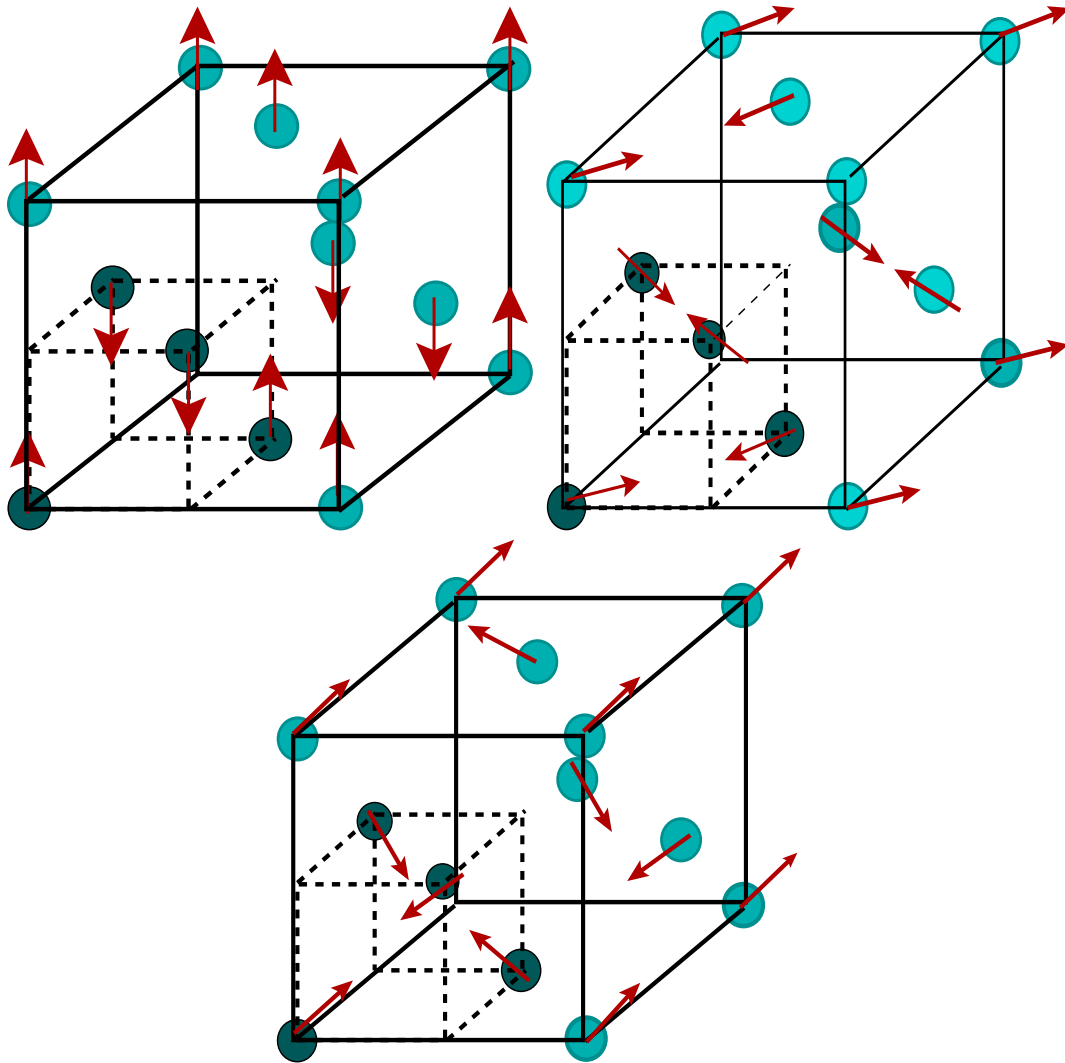
Figure 8.3: The 1Q, 2Q and 3Q magnetic structures on the magnetic primitive lattice in a fcc structure
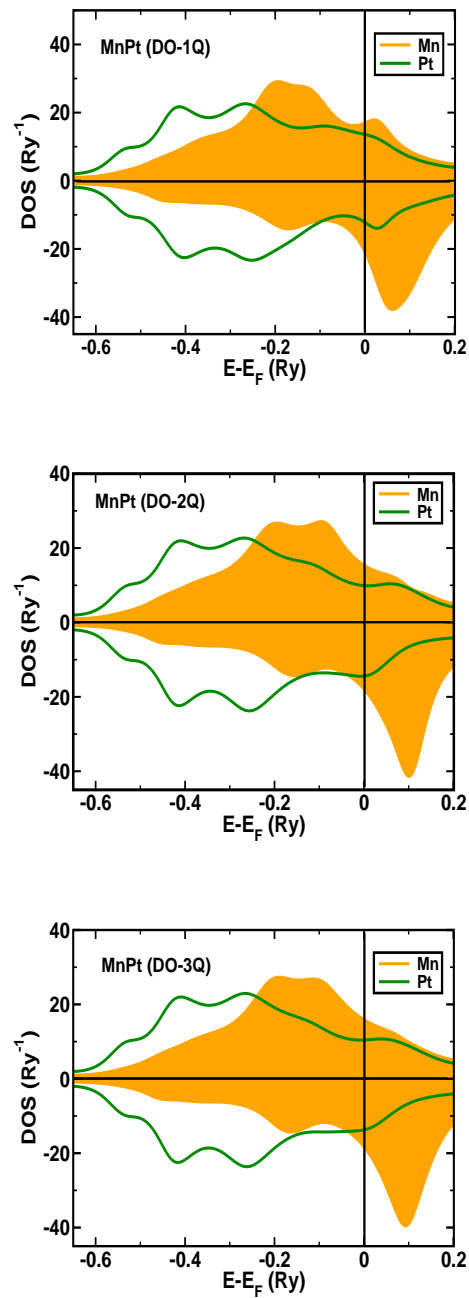
Figure 8.4: Partial density of states for Mn and Pt for the disordered (DO) 1Q, 2Q and 3Q spin arrangements in MnPt alloys
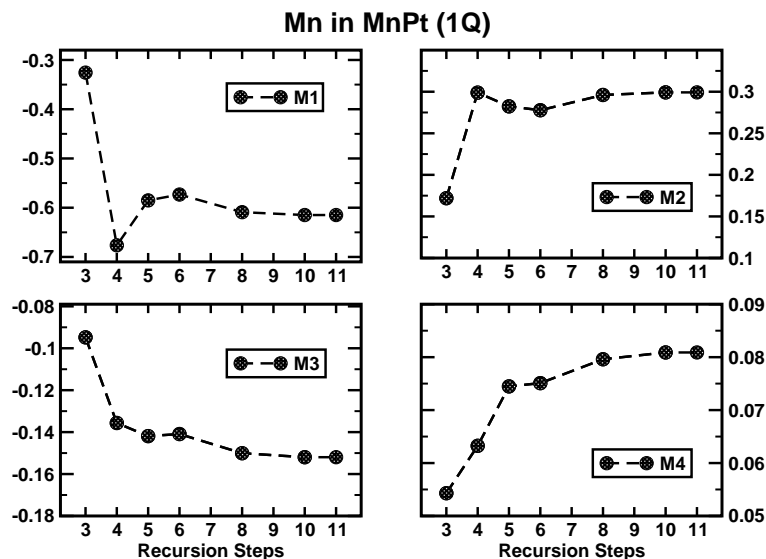
Figure 8.5: Variation of the first four moments of the partial DOS of Mn in MnPt in the 1Q magnetic structure. The variation is with the number of recursion steps after which the asymptotic part of the continued fraction expression for the Green function is replaced by a Beer-Pettifor Terminator. The units for the moments M_n are $(Ry)^n$.

where $T(E)$ is one of the terminators suggested by Haydock [Haydock 1980] or Beer and Pettifor [Beer and Pettifor 1984]. Two recursions with the two possible starting states in Eqn. (8.14) for the two values of α give the two diagonal matrix elements in spinor space.

The ordered inter-metallic compound 50-50 MnPt has a L1$_0$ structure. A small tetragonal distortion with $c/a \simeq 0.92$ lowers the total energy and stabilizes the compound. It exhibits collinear anti-ferromagnetism of the Mn atoms only. The Pt atoms carry negligible magnetic moment. The Néel temperature is rather high $\approx 1000K$ [Kren *et.al.* 1968]. Figure 8.1 shows choice of the magnetic primitive cell for the alloys. For ordered MnPt alloy in the L1$_0$ structure the Mn and Pt atoms sit in alternate layers. This is shown in Fig.8.2. It is experimentally known that the possible magnetic structure of Mn atoms is a AF-I type arrangement shown in Fig. 8.2.
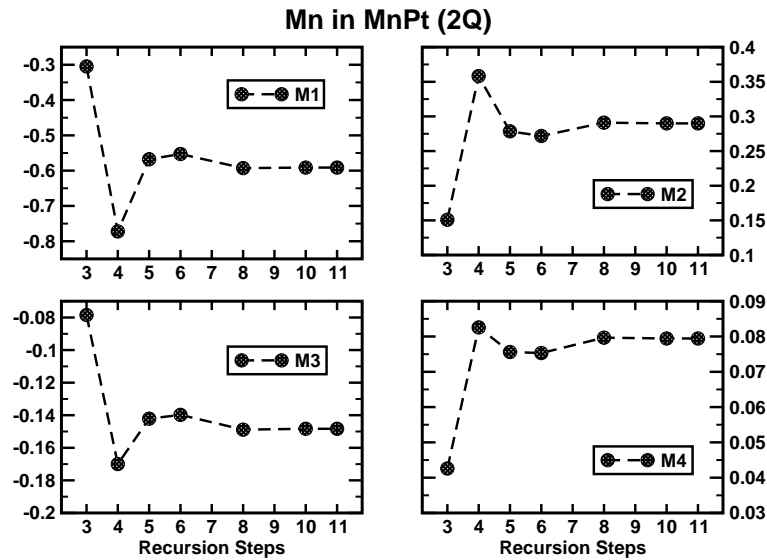
Figure 8.6: Same as above but for the 2Q magnetic structure.
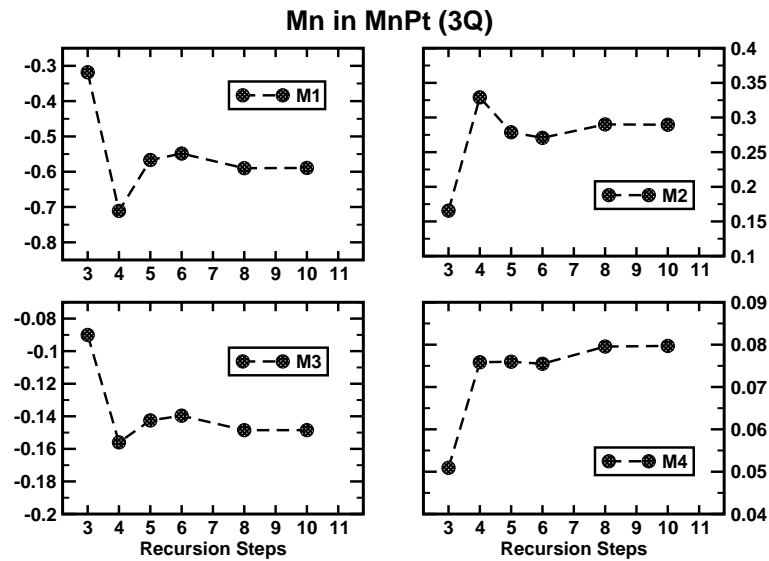
Figure 8.7: Same as above but for the 3Q magnetic structure.

Although ordered 50-50 MnPt has been studied earlier, not much work has been done on disordered 50-50 MnPt which has been prepared in thin film form. Interest in this alloy

waned, primarily because the exchange bias mechanism is absent in them and therefore probability of their potential use in GMR devices is doubtful. Nevertheless, presence of possible anti-ferromagnetic Mn in the alloy and Pt which provides spin-orbit coupling makes this alloy system a fertile ground for a search for non-collinear magnetic phases.

In the disordered alloy, in contrast with the $L1_0$ ordered arrangement, the Mn and Pt atoms do not sit in parallel planes. The lattice structure is strictly face-centered cubic with both the corner and face-centre positions being occupied randomly with either Mn or Pt atoms with equal probability.

The magnetic arrangements on this face-centered lattice are shown in Fig.8.3. The simplest is the 1Q arrangement where the intra-layer alignment is collinear ferromagnetic while the inter-layer alignment is anti-ferromagnetic. If we choose the positive c-axis as the global axis of quantization (z-axis) and represent the unit vector along the magnetic moment by $\vec{e}_R = (\theta_R, \phi_R)$, and if we label the position of the two sites on the bottom $x - y$ plane as R_1, R_2 and those on the top x-y plane as R_3, R_4, then,

$$\phi_{R_k} = 0^o, \text{ for } k = 1, 2 \ldots 4$$
$$\theta_{R_1} = \theta_{R_2} = 0^o \; ; \; \theta_{R_3} = \theta_{R_4} = 180^o$$

The next arrangement is the 2Q non-collinear anti-ferromagnetic structure shown in the middle panel of Fig. 8.3. Here,

$$\theta_{R_k} = 90^o, \text{ for } k = 1, 2 \ldots 4$$
$$\phi_{R_1} = 45^o \; , \; \phi_{R_2} = 225^o \; , \; \phi_{R_3} = 135^o \; , \; \phi_{R_4} = 315^o$$

The moments lie in planes in twos and point towards each other. Finally the last

Spin structure	M^a (μ_B)	M^p (μ_B)
1Q	2.75	2.08
2Q	2.76	2.19
3Q	2.76	2.16

Table 8.1: Magnetic moments obtained from TB-LMTO-CPA and TB-LMTO-ASR. [a] refers to the TB-LMTO-CPA work by Sakuma [Sakuma 2000], while [p] refers to our present work.

arrangement is the 3Q structure shown in the right-most panel of Fig.8.3. This structure is quite similar to the 2Q with the difference that spins are raised in the lower plane and dipped in the upper plane so that now they all point towards the cube centre.

$$\theta_{R_k} = 54.7^o, \text{ for } k = 1, 2 \ldots 4$$

$$\phi_{R_1} = 45^o \ , \ \ \phi_{R_2} = 225^o \ , \ \ \phi_{R_3} = 135^o \ , \ \ \phi_{R_4} = 315^o$$

We have carried out a fully self-consistent local density matrix functional approximation electronic structure and total energy calculation on all the three magnetic structures of the disordered MnPt alloy. We have chosen to carry out scalar recursions in the framework of the local quantization axes. We carried out 11 recursions steps on a augmented space cluster with seven nearest neighbour shells around a central site. The terminator chosen was that of Beer and Pettifor [Beer and Pettifor 1984]. The Madelung energy was estimated by the method of Ruban and Skriver [Ruban and Skriver 2003]. The lattice constants of the ordered and disordered phases do not vary much and our presented calculations were done with a = 3.77 A. In Fig 8.4 we present our partial (constituent projected) density of states (PDOS) results of our TB-LMTO-ASR calculations.

Before we discuss the disordered alloy, we remind the reader of the earlier work on the DOS of L1$_0$ AF-I MnPt [Sakuma 2000] and the related MnNi [Sakuma 1998] alloys. Both have a prominent pseudo-gap around the Fermi level. This as been assigned to the AF-I staggered field. This gap completely disappears in the ferromagnetic or paramagnetic arrangements. This pseudo-gap is absent in all the three disordered arrangements 1Q, 2Q and 3Q of MnPt. The random arrangement of Mn and Pt atoms, which have electronic structures very different from each other, means that the regular L1$_0$ arrangement in the ordered phase is strongly disrupted as Pt and Mn randomly replace each other. This disrupts the AF-I staggered field and prevents a pseudo-gap forming near the Fermi level.

We need to comment on the accuracy of our ASR calculations. In particular, the accuracy of the dominant terminator approximation of the ASR. As Haydock has argued [Haydock 1980] that the DOS itself is unstable under small perturbations and convergence criteria need to be based on the convergence of the energy moments of the DOS : $M_n = \int_{E_{min}}^{E_F} E^n \ n(E) \ dE$. Figure 8.5 shows the variation of the first four moments of the

Mn PDOS for the 1Q, 2Q and 3Q magnetic states in MnPt, with the number of exact recursion steps before the asymptotic part of the continued fraction expression for the Green function is replaced (terminated) by a Beer-Pettifor 'terminator'.We see that after 10-11 recursion steps the moments fluctuate by less than 5%. We have, therefore, terminated recursion after 11 steps with a sixth-nearest neighbour map in augmented space. Therefore, inaccuracy creeps up only in the 12th moment, as opposed the 8th moment in the CPA. The Beer-Pettifor terminator ensures that the asymptotic moments are also accurate.

Table 8.1 shows the magnetic moments from our results and compares them with the CPA results of Sakuma [Sakuma 2000]. The ASR agrees with the CPA that the 3Q arrangement has the lowest energy per atom. The CPA gave the 2Q arrangement to have almost the same energy as the 3Q arrangement and 1Q to be about 1.47 mRy/atom higher. The ASR on the other hand ordered the structures as 1Q, 1.41 mRy/atom higher and then 2Q at 1.68 mRy/atom higher still. These energy differences of a few mRy/atom are really at the very limit of error windows of either the CPA or the ASR. The error occurs in the TB-LMTO and then in the single-site CPA or the better ASR approximation. These errors are additive and it would be unwise to make definitive statements based on such small energy differences. The ASR estimates of the Mn moments are about 0.57-0.67 μ_B lower than the CPA.

8.3   Summary

In this chapter we have set up a computational framework for the study of non-collinear magnetic phases in disordered alloys based on the marriage of three distinct techniques : the TB-LMTO, the recursion method and the augmented space formalism. We have used our formalism to study disordered MnPt alloy. The very small energy differences between different non-collinear phases means that our error window should be very narrow. The augmented space formalism is formally exact, therefore the error arises in the recursion method and the TB-LMTO. Errors in the former are controlled and can be estimated. It is in the TB-LMTO that is the main source of error. A way out is either to replace TB-LMTO with the more accurate TB-KKR. This would lead to energy dependent potential

parameters and hence energy dependent recursion. This has been developed by us earlier [Ghosh *et.al.* 1999]. Alternatively we can use the full-potential LMTO. But in that case, the Hamiltonian is not sparse and we have to have a re-look at the errors in the recursion method. This work is now in progress.

It appears that no detailed experimental investigation into non-collinear magnetism in disordered MnPt alloy has been carried out to confirm our predictions. Until this is carried out, we have only the theoretical analyses at hand.

Chapter 9

Conclusion

In this concluding chapter we will discuss the developments made and objectives achieved in this thesis work and the scope for future developments that this work has opened up. This thesis attempts to understand the effect of confinement and disorder on binary systems.

1. In this direction the first set of studies that we made are on confined binary systems, namely on transition metal nano-alloy and nano-oxide clusters.

   We find that the first step to the study of electronic structure of clusters is the correct determination of ground state structure as magnetic and all other properties of clusters are strongly correlated with its exact geometric structure and arrangement of atoms. For the alloy clusters the search for the actual ground state geometry is guided by the geometries of the clusters of the constituent pure metals. But for such clusters the ground state search is non-trivial for in such clusters there exists "homotops",i.e., same geometric structure with different arrangement of atoms. For oxide cluster finding the actual ground state geometry itself has been a challenging task since all previous theoretical attempts were largely biased and few experiments on such oxide clusters exist in literature. Using a combination of first principle Born-Oppenheimer molecular dynamics simulation and then force optimization techniques we conducted an extensive and unbiased scan through the potential energy surface to reach the actual ground state structure.

   Both these systems show some properties much like bulk, others significantly different from bulk. In MnCo nanoalloy, as the environment is made more Mn-rich the

average moment of the Co atoms decreases like bulk. But unlike bulk the Co-rich alloy clusters are found to be ferromagnetic. The MnO clusters are antiferromagnetic much like bulk but they are found to have unusual two-dimensional structural growth upto clusters containing five MnO units. Infact, the larger sized clusters (containg 6-8 MnO units) are found to have these two-dimensional structures as their geometric units and not the bulk-like cuboidal structures as predicted by some studies.

Both these systems show great potential for industrial usage. Mn atoms being half-filled have a large number of unpaired electrons (5) and thus large atomic moment. But in bulk since pure Mn or even MnCo alloys are antiferromagnetic thus the total moment gets quenched. However in MnCo alloy clusters we see as long as the clusters are Co-rich they remain ferromagnetic and thus their net moments are much enhanced from the corresponding pure Co clusters. $(MnO)_x$ clusters for x=2 to 8 are antiferromagnetic like bulk. But Mn_x clusters are ferromagnetic for x < 5. Thus there is a transition of magnetic state of Mn_x clusters for x=2 to 4 from ferromagnetic to antiferromagnetic upon oxidation. This ability to chemically tune the magnetism in Mn clusters can be of great technological relevance. Infact a structural transition of Mn_x clusters also occur (from 3 dimensional to 2 dimensional) for x=4 and 5 upon oxidation. In future we intend to trace out the path of this magnetic and structural transition by studying off-stoichiometric manganese-oxide clusters.

For MnCo clusters we find it is necessary to carry out calculations for not only the ground states but also the low energy isomers for comparison of theoretical results with Stern-Gerlach (SG) experiments since in the SG beam the isomers are also present with a statistical weight. This is because the experiments are all carried out at very low but finite temperatures. Although for Manganese-Oxide clusters experimental reports are rare, still it is essential to investigate the isomers of such clusters to be prepared to correspond theoretical results with future experiments.

2. The next set of studies are on model and real substitutionally disordered binary alloys. The studies on model disordered binary alloys are in an attempt to under-

stand the effect of disorder on single and multiband superconductivity. Through these studies we have developed an efficient real-space based approach to study the effect of homogeneous as well as correlated disorder on single-band and multiband superconductivity. Our method can also deal with off-diagonal randomness that is present in alloys where there is local lattice distortion due to size mismatch of the constituents. Multiband superconductivity unlike single-band superconductivity opens up a paradigm beyond Anderson's theorem to understand the interplay of superconductivity with disorder. In future we intend to couple our technique with first-principles band structure calculation methodologies like the tight-binding linear muffin-tin orbital method to study the effect of disorder on superconductivity in real binary alloys.

3. Finally, we have also developed a formalism by combining the tight-binding linearized muffin-tin orbital method and the recursion methods with augmented space formalism (TB-LMTO-ASR) to study the effect of substitutional disorder on non-collinear magnetism in binary alloys. We have applied our methodology to MnPt alloy system in this thesis. However, at present we have kept our spin arrangements fixed at 1Q, 2Q and 3Q spin structures. In future we intend to relax the spin structure as well so that we are able to investigate the stability of some arbitrary spin arrangement for our system. Such spin relaxations has been done for ordered systems[Bergman *et.al.* 2006] and we intend to extend it for disordered alloys.

We also intend to extend our study of non-collinear magnetism for systems with partial disorder. Generally off-stoichiometric alloys exhibit partial disorder in the sense that only some of the sub-lattices of the stoichiometric ordered alloy becomes disordered. Binary alloys in stoichiometric composition generally exhibit ordered structures at low temperatures. As we depart from perfect stoichiometric compositions, it is not possible to populate the lattice in the given compositions so as to produce a perfectly ordered structure. For example, for a $B_{75}A_{25}$ binary alloy on a fcc lattice, one of the possible stable ordered phases is the L12 arrangement. In a cubic unit cell the corner is occupied by an A atom, while the three face centres are occupied by B atoms. Since there are N corners and 3N face centres (N being the total number of unit cells in the solid) and exactly as many A and B atoms,

at this composition the L12 ordered arrangement exactly populates all the lattice sites. But ordered arrangement becomes impossible for say $B_{70}A_{30}$. However, the following arrangement becomes possible: since there are now 1.2N A atoms, N of them occupy the N corners. The 3N face centres may be occupied randomly by the 2.8N B atoms and 0.2N remaining A atoms. The original A sublattice remains ordered, while the B sublattice becomes disordered. Since there are on the whole 3N face centres, the occupation probabilities of the A and B atoms in this sublattice are 0.93 and 0.06 respectively. This arrangement is quite different from that of the completely random alloy, where all sites are randomly occupied by either the A or B atoms with probabilities 0.3 and 0.7 respectively. It would be interesting to investigate the spin arrangements in systems with such partial disorder.

So, in future we intend to investigate these unexplored areas that this thesis work indicates to be physically intuitive and enriching.

Bibliography

Anderson P.W., J. Phys. Chem. Solids **11**, 26 (1959).

Andersen O.K. and Jepsen O. Phys. Rev. Lett **53** 2571 (1984).

Andrews M.P. and O'Brien S.C., J. Phys. Chem. **96**, 8233 (1992).

Annett J.F.,Litak G.,Györffy B.L., and Wysokinski K.I. Phys.Rev.B **66**, 134514 (2002)

Aryanpour K., Dagotto E.R., Mayr M., Paiva T., Pickett W.E.,and Scalettar R.T. Phys. Rev. B **73**, 104518 (2006).

Asano Y., Tanaka Y. and Kashiwaya S. Phys. Rev. Lett **96**, 097007 (2006).

Ashcroft N.W. and Mermin N.D. *Solid State Physics*, Harcourt College Publishers (1976).

Bader R. F. W. *Atoms in Molecules-A Quantum Theory* Oxford University Press (1990).

Bagwell P.F. Phys. Rev. B **49**, 6841 (1994).

Bansil A., *Electronic Band Structure and its Applications, Lecture Note Series*, (Springer-Verlag, Heidelberg) 283 (1987).

Becke A.D., *Phys. Rev. A* **38**, 3098 (1988).

Beer N. and Pettifor D. in *The Electronic Structure of Complex Systems* (Plenum Press, New York) (1984).

Bergman A., Nordström L., Klautau A.B., Frota-Pessoa S., and Eriksson O., Phys. Rev. B **73**, 174434 (2006).

Bertaut F.F. and Fruchart D., Int. J. Magn. **2** 259 (1972).

Blackman J.A., Esterling D.M. and Berk N.F., Phys. Rev. B **4**, 2412 (1971).

Blöchl P.E., Phys. Rev. B **50**, 17953 (1994).

Bose S.K., Kudronovský J., Jepsen O., and Andersen O.K., Phys. Rev. B **45**, 8272 (1992).

Boskovic C., Huffman J.C. and Christou G. Chem.Commun.2502 (2000).

Bullett D. *Solid State Physics* (Academic Press, New York)(1980) Vol.35.pp.129-215

Bouquet F., Fisher R.A., Phillips N.E., Hinks D.G., and Jorgensen J.D., Phys.Rev.Lett. **87**, 167003 (2001).

Breit G., *Phys. Rev.* **34** 553 (1929) ; **36** 383 (1930) ; **39** 616 (1936).

Brimblecombe Robin, Koo Annette, Dismukes G. Charles, Swiegers Gerhard F., Spiccia L. **132** 2892 (2010).

Cable J.W. Phys. Rev. B **25**, 4670 (1982).

Castro M., Jamorski C. and Salahub D.R., Chem. Phys. Lett. **271**, 133 (1997).

Ceperley D.M. and Alder B.J., Phys.Rev.Lett., **45** 566 (1980).

Chakrabarti A. and Mookerjee A., J.Phys. Condens Matter **13** 10149 (2001).

Chakrabarti A. and Mookerjee A. Euro. Phys. Journ. B **44**, 21 (2005).

Chen X.K., Konstantinovic M.J., Irwin J.C., Lawrie D.D., and Franck J.P., Phys.Rev.Lett. **87**, 157002 (2001).

Cheng Ming and Su W.P. Phys. Rev. B **72**, 094512 (2005).

Choi H.J., Roundy D., Sun H., Cohen M.L., and Louie S.G., Nature **418**, 758 (2002).

Christensen A., Stolze P., and Norskov J.K., J.Phys. Condens Matter **7**, 1047 (1995).

Covaci L. and Marsiglio F. Phys. Rev. B **73**, 014503 (2006)

Czajka K., Maska M.M, Mierzejewski M., and Sledz Z. Phys. Rev. B **72**, 035320 (2005).

Daghofer M., Moreo A., Riera J.A., Arrigoni E., Scalapino D.J., and Dagotto E., Phys.Rev.Lett. **101**, 237004 (2008).

Darby S., Mortimer-Jones T.V., Johnston R.L., and Roberts C., J. Chem. Phys. **116**, 1536 (2002).

Dasgupta I., Saha T., and Mookerjee A., Phys.Rev. **B51**, 3414 (1995).

Datta S., Kabir M., Ganguly S., Sanyal B., Saha-Dasgupta T. and Mookerjee A., Phys. Rev. B **76**, 014429 (2007).

Dean P., *Proc. Phys. Soc. (London)* **73**, 413 (1959).

Dean P., *Proc. Roy. Soc.* **A254**, 507 (1960).

Dean P., *Proc. Roy. Soc.* **A260**, 263 (1961).

Ehrenreich H. and Schwartz L., *Solid State Physics*, Seitz F. and Turnbull D., Ed.(Acedemic, New York) **31**, 149 (1976).

Faulkner J.S.,*Progress in Materials Science* **27**, 1 (1982).

Fermi E. Z.Phys. **48** 73 (1928); Thomas L.H.,Proc.Camb.Phil.Soc. **23** 542(1927)

Foo E-Ni, Amar H. and Ausloos M., Phys. Rev. B **4** 3350 (1971)

de Gennes P.G., *Superconductivity of Metals and Alloys* (W.A.Benjamin, New York, 1966) p.140

Ferreira Kristina N., Iverson Tina M., Maghlaoui Karim, Barber James and Iwata So Science **303** 1831 (2004).

Frota-Pessoa S., Phys. Rev. **B 46** 14570 (1992).

Ghosh S., Das N. and Mookerjee A., Int.J.Mod.Phys. B **13** 723 (1999).

Ghosal Amit, Randeria Mohit, and Trivedi Nandini Phys. Rev. Lett **81**, 3940 (1998) .

Ghoshal Amit, Randeria Mohit, and Trivedi Nandini, Phys. Rev. B **65**, 014501 (2001).

Ghoshal Amit and Kee Hae-YoungPhys. Rev. B **69**, 224513 (2004).

Giubileoo F., Roditchev D., Sacks W., Lamy R., Thanh D.X., Klein J., Miraglia S., Fruchart D., Marcus J., and Monod P., Phys.Rev.Lett.**87**, 177008(2001).

Godin T.J. and Haydock R., Phys. Rev. B 38, 5237 (1988).

Godin T.J. and Haydock R., Phys. Rev. B 46, 1528 (1992).

Goldman A.M. and Markovic N., Phys. Today **51** (11), 39 (1998).

Gonis A., Zhang X.G., Freeman A.J., Turchi P., Stocks G.M., and Nicholson D.M., Phys. Rev. B **36**, 4630 (1987).

Häkkinen Hannu, Moseler Michael and Landman Uzi Phys. Rev. Lett. **89** 033401 (2002).

Han M.J., Ozaki T. and Yu J. The Journ.of Chem.Phys. **123**, 034306 (2005).

Hansen P.L., Molenbroek A.M. and Ruban A.V., J. Phys. Chem. B **101**, 1861 (1997).

Hayashi M. and Ebisawa H. Phys. Rev. B **72**,24505 (2005).

Haydock R. in *Solid State Physics* **35** (Academic Press, New York) (1980).

Haydock R.,Heine V. and Kelly M.J.,J. Phys. C : Solid State Phys **5** 2845 (1972).

Heersche H.B., Groot de Z., Folk J.A., Zant H.S.J. van der, Romeike C., Wegewjs M.R., Zobbi L., Barreca D., Tondello E. and Corria A. PRL **96**, 206801 (2006).

Henkelman G., Arnaldsson A. and Jnsson H. Comp. Mater. Sci. **36** 354 (2006).

Hocking W. H., Merer A. J., Milton D. J., Jones W. E.and Krwashnamurty G. **58** 516 (1980).

Hohenberg P. and Kohn W., Phys. Rev. B **136**, 864 (1964).

Hyeon T., Chem. Commun. (Cambridge) 08 **2003**, p.927.

Jellinek J. and Krissinel E.B., Chem. Phys. Lett. **258**, 283 (1996).

Jellinek J. and Lopez M.J., J. Chem. Phys. **110**, 8899 (1999).

Jellinek J., and Krissinel E.B., in *Theory of Atomic and Molecular Clusters*, edited by J. Jellinek (Springer, Berlin, 1999), pp.277-308.

Jellinek J., Faraday Discussions **138**, 11 (2008).

Jiao Feng and Frei Heinz Chem. Commun. **46**, 2920 (2010).

Kabir M., Mookerjee A. and Kanhere D.G., Phys. Rev. B **73**, 224439 (2006).

Kabir M., Kanhere D.G. and Mookerjee A., Phys. Rev. B. **75**, 214433 (2007).

Kakehashi Y., Akbar S. and Kimura N., Phys. Rev. B **57**, 8354 (1998).

Kamper K.P., Schmitt W., Guntherodt G., Gambino R.J. and Ruf R. Phys. Rev. Lett **59**, 2788 (1987).

Keesee R.G., Chen B., Harms A.C., Castleman A.W., Jr. Int.J.Mass Spectrom.Ion Processes **123** 225 (1993).

Ketelle, B. H. Phys. Rev. **76** 1256 (1949).

Kino H.,Wagner L.K. and Mitas L. J. Comp. Theo. Nano. **6** 2583 (2009).

Kirilyuk A., Fielicke A., Demyk K., von Helden G., Meijer G., and Rasing Th. Phys. Rev. B **82** 020405 (2010).

Klabunde K.J., *Free Atoms, Clusters and Nanoscale Particles*, (Academic, New York, 1994); Klabunde K.J., *Nanoscale Materials in Chemistry* (Wiley, New York, 2001).

Knickelbein M.B., Phys. Rev. Lett. **86**, 5255 (2001).

Knickelbein M.B., Phys. Rev. B **70**, 14424 (2004).

Knickelbein M.B., J. Chem. Phys. **125**, 044308 (2006).

Knickelbein M.B., Phys. Rev. B **75**, 014401 (2007).

Koelling D.D. and Harmon B.N., J. Phys. C-Sol. St. Phys. **10**, 3107 (1977).

Kondow T. *Progress in Experimental and Theoretical Studies of Clusters*, edited by Kondow T. and Maufune F. (World Scientific, New York, 2003)

Korotin M.A., Anisimov V.I., Khomskii D.I. and Sawatzky G.A. Phys. Rev. Lett. **80**, 4305 (1998).

Kren E., Kadar G., Pal L., Solyom J., Szabo P. and Tarnoczi T., Phys. Rev. **171** 574 (1968).

Kresse G. and Joubert D., Phys. Rev. B **59**, 1758 (1999).

Krissinel E.B. and Jelllinek J., Chem. Phys. Lett. **272**, 301 (1997).

Krissinel E.B. and Jellinek J., Int. J. Quantum Chem. **62**, 185 (1997).

Kübler J., Höck K.H., Sticht J. and Williams A.R., *J. Phys. F : Metal Phys* **18** 469 (1988).

Kudronovský J. and Maśek M., Phys. Rev. B **31**, 6424 (1985).

Kudronovský J. and Drchal V., Phys. Rev. B. **41**, 7515 (1990).

Kumar V., Srivastava V.K. and Mookerjee A., J. Phys. C : Solid State Phys **15** 1939 (1982).

Lee Gang H., Huh Seung H., Jeong Jin W., Choi Byeong J., Kim Seung H. and Ri Hyeong-C. J. Am. Chem. Soc. **124** 12094 (2002).

Li J., Wang Y.J., Zou B.S., Wu X.C., Lin J.G., Guo L. and Li Q.S. Appl. Phys. Lett. **70** 3047 (1997).

Linder J. and Sudbo A. Phys. Rev. B **77**, 064507 (2008)

Litak G., Miller P., Györffy B.L. *Physica C : Superconductivity* **251**, 263 (1995).

Litak G. and Györffy B.L. Phys. Rev. B **62**, 6629 (2000).

Loo C., Lowery A., Halas N., West J., and Drezek R., Nano Lett. **5**, 709 (2005); Huang X.H., Jain P.K., El-Sayed I.H., and M. A. El-Sayed, Nanomedicine **2**, 681 (2007); Pankhurst Q.A., Connolly J., Jones S.K., and Dobson J., J. Phys. D: Appl. Phys. **36**, R167 (2003); C. C. Berry, and A. S. G. Curtis, J. Phys. D: Appl. Phys. **36**, R198 (2003).

Lopez M.J., Marcos P.A., and Alonso J.A., J. Chem. Phys. **104**, 1056 (1996).

Lorenz R. and Hafner J., *J. Magn. Magn. Matter.* **139** 139 (1995).

Machida K., Ichioka M., Takigawa M., and Nakai N. pp. 32-45, Springer-Verlag Berlin Heidelberg (2002).

Martin A.M. and Annett James F. Phys. Rev. B **57**, 8709 (1998).

Martin A.M., Litak G., Györffy B.L., Annett J.F. and Wysokiński K.I. Phys. Rev. B **60**, 7523 (1999)

Matsui M., Ido T., Sato K., and Adachi K., J. Phys. Soc. Jpn. **28**, 791 (1970).

McElroy K., Lee D.H., Hoffman J.E., Lang K.M., Hudson E.W., Eisaki H., Uchida S. and Davis J.C. Phys.Rev.Lett **94**, 197005 (2005).

Men'shikov A.Z., Takzei G.A., Dorofeev Y.A., Kazantsev V.A., Kostyshin A.K., and Sych I.I., Sov. Phys. JETP **62**, 734 (1985).

Merer A.J. Annu. Rev. Phys. Chem. **40** 407 (1989).

Michalik M. and Wysokiński K.I., Acta Phys. Polonica A **106**, 653 (2004)

Michalik M. and Wysokiński K.I., Acta Phys. Polonica A **109**,623 (2006)

Mizushima T., Machida K., and Ichioka M. Phys. Rev. Lett **95**, 117003 (2005)

Molenbroek A.M. and Norskov J.K., and Clausen B.S., J. Phys. Chem. B **105**, 5450 (2001).

Mookerjee Abhijit, *J.Phys. C : Solid State Phys.* **6**, 1340 (1973);**6**, L205 (1973)

Mookerjee A., in *Electronic structure of alloys, surfaces and clusters* ed. A. Mookerjee and D.D. Sarma (Taylor-Francis, UK) (2003).

Mookerjee A. and Bishop A.R., J. Phys. C : Solid State Phys **7** 2165 (1974).

Mookerjee Abhijit and Prasad Rajendra Phys. Rev. B **48**, 17724 (1993).

Moradian R., Annett J.F., Györffy B.L. and Litak G. Phys. Rev. B **63**, 024501 (2000)

Moreo A., Daghofer M., Riera J.A., and Dagotto E., Phys.Rev.B **79**, 134502 (2009);arXiv:0906.1747v1 [cond-mat.supr-con] 9 Jun 2009

Morr D.K. and Yoon J. Phys. Rev. B **73**, 224511 (2006).

Nagamatsu J., Nakagawa N., Muranaka T., Zenitani Y. and Akimitsu J., Nature **410**, 63 (2001).

Nayak S.K. and Jena P. Phys. Rev. Lett **81**, 2970 (1998)

Nayak S.K. and Jena P. Phys. Rev. B **121**, 644 (1999)

Nex C.M.M., *Comp. Phys. Commun.* **53** 141 (1989).

Nosé S. Mol.Phys **52**, 255 (1984).

Oguchi T., Ono I. and Ishikawa T., J. Phys. Soc. Japan **35** 1586 (1973).

Pederson M.R. and Khanna S.N. Phys. Rev. B (Rap. Commun) **59** R693 (1999)

Perdew J.P., Phys. Rev. B **34**, 7406 (1986).

Perdew J.P., Burke K. and Ernzerhof M., Phys. Rev. Lett. **77**, 3865 (1996).

Pettifor D., *Electronic Theory in Alloy Design* (The Institute of Materials, London) 81 (1992)

Prasad R., in *Methods of Electronic Structure Calculations*, Andersen O.K., Kumar V., and Mookerjee A., Eds (World-Scientific, Singapore) 211 (1995). .

Raghu S., Qi X.L., Liu C.X., Scalapino D.J., and Zhang S.C., Phys.Rev.B **77**, 220503 (2008).

Razee S.S. A., Mookerjee A. and Prasad R., *J. Phys. Condens Matter* **3** 3301 (1991).

Renner Ch., Revaz B., Genoud J.Y., Kadowaki K. and Fischer O., *Phys. Rev. Lett.* **80**, 149 (1998)

Rieck C.T., Scharnberg K. and Scheffler S. *Electron Correlation in New Materials and Nanosystems* (Springer Netherlands,2007)

Ruban A.V. and Skriver H.L., Phys. Rev. B **66** 024201 (2003).

Ruban A.V., Skriver H.L., and Norskov J.K., Phys. Rev. B **59**, 15990 (1999).

Ruettinger, W., Yagi M., Wolf K., Bernasek, S., and Dismukes, G. C. J. Am. Chem. Soc. **122** 10353 (2000).

Saha T., Dasgupta I. and Mookerjee A., Phys. Rev. B **50** 13267 (1994).

Saha T., Dasgupta I., and Mookerjee A., J.Phys.:Condens.matter **6**, L245 (1994).

Saha T. and Mookerjee A., J. Phys. Condens Matter **8** 2915 (1996).

Saha K.K. and Mookerjee A., *J. Phys. Condens Matter* **17** 287 (2005).

Sakuma A., *J.Magn. Magn. Mater.* **187** 105 (1998).

Sakuma A., *J. Phys. Soc. (Japan)* **69** 3072 (2000).

Satpathy L., Goss D. and Banerjee M.K. Phys. Rev. **183** 887 (1969).

Schröder D. and Schwarz H., Angew. Chem. Int. Ed. Engl. **34** 1973 (1995).

Schwarz K. Journ.Phys.F **16**, L211 (1986).

Sessoli, R., Gatteschi, D., Caneschi, A. and Novak, M. A. Nature **365** 141 (1993).

Shull C. G. and Smart J. Samuel Phys. Rev. **76** 1256 (1949).

Shulthess T.C., Butler W.H., Stocks G.M., Maat S. and Mankey G.J., *J. Appl. Phys.* **15** 4842 (1999).

Sinfelt J.H., *Bimetallic Catalysts. Discoveries, Concepts, and Applications*, (John Wiley & Sons: New York, 1983).

Soven P., Phys. Rev. B **2**, 4715 (1970).

Stamatatos Theocharis C., Pringouri Konstantina V., Abboud Khalil A. and Christou George Polyhedron **28** 1624 (2009).

Sticht J., Höck K.H. and Kübler J., J. Phys. Condens Matter **1** 8155 (1989).

Stiles M.D., Halilov S.V., Hyman R.A. and Zangwill A., Phys. Rev. **B 64** 104430 (2001).

Suhl H., Matthias B.T., and Walker L.R. Phys.Rev.Lett **3** (1959)

Sun S., Murray C.B., Weller D., Folks L., and Moser A., Science **287**, 1989 (2000).

Shibata T., Bunker B.A., Zhang Z., Meisel D., Vardeman II C.F., and Gezelter J.D., J. Am. Chem. Soc. **124**, 11989 (2002).

Szabo P., Samuely P., Kacmarcik J., Klein T., Marcus J., Fruchart D., Miraglia S., Marcenat C., and Jansen A.G.M., Phys.Rev.Lett.**87**, 137005 (2001)

Szotek Z., Gyorffy B.L., Andersen O.K., and Jepsen O., Phys. Rev. Lett **76**, 307 (1996).

Tasiopoulos A.J., Wernsdorfer W., Moulton B., Zaworotko M.J., and Christou G. JACS **125**, 15274 (2003)

Towler M. D., Allan N. L., Harrison N. M., Saunders V. R., Mackrodt W. C. and Aprà, E. Phys. Rev. B **50**, 5041 (1994).

Tsuda S., Yokoya T., Kiss T., Takano Y., Togano K., Kito H., Ihara H. and Shin S., *Phys. Rev. Lett.* **87**, 177006 (2001).

M. Uhl, L.M. Sandratskii and J. Kübler, *Phys. Rev.* **B 50** 291 (1994).

Wagner L. K. and Mithas L. J. Chem. Phys. **126** 034105 (2007).

Wales David J. and Doye Jonathan P.K. J. Phys. Chem. A **101** , 5111 (1997).

Wang Y., *Phys. Rev. B* **54**, 16533 (1996).

Wang Y., Plackowski T., and Junod A., Physica C **355**, 179 (2001).

Wang Y., Gong X. and Wang J. Phys.Chem.Chem.Phys. **12**, 2471 (2010).

Watanabe T., Sasame H., Okuyama H., Takase K. and Takano Y. Phys.Rev.B **80**, 100502(R) (2009).

Weightman P., Wright H., Waddington S.D., Marel D., Sawatzky G.A., Diakun G.P., and Norman D., Phys. Rev. B **36**, 1725 (1987).

Wernsdorfer Wolfgang., Aliaga-Alcalde Nuria, Hendrickson David N., and Christou George Nature (London) **416** 406 (2002)

Wysokinski K.I.,Litak G.,Annett J.F., and Györffy B.L. Phys.Stat.Sol. **244** (2007).

Xu S., Moritomo Y., Kato K., and Nakamura A., J.Phys.Soc.Jpn. **70**, 1889 (2001).

Xu X., Yin S., Moro R. and de Heer W.A., Phys. Rev. Lett. **95**, 237209 (2005).

Yang H.D., Lin J.Y., Li H.H., Hsu F.H., Liu C.J., Li S.C., Yu R.C., and Jin C.Q., Phys.Rev.Lett.**87**, 167003 (2001).

Yin S., Moro R., Xu X., de Heer W.A., Phys. Rev. Lett. **98**, 113401 (2007).

Zarur A.J. and Ying J.Y., Nature (London) **403**, 65 (2000).

Zhao Yan-Xia, Hu Xiao-Nan, Ma Jia-Bi, He Sheng-Gui and Ding Xun-Lei Phys.Chem.Chem.Phys. **13**, 1925 (2011).

Zhu J.X., Ahn K.H., Nussinov Z., Lookman T., Balatsky A.V., and Bishop A.R. Phys. Rev. Lett 57004 (2003).

Zouni A., Witt Horst-Tobias, Kern J., Fromme P., Krauss N., Saenger W. and Orth P. Nature (London) **409** 739 (2001).

Ziemann Paul J. and Castleman A.W., Jr. Phys. Rev. B **46**, 13480 (1992).